Heterojunction Abruptness in GaAs/AlGaAs Superlattices Grown in an Atmospheric Pressure Inverted-Vertical MOCVD Reactor

Karen Oatis
BSEE, Oregon State University, Corvallis, Oregon, 1988
MSEE, Oregon State University, Corvallis, Oregon, 1991

A dissertation submitted to the faculty of the
Oregon Graduate Institute of Science & Technology
in partial fulfillment of the
requirements for the degree
Doctor of Philosophy
in Electrical Engineering

July 1995

The dissertation "Heterojunction Abruptness in GaAs/AlGaAs Superlattices Grown in an Atmospheric Pressure Inverted-Vertical MOCVD Reactor" by Karen Oatis has been examined and approved by the following Examination Committee.

James D. Parsons, Dissertation Advisor
Associate Professor

Rajendra Solanki
Associate Professor

Reinhart Engelmann
Professor

James T. Stanley
Assistant Professor
Materials Science and Engineering

To Keenan Oatis

Acknowledgements

I would like to thank my dissertation advisor, James D. Parsons, for advice and instruction in the art of crystal growth by MOCVD. I am grateful to the members of the thesis committee, Drs. Rajendra Solanki, Reinhart Engelmann, and James T. Stanley, for reviewing this dissertation and offering helpful suggestions. In particular, I thank Raj Solanki for extensive advice and consultation and for unlimited access to the x-ray diffraction system. He contributed significantly to the completion of this project.

I have been supported throughout my graduate work by a fellowship from AT&T Bell Laboratories. This fellowship provided me not only with generous financial support but also with invaluable human resources. I thank Equilla Wynn and Selwyn Joseph, fellowship program administrators, for their help; Roosevelt People and Sharon Sputz for allowing me to use their photoluminescence system; Henryk Temkin, Mort Panish, and Cammy Abernathy for my introduction to crystal growth; and W. Dexter Johnston for his unfailing support and encouragement, without which I would not have persisted.

I also want to thank many friends who offered needed help and support, among others: Jin Wu, Ajay Chaddha, SukRyong Hahn, Jeanne Selvy, Linda McCormick, and Mary Jensen. Each one helped make it possible.

Finally, I especially want to thank my son, Keenan Oatis, for his years of patience, tolerance, and doing the laundry.

Table of Contents

Page

List of Tables

List of Figures

List of Symbols

a_o	Lattice constant of substrate.
a_r	Relaxed (or actual) lattice constant of epilayer.
$a_\perp$	Lattice constant of epilayer perpendicular to plane of growth.
$a_{//}$	Lattice constant of epilayer parallel to plane of growth.
$[Al_o]$	Steady-state aluminum flow rate for superlattice growth.
C_A	Constant relating Al flow rate to AlAs growth rate.
C_G	Constant relating Ga flow rate to GaAs growth rate.
d	Thickness of layer or separation of diffracting layers (defined in context).
D	Thickness of 20-period superlattice stack.
E_a	Activation energy.
E_C	Conduction band energy relative to valence band maximum of GaAs.
E_g	Energy gap; also referred to as bandgap.
E_{PL}	Photoluminescence transition energy.
E_V	Valence band energy relative to valence band maximum of GaAs.
E_1	First quantized energy level in a quantum well.
E_{1C}	First quantized energy level in a conduction band well.
E_{1V}	First quantized energy level in a valence band well.
E_Γ	Directo energy gap.
E_X	Indirect energy gap.
$f_{1,2}$	Atomic scattering factor.
F	Structure factor for a given reflection.
$[Ga_o]$	Steady-state gallium flow rate for superlattice growth.

h	Planck's constant, $6.626 \times 10^{-34} \mathrm{J} \cdot \mathrm{s}$.
L_W	Effective width of a quantum well.
$m_W^{e,\,hh}$	Effective mass of electrons (e) and heavy holes (hh) in a quantum well.
$m_B^{e,\,hh}$	Effective mass of electrons (e) and heavy holes (hh) in a barrier layer.
m_o	Electron rest mass, $9.100 \times 10^{-31} \mathrm{kg}$.
p	Superlattice period as measured by double crystal rocking curves.
p_o	Superlattice period as designed.
Q[ ]	Flow rate of compound in the argument.
R	Gas constant, 0.08206 L atm K^{-1} mol^{-1}.
R_g	Growth rate.
$R_{r,nr}$	Radiative (r) and non-radiative (nr) recombintation rates of carriers.
t	Thickness of an arbitrary epitaxial layer.
t_b	Thickness of a superlattice barrier layer.
t_f	Fall time of a concentration pulse at the growing surface.
t_g	Growth interval in seconds.
t_r	Rise time of a concentration pulse at the growing surface.
t_w	Thickness of a superlattice well layer.
T	Temperature or specified point in time (defined in context).
T_g	Temperature of substrate during crystal growth.
$V_{B1,2}$	Barrier heights in asymmetrical square wells.
$V_{c,v}$	Barrier height in conduction and valence band wells, respectively.
$W_{1,2}$	Angle of incidence or diffraction in asymmetric reflections.
x	Mole fraction of aluminum in $Al_xGa_{1-x}As$.
$\bar{x}$	Average aluminum mole fraction in superlattice stack.

α	Substrate misorientation angle with respect to <001> direction.
$(\Delta a/a_o)_r$	Relaxed lattice mismatch between substrate and epilayer.
$\Delta a_\perp/a_o$	Relative perpendicular lattice mismatch between substrate and epilayer; also referred to as perpendicular strain.
$\Delta a_{//}/a_o$	Relative parallel lattice mismatch between substrate and epilayer; also referred to as parallel or in-plane strain.
$\Delta d/d$	Relative spacing difference of diffracting planes in substrate and epilayer
ΔE_C	Conduction band offset between GaAs and AlGaAs.
ΔE_V	Valence band offset between GaAs and AlGaAs.
Δp	Difference between period as measured and period as designed.
Δt	Growth interval of superlattice barriers and wells when $\Delta t_b=\Delta t_w$.
$\Delta t_{b.w}$	Growth intervals of superlattice barriers and wells.
Δt_I	Interval of the growth interrupt between superlattice barriers and wells.
$\Delta W_{1,2}$	Diffraction angle separation of substrate and epilayer in asymmetrical reflections.
$\Delta\nu$	Difference between Poisson's ratio for GaAs and Poisson's ratio for AlAs.
$\Delta\phi$	Difference between tilt of diffracting epilayer plane and tilt of diffracting substrate plane with respect to sample surface.
$\Delta\theta$	Difference in Bragg angle of substrate and epilayer.
$\Delta\omega_{PF}$	Angular separation between Pendllösung fringes.
$\Delta\omega_{SL}$	Angular separation between superlattice satellite peaks.
η_q	Radiative efficiency.
λ	X-ray wavelength.
λ_{PL}	Wavelength of photoluminescence transition.
μ_o	Reduced exciton mass.
ν	Poisson's ratio of components of elasticity tensor.

ϕ	Tilt of diffracting plane with respect to sample surface.
Ψ	Azimuthal orientation of substrate with respect to major and minor flats.
τ_A	Time constant characterizing the switching transient of DMAlH.
τ_G	Time constant characterizing the switching transient of TMGa.
θ	Arbitrary angle of x-ray incidence.
θ_B	Angle of x-ray incidence at which the Bragg condition is satisfied.
θ_i	Angle of x-ray incidence.
θ_d	Angle of x-ray diffraction.

List of Acronyms

ALE	Atomic Layer Epitaxy
AP	Atmospheric Pressure
BE	Bound Exciton
CW	Continuous Wave
DCRC	Double Crystal Rocking Curve
DI	De-Ionized
DMAlH	Di-Methyl Aluminum Hydride
FME	Flow-rate Modulation Epitaxy
FWHM	Full Width Half Maximum
GI	Growth Interruption
HEMT	High Electron Mobility Transistor
III-V	Three-Five Compounds
IV	Inverted Vertical
LN_2	Liquid Nitrogen
LP	Low Pressurer
LPE	Liquid Phase Epitaxy
MBE	Molecular Beam Epitaxy
MEE	Migration Enhanced Epitaxy
MFC	Mass Flow Controller
MOCVD	Metal Organic Chamical Vapor Deposition
MOMBE	Metal-Organic Molecular Beam Epitaxy
PBN	Pyrolytic Boron Nitride
PID	Proportional-Integral-Derivative
PIN	P-Type, Intrinsic, N-Type

PF	Pendellösung Fringes
PL	Photoluminescence
QW	Quantum Well
RF	Radio Frequency
RHEED	Reflection High Energy Electron Diffraction
SCCM	Standard Cubic Centimeters per Minute
SL	Superlattice
SLPM	Standard Liters Per Minute
TCE	Tri-Chloro-Ethane
TEGa	Tri-Ethyl Gallium
TMAl	Tri-Methyl Aluminum
TMGa	Tri-Methyl Gallium
UHV	Ultra-High Vacuum
VLSI	Very Large Scale Integration
V/III	Ratio of Group V to Group III Reactants
2D	Two Dimensional

ABSTRACT

Heterojunction Abruptness in GaAs/AlGaAs Superlattices Grown in an Atmospheric Pressure Inverted-Vertical MOCVD Reactor

Karen Oatis
Supervising Professor: James D. Parsons

A metal-organic chemical vapor deposition (MOCVD) system with an inverted-vertical reactor was built with a fast-switch manifold to minimize pressure variation during switching. Pressure variation is one of the causes of switching transients in the concentration of reactants in the manifold; these transients result in non-abrupt heterojunctions. The purpose of this work was to characterize the manifold and evaluate its effectiveness in controlling pressure variations, and thus the concentration gradient of source materials in the manifold.

The MOCVD growth process, using reactant sources trimethyl gallium (TMG), dimethyl aluminum hydride (DMAH), and arsine (AsH_3), was optimized for the growth of gallium arsenide (GaAs), aluminum arsenide (AlAs), and aluminum gallium arsenide ($Al_xGa_{1-x}As$). Multiple thin layers (superlattices) of dimensions comparable to those of the transient-induced interfacial layers were grown to characterize the manifold switching transient. Optimum superlattice parameters subject to growth and characterization system constraints were determined. Superlattices were grown on 2 inch Sumitomo semi-insulsating GaAs substrates. The structures had a nominal period of 350Å, consisting of 125Å of GaAs and 225Å of $Al_{0.8}Ga_{0.2}As$.

Double crystal rocking curve (DCRC) measurements of three crystal reflections were taken on each specimen. Substrate miscut and superlattice uniformity were determined from (004) plane reflections. Four (115) reflections were measured for each specimen to determine the misorientation of the epitaxial layers with respect to the substrate. The (002) reflections were used to evaluate the periodicity of the superlattice structure itself and to characterize the interfacial layers.

Using DCRC results, a model of the switching transient in the manifold was constructed; bandedge versus thickness and photoluminence (PL) transition energies were predicted from the model. Photoluminescence measurements were performed on the superlattice specimens and on quantum well stacks grown with various growth interruption intervals. The PL results were compared to the model derived from DCRC data and an optimum interval was suggested for the growth interruption required to form abrupt heterojunctions in this system.

Chapter 1

Introduction

1.1 Desirability of Thin Layers with Abrupt Interfaces

It is well known that the quality of the interfaces has a significant impact on the performance of devices based on very thin semiconductor heterostructures, such as quantum wells (QWs) and superlattices (SLs). The unique properties of these devices are a result of the quantum-mechanical interaction between carriers (electrons, holes, and excitons) and heterointerfaces. These properties can be exploited in devices characterized by quasi two-dimensional (2D) transport, such as high electron mobility transistors (HEMTs) and QW lasers, and in tunneling devices based on superlattice structures [1]. The correlation of microscopic interfacial quality with electrical and optical properties indicates that atomic scale morphology is a determining factor in charge carrier mobility parallel to the interface, that the concentration of interface traps determines radiative efficiency [2], and that the compositional abruptness of the heterojunction affects both radiative efficiency and emission wavelength [3].

The evaluation and improvement of heterointerface quality are therefore of considerable practical interest. A detailed knowledge of the nature of the interface is required to successfully adjust crystal growth and processing parameters so that device performance is optimized. The quality of heterojunctions is determined by the compositional abruptness of the junction, the atomic-scale roughness at the chemical interface, and the trap concentration at the interface. In addition, devices designed to use quantum confinement effects must have thickness uniformity of layers on the order of nanometers across relatively large areas of substrate. Layer thickness can be determined from double crystal x-ray diffraction (DCRC) measurements [4], and qualitative information on compositional abruptness can also be obtained from this technique [5]. Atomic-scale roughness and interfacial trap concentration can be inferred from the linewidth and line shape of the low temperature photoluminescence (PL) spectrum [6]. If accurate models of growth system behavior can be developed from the materials characterization data, appropriate process control adjustments can be made in a systematic way.

1.2 The GaAs/Al$_x$Ga$_{1-x}$As Material System

The III-V semiconductors GaAs and AlAs comprise an attractive material system for devices which require heteroepitaxial thin films of good crystal quality. Heteroepitaxy of these binary materials and their alloy, Al$_x$Ga$_{1-x}$As, is simplified by a lattice mismatch of only 1600ppm (±1%) between the binary compounds [7]. This small lattice mismatch reduces the effects of in-plane strain, which limits the thickness of epitaxial layers that can be grown coherently in materials systems with a larger mismatch [8].

Transition energies in a symmetric square QW are determined by well width, potential step height, and the effective masses of carriers in the well and barrier layers. Transition energies in GaAs QWs confined by AlAs or Al$_x$Ga$_{1-x}$As barriers are therefore a function of the potential step between the conduction (or valence) band in the well and the conduction (or valence) band in the barriers. The maximum conduction band potential step in this system is approximately 0.35eV, a value calculated using E_g(GaAs)=1.51eV at 300K [9], E_g(AlAs)=2.37eV at 300K [9], and the conduction band offset between GaAs and AlAs as presented by Kroemer [10].

The bandgap difference for $Al_xGa_{1-x}As$ follows Vegard's Law; hence both the potential step and the effective mass of the carriers in the barriers can be adjusted by changing the aluminum mole fraction in the barrier. The transition energies achievable by adjusting both barrier composition and well width are in the range 1.4 to 2.1 eV [11].

In addition to the relative simplicity of epitaxy in the GaAs/AlAs system and the desirable optical characteristics obtainable through bandgap engineering, the electronic properties of GaAs/AlGaAs heterostructures are also advantageous. The Hall mobility for electrons in bulk GaAs is on the order of $10^5 cm^2/Vs$ at 40K [9], while in HEMT structures where the electrons are confined by the band discontinuity, quasi-2D electron mobilities as high as $10^7 cm^2/Vs$ have been measured at ~1K [12]. These characteristics make this a technologically important material system.

1.3 Purpose and Methodology of this Investigation

The purpose of this work was to characterize the atmospheric pressure inverted-vertical MOCVD reactor and its fast-switch manifold in terms of layer thickness uniformity, heterojunction abruptness, heterojunction roughness, and interfacial trap concentration. The results were then used to determine optimum growth parameters and conditions for heterojunction growth in this system and to evaluate the feasibility of using this system for production of HEMTs and QW laser devices. The major steps involved in this work were:

1. Optimization of the growth of bulk GaAs, AlAs, and $Al_xGa_{1-x}As$ using Nomarski microscope examination and DCRC measurements;
2. Determination of appropriate superlattice parameters subject to MOCVD system constraints;

3. Growth of superlattices and quantum wells at optimized conditions with various growth interruption intervals;
4. Evaluation of substrate quality, epitaxial layer quality, and superlattice characteristics using DCRC measurements;
5. Construction of a model to describe concentration of reactants versus time in the reactor manifold;
6. Prediction of bandgap and PL transition energies from the model;
7. Determination of optical characteristics using PL measurements and comparison of these results with the model predictions; and
8. Proposal of optimum conditions for the growth of abrupt heterojunctions in this system.

1.4 Dissertation Overview

This thesis is divided into seven chapters including this introduction. Chapter 2 contains a review of epitaxial systems and describes the atmospheric pressure inverted-vertical MOCVD reactor used in this work. Chapter 3 details the growth parameters and conditions for bulk material, superlattices, and quantum wells grown for this investigation. In Chapter 4 there is a brief review of the double crystal rocking curve (DCRC) measurement technique, a discussion of the application of that technique to the current structures, and the presentation of DCRC data. Chapter 5 describes the construction of models for concentration versus time and bandgap versus thickness derived from the DCRC data. In Chapter 6 the photoluminescence data are presented and compared to the predictions of the model. Chapter 7 consists of conclusions about the performance of the fast-switch manifold and suggestions for improving interface abruptness through adjustment of growth parameters.

Chapter 2

Epitaxial Systems

Epitaxy describes a technique for the growth of thin layers of single crystal materials with a lattice structure identical to that of the crystalline substrate on which the growth occurs. The growing layer maintains the crystal structure and orientation of the substrate. The source materials for crystal growth can be present in either vapor or liquid phase. An advantage of epitaxial growth of semiconductors is that pure material can be grown at temperatures well below the melting point of the semiconductor. Another important advantage is that a crystal of one semiconductor material can be grown on the surface of a different semiconductor crystal [13].

The crystal quality of the epitaxial layer is determined by the degree to which the grown layer has the identical lattice constant as the substrate in the plane of growth. In homoepitaxial growth (the growth of crystalline layers on a substrate of the same material) the lattice constant of the epitaxial layer is by definition identical to that of the substrate. A heteroepitaxial process is defined as the growth of a crystalline material on a substrate of a different material [14].

In ideal heteroepitaxy the lattice constant of the grown layer parallel to the interface is identical with that of the substrate; this is the condition of perfectly coherent epitaxy. In this condition there is distortion, and therefore strain, in the epilayer perpendicular to the interface. In the GaAs/$Al_xGa_{1-x}As$ system the misfit between the lattice constant of the GaAs substrate and that of the epitaxial layer over the entire range of aluminum mole fraction is so small that thick epitaxial layers can be grown coherently; the layers are considered to be fully strained [15]. However, for highly mismatched materials the strain required to accommodate the layer to the substrate is reduced by the formation of misfit and threading dislocations when the epilayers are thicker than the pseudomorphic limit [16]. Recent work has indicated that $Al_xGa_{1-x}As$ may also form a semi-coherent interface with the substrate and that the layer undergoes some dislocation to accommodate the strain [17].

To achieve high quality epitaxy of crystalline material, the growth must be essentially two dimensional; that is, it must proceed one atomic layer at a time without the formation of three dimensional clumps or islands. This requires stringent control of reactant delivery and growth rate for coherent heteroepitaxy. In addition, useful growth processes must also be able to change material composition within Ångstroms to produce low-dimension devices, grow layers of high purity, and perform these tasks economically and reproducibly [18]. Several epitaxial techniques have been developed for the growth of semiconductor materials. The techniques applicable to the $GaAs/Al_xGa_{1-x}As$ system are liquid phase epitaxy (LPE), molecular beam epitaxy (MBE), metal-organic chemical vapor deposition (MOCVD) at both low pressure (LP) and atmospheric pressure (AP), and modulated beam flow epitaxy.

2.1 Liquid Phase Epitaxy

Liquid phase epitaxy was an important technique in the early research on III-V semiconductors. The apparatus is simple and material of high purity can be grown [18]. High purity source materials appropriate for the LPE process are available and there is also an inherent purification process occurring during the liquid to solid phase transition. This is essential for the growth of Al-containing materials, as Al is highly reactive and forms stable Al_2O_3. In LPE the Al_2O_3 is segregated on the surface of the melt, thus preventing oxygen incorporation in the epitaxial layer. Despite its simplicity and the high purity of the resulting material, LPE has limited flexibility. Growth of multilayer structures with abrupt interfaces is difficult and the thickness uniformity of layers is usually poor. Yield is therefore low and the process is extremely difficult to scale to the larger sizes required for production.

2.2 Molecular Beam Epitaxy

In the early 1970s the development of molecular beam epitaxy led to the growth of semiconductor materials with atomic layer control [19]. This made it possible to produce devices based on theoretically predicted behavior of low-dimensionality structures, including the Bloch oscillator, double heterojunction semiconductor lasers, and devices based on quantum confinement of carriers [1]. For some years MBE was the only technique capable of producing abrupt interfaces with no graded transition region between materials.

In MBE elemental sources are evaporated at a controlled rate onto a heated substrate under ultra-high-vacuum (UHV) conditions. When the growth rate is low enough to maintain two-dimensional growth, the resultant layer is epitaxial and the crystal is built up one layer at a time [20]. Recent developments include the use of metalorganic sources for both the group III and group V reactants in metalorganic molecular beam epitaxy, or MOMBE [21]. All MBE techniques are performed at pressures low enough (10^{-6} to 10^{-5} Torr) that the transport of atoms and molecules is by molecular flow and the mean free path of the reactant species is greater than the source-to-substrate distance [22]. Because of the high vacuum environment, *in situ* techniques to monitor and control atomic layer deposition are available, including reflection high energy electron diffraction (RHEED) and Auger spectroscopy. The limitations of MBE as a production process are low throughput, high capital outlay, and the maintenance of the high vacuum system.

2.3 Conventional Metal-Organic Chemical Vapor Deposition

MOCVD involves the pyrolysis of vapor phase mixtures of metalorganic group III compounds and group V hydrides or metalorganics, transported in a carrier gas (usually H_2); the technique was pioneered by Manasevit in the early 1980s [23]. Control over the growth rate and crystal quality in MOCVD requires an understanding of competing processes driving the reaction: Mass transport and kinetics [24]. The complexity of these interacting processes is reflected in the models of the MOCVD process [25-27].

Mass transport in MOCVD occurs via diffusion through the gas phase adjacent to the growing solid surface and involves the hydrodynamics of the vapor passing through the reactor coupled with the diffusion characteristics of the reactant species [28]. In conventional horizontal MOCVD reactors, the gas flow dynamics leads to the formation of a boundary layer at the stationary substrate surface. As shown in Figure 2.1, this layer increases in thickness in the direction of the gas flow, resulting in a so-called stagnant layer which limits the transport of reactants to the substrate surface [22].

It has been clearly determined that the growth-rate-limiting step in horizontal reactors is mass transport and diffusion in the gas phase in the temperature range 550° to 750°C [18]. In this temperature range the surface catalyzed pyrolysis and surface diffusion of reactants is significantly faster than the diffusion of source molecules through the boundary layer, so that the gas phase at the growing surface is essentially depleted of reactants. Thus the driving force for the reaction is the difference in chemical potential due to the concentration gradient across the boundary layer. The difference in chemical potential between the gas phase at the solid surface and the solid surface itself is essentially zero, because the surface reactions have reached near-equilibrium [18].

Horizontal MOCVD reactors generally operate in the mass-transport limited regime due to the rate-limiting effect of the boundary layer. Under these conditions the growth rate is essentially independent of temperature and directly proportional to the flux of the Group III source material arriving at the growing surface. Surface kinetics limits

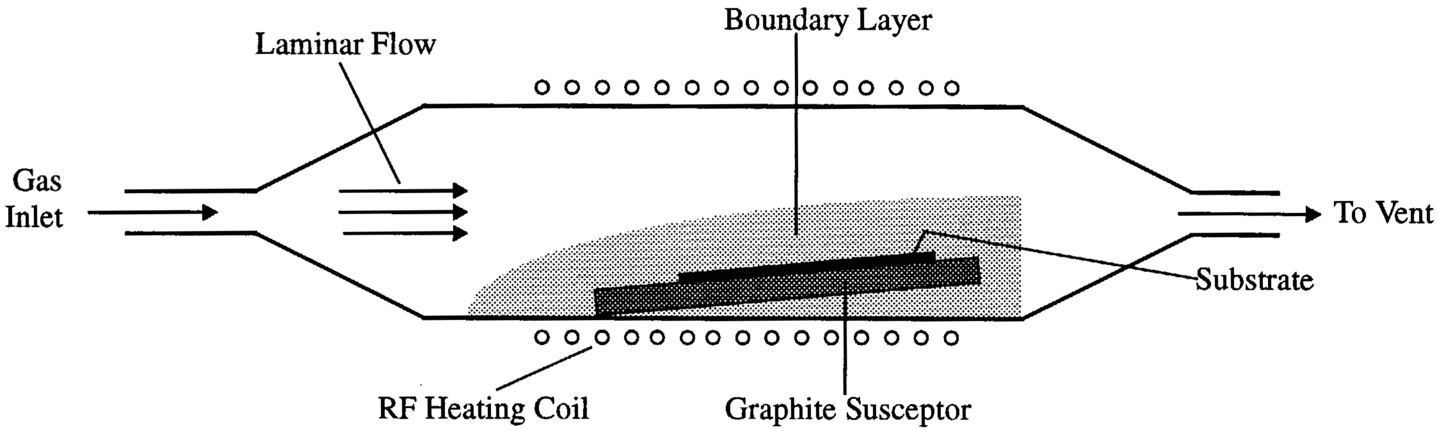

Figure 2-1 Boundary Layer in a Horizontal MOCVD Reactor

the rate at which arriving reactants pyrolyze and adsorb, migrate on the surface to energetically favorable positions, and desorb. Only when the diffusion rate through the boundary layer exceeds the decomposition rate of the reactants on the surface do catalytic effects at the surface become important [22].

2.3.1 Atmospheric Pressure MOCVD

The least complex MOCVD systems operate at atmospheric pressure. Flow behavior and memory effects in horizontal atmospheric pressure (AP) MOCVD reactors have been extensively studied [29, 30]. Ideal laminar flow is rarely achieved in real reactors [31]. Disturbances of the laminar pattern due to a barrier in the flow path, a change in tube diameter, high inlet gas velocity, or buoyancy effects due to temperature gradients result in vortices in the gas flow which cause memory effects in the reactant concentration and make rapid switching of the gas phase composition difficult [27]. Turbulence effects are particularly strong in AP reactors, in which high flow rates are necessary to achieve rapid switching of the gas composition [22].

The engineering details of the gas handling system in an AP-MOCVD reactor impose limits on the abruptness of heterojunctions grown in the system. High speed switching manifolds suitable for either continuous or interrupted growth have been designed to improve AP-MOCVD system performance [32, 33]. These designs have focused on (1) minimizing unpurged areas in the manifold and in the reactor which act as virtual reactant sources due to retention of gases, (2) minimizing pressure perturbation during switching by using a vent/run switching configuration, and (3) minimizing interdiffusion of gases in the manifold by keeping the distance from the switching point to the substrate as short as possible [33]. All of these factors (deadspace, pressure variations, and mixing in the entrance manifold) inhibit rapid changes in vapor phase composition and preclude the formation of abrupt compositional changes in the solid.

2.3.2 Low Pressure MOCVD

Since hydrodynamics are mainly dependent on reactor geometry and on total system pressure, reactors operating at low pressure were developed in an attempt to decrease the turbulence problems associated with atmospheric pressure reactors. Low pressure (LP) MOCVD reactors are operated in the range 10^{-2} to 300 Torr [22]. In this pressure range mass transport is still characterized by viscous rather than molecular flow, but there is a marked decrease in turbulence [27] and an improvement in compositional and thickness uniformity due to the enhanced diffusivity of reactant species at lower pressures [22]. Successful growth of $(GaAs)_m/(AlAs)_n$ superlattices has been demonstrated in LP-MOCVD [34]. LP-MOCVD is suitable for large-area scaleup to volume production equipment where increased dimensions make recirculating currents nearly unavoidable at atmospheric pressure. However, the Group V hydride consumption increases dramatically, and reactant usage in general is less efficient. The vacuum equipment required for LP-MOCVD brings with it the same increase in complexity, expense, and maintenance which is characteristic of MBE.

2.4 MOCVD in Vertical Reactors

The dependence of flow characteristics on reactor geometry has led to numerous attempts to improve the quality of crystals and the abruptness of interfaces by optimizing various aspects of reactor design. Horizontal reactor design has been improved by using angles less than 7° when changing the diameter of the reactor chamber, by avoiding unpurged deadspaces, by constructing the vent/run input into the manifold at a position near the reactor inlet, and by various pressure balancing schemes [35]. Another approach to improving reactor performance has been to utilize the design considerations listed above in conjunction with a vertical reactor chamber.

2.4.1 The Conventional Vertical MOCVD Reactor

In the conventional or "top to bottom" vertical reactor, the gas stream enters at the top and flows downward over and around a horizontal substrate. In this configuration the laminar flow must compete with the directly opposing forces of buoyancy and gravity. Modeling of flow dynamics in conventional vertical reactors indicates that such configurations invariably produce recirculating regions when operated at atmospheric pressure, making rapid change of gas phase composition impossible [36-39]. Several approaches to minimizing turbulence in the conventional vertical reactor have been suggested, including inlet gas stream diffusers [38, 39] and rotating disks [40]. Some workers have achieved high purity AlGaAs in a conventional vertical reactor with a rotating substrate operated at 80 Torr [41], but the system is complex and junction abruptness remains a problem.

2.4.2 The Inverted-Vertical MOCVD Reactor

The natural convective forces can work in concert with the input gas velocity by inverting the gas flow so that the reactants enter at the bottom, flow past the substrate, and exit to the exhaust line at the top of the chamber.

In the inverted-vertical chimney reactor, the substrate or substrates are mounted vertically on the wall of the reactor and the gas flow from bottom to top is parallel to the substrate surface, as is the case in horizontal MOCVD reactors. The intent of this design is to create an upward convective flow near the susceptor, thus promoting rapid gas switching for growth of abrupt heterojunctions [18]. This configuration has great potential for scaleup to production because of the possibility of growing on multiple wafers in each run. Such a chimney reactor has produced GaAs/AlGaAs structures with atomically abrupt interfaces [42]. However, careful modeling of this configuration indicates that laminar flow is assisted by forced convection at low pressures, but that at atmospheric pressure complex flow patterns occur in a laminar mixed convection regime [43]. Asymmetrical flow and eddying are characteristic of this reactor design.

In the inverted-vertical stagnation point flow reactor, the substrate is mounted horizontally with the growing surface facing downward, and the gas flow from bottom to top is perpendicular to the substrate surface, creating a zero (or stagnation point) in the vertical velocity of the gas stream. Models of this flow configuration use the simplifying assumptions that operation is in the mass transport limited regime, that the reactants are dilute, and that the reactor is axially symmetric. Both one-dimensional and two-dimensional solutions to the hydrodynamic, thermal, and mass transfer equations give an accurate picture of the deposition process [44], and indicate that the system parameters responsible for the disturbance of laminar flow are thermal recirculation regions, susceptor size, inlet size, and flow rate. Comparison of the model results from both AP and LP IV-MOCVD reactors with the model results from conventional vertical reactors indicates a marked decrease in recirculation currents in the IV configuration; these recirculation loops are, in theory, entirely eliminated in an IV-MOCVD reactor operated at low pressure [44].

Various nozzle [45] and shower-head [46] inlet configurations have been suggested to achieve a well-defined flow field in the short reactor residence time essential in producing abrupt heterojunctions. The nozzle schemes have the disadvantage of requiring an abrupt change in diameter of the flow path from the nozzle to the reactor chamber, which is known to cause recirculation loops in any reactor configuration [27, 45]. The shower-head arrangement requires that the "stand-off distance" between the gas inlet and the heated substance be very short, on the order of 2-3 cm. This results in the possibility of premature heating of the precursor gas in the inlet. When this problem is solved by keeping the temperature of the distributor below the decomposition temperature of the reactants, there is the possibility of incomplete pyrolysis due to the spatial limitation of the pyrolysis zone (this issue is discussed in greater detail in the next section). However, experimental evaluation of both these gas inlet arrangements indicate that recirculation is decreased at AP and essentially eliminated at LP [45, 46].

2.4.3 The IV-MOCVD System with Fast-Switch Manifold

The inverted-vertical MOCVD reactor with fast-switch manifold used in this work was designed to minimize thermal recirculation loops [47]. It was predicted that this rigorous design would improve heterojunction abruptness in material grown at atmospheric pressure and thus eliminate the need for low pressure equipment. The components of the reactor design include the IV configuration to make use of the buoyancy effect, the gradual changes in gas flow path diameter, axial symmetry, the elimination of unpurged deadspace in areas of the reactor upstream from the substrate, a unique fast-switch manifold to minimize pressure variations [32], and a vent/run input into the manifold positioned as close to the reactor inlet as possible.

The reactor assembly, shown in Figure 2-2, is made of fused quartz and includes a 2mm water cooling jacket, a pyrolytic boron nitride (PBN) pedestal, and a graphite susceptor. The angle between the reactor axis and the chamber walls in the inlet portion of the reactor is 11.5°, the smallest angle which can be reproducibly made by conventional glass shop techniques. The pedestal-susceptor-substrate assembly is positioned symmetrically with respect to the reactor chamber axis and has been described in detail elsewhere [47, 48]. Circular openings in the upper wall of the pedestal provide a flow path for gases to the reactor exhaust port.

The optimum flow rate in this reactor is defined as the total flow rate which minimizes recirculation loops near the reactor tube walls, and is determined by the exhaust pressure and by the smallest downstream cross-sectional area through which reactants must pass. The optimum flow rate to minimize the size of eddy currents and localize them to the reactor wall was determined to be 2.9 standard liters per minute (slpm) [47]. The optimum flow rate also minimizes the distance below the base of the pedestal at which deposits begin to form on the reactor wall. At 2.9 slpm deposits form from about one half inch below the base of the pedestal and up; this distance increases in the direction of the gas inlet when the total flow is either increased or decreased [47].

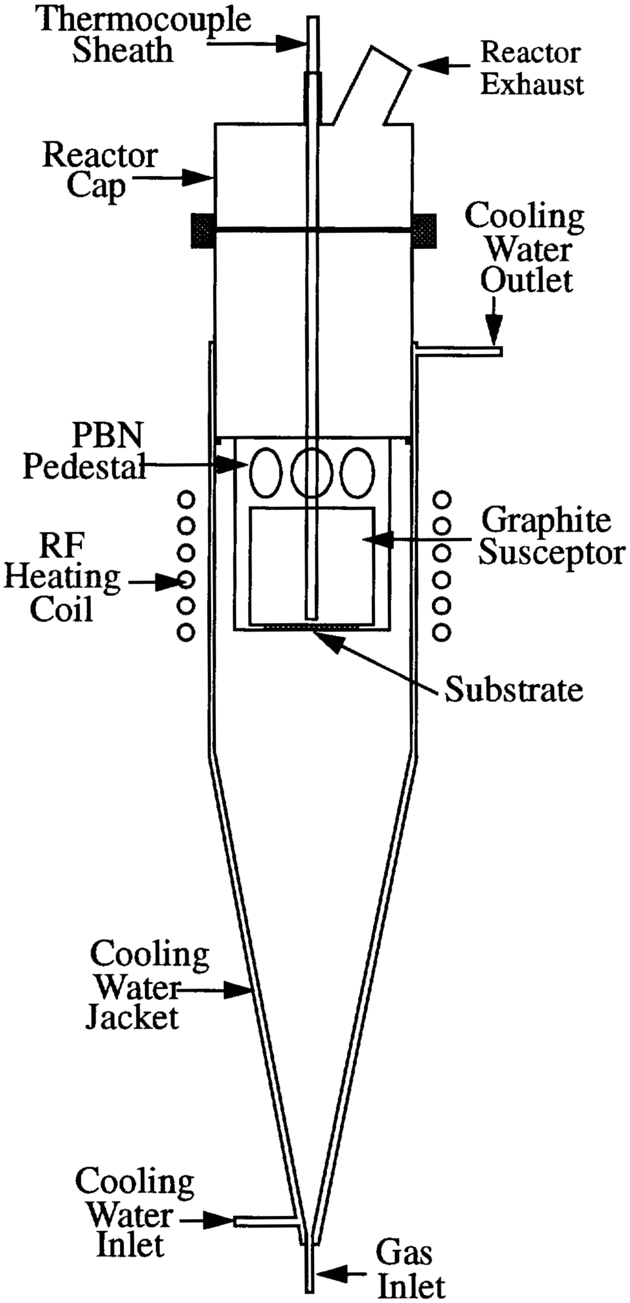

Figure 2-2 **The Inverted-Vertical MOCVD Reactor Chamber**

This observation (of the distance from the heated susceptor at which deposits form on the reactor wall) raises the interesting possibility that the shortening of the effective hot zone for pyrolysis in the IV configuration (Figure 2-3) may lead to an increase in the role of surface kinetics and surface catalyzed pyrolysis relative to the role of mass transport and diffusion in the vapor phase. In this configuration the thickness of the boundary layer through which reactants must diffuse to reach the growing surface is decreased due to the fact that the inlet gas velocity is perpendicular to the substrate and all reactant species have a momentum component assisting diffusion. These characteristics together lead to a situation in which diffusivity is increased and the area in which pyrolysis may occur is decreased. It has been suggested that this reactor configuration operates in a mixed mass transport limited and kinetically limited regime [49]. Other workers have observed similar pyrolysis limited behavior [50-53]. The Arrhenius plot of growth rate versus inverse temperature for this IV-MOCVD system (shown in Figure 2-4) indicates a temperature dependence of growth rate proportional to the exponential of the activation energy for surface pyrolysis, $R_g \propto Ae^{-E_a/RT}$, which confirms a kinetic component of growth rate in this configuration.

Good control of doping profiles, layer thicknesses in GaAs and AlGaAs, and compositional uniformity in AlGaAs have been demonstrated in this IV-MOCVD reactor operating at atmospheric pressure [47, 54]. The current work focuses on characterizing the fast-switch manifold and evaluating its effectiveness in achieving atomically abrupt heterojunctions in atmospheric pressure growth.

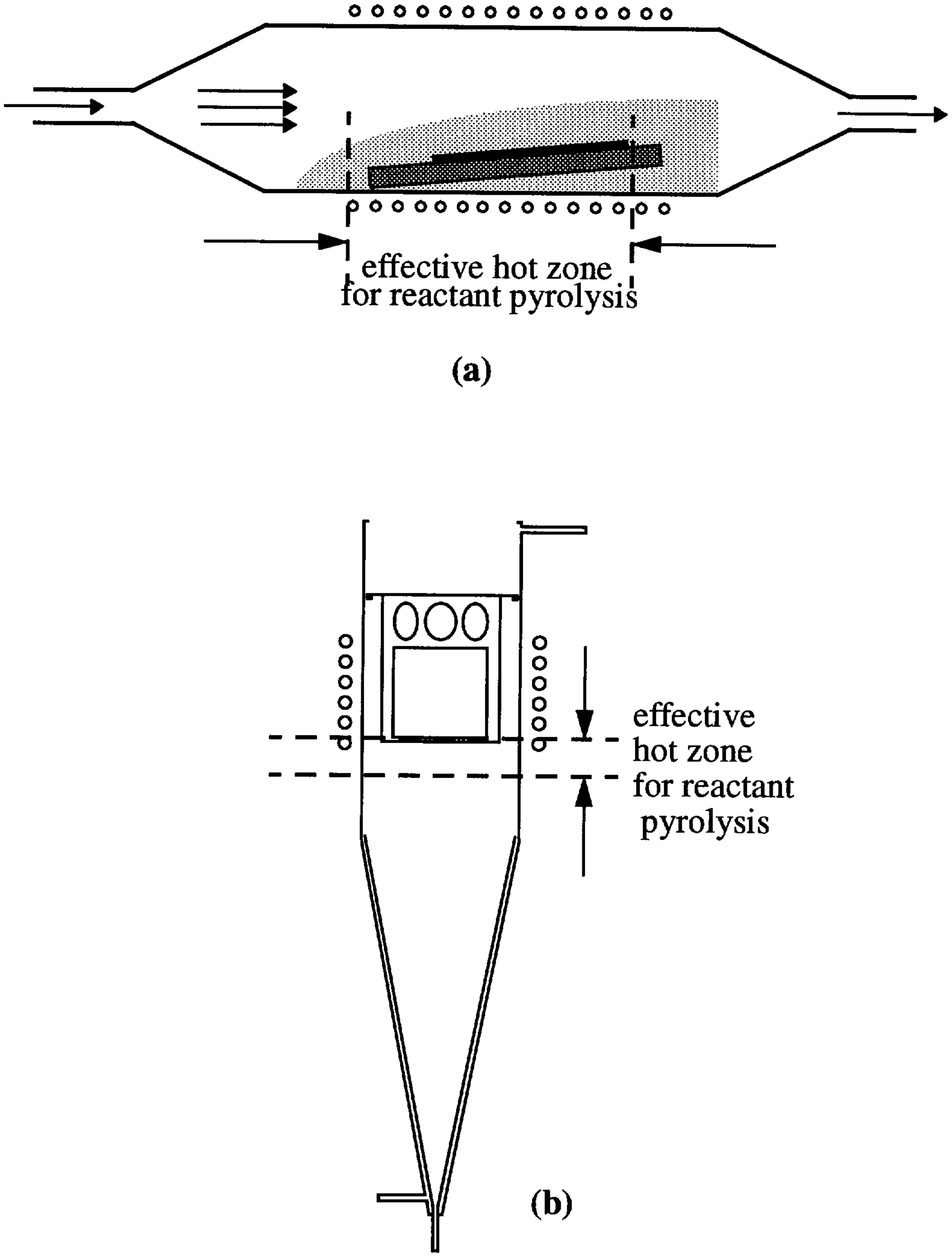

Figure 2-3 Hot Zone Length in Horizontal (a) and Vertical (b) Reactors

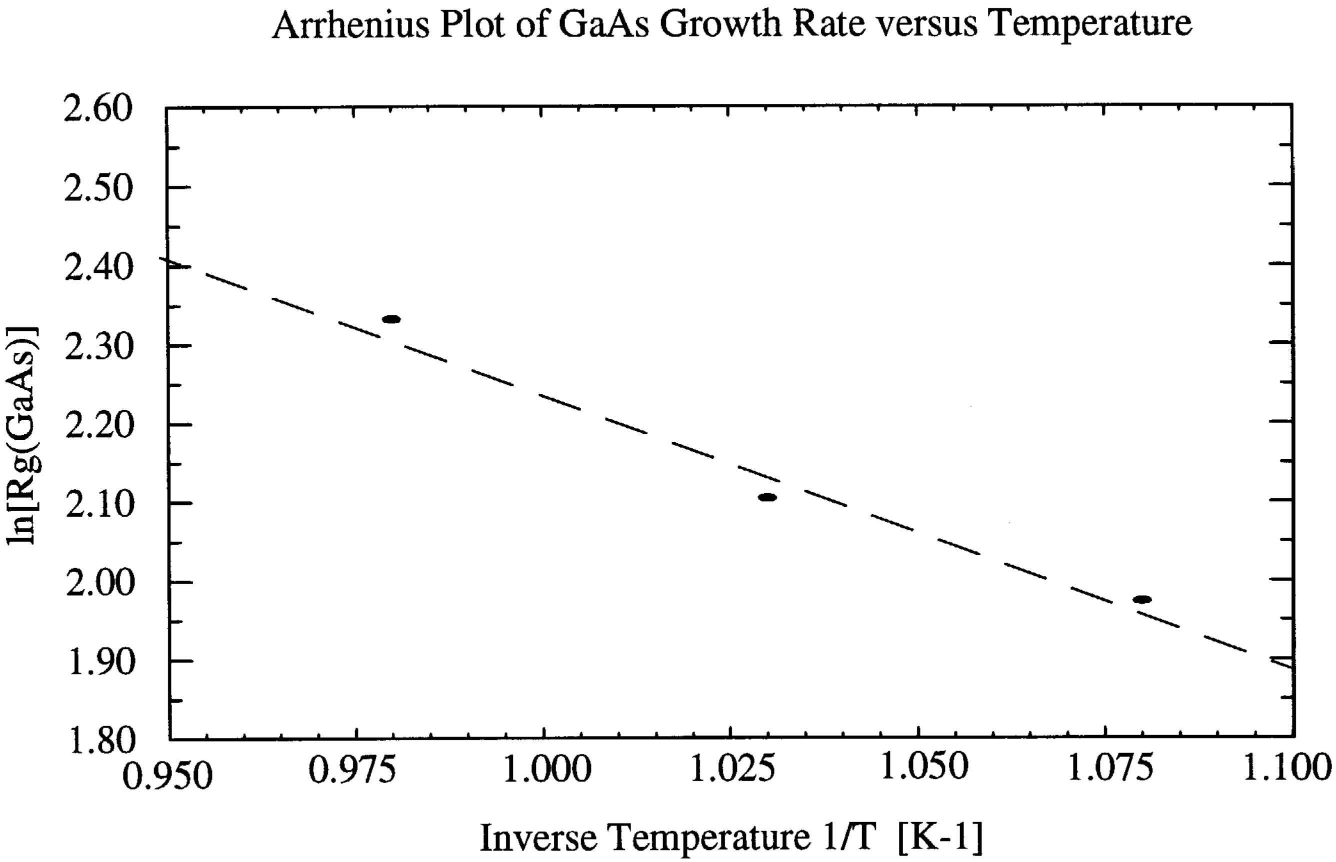

Figure 2-4 Arrhenius Plot of GaAs Growth Rate

2.5 Modulated Beam Flow Epitaxy

New growth techniques have recently been developed to increase control of the deposition process by growing in the kinetically limited growth regime [24]. These techniques use synchronized modulated or alternating flows to achieve layer-by-layer growth in migration enhanced epitaxy (MEE), atomic layer epitaxy (ALE), and flow-rate modulation epitaxy (FME). The advantages of these techniques are the superior morphology of surfaces and interfaces, especially for lattice-mismatched systems, and the lowering of required growth temperature for high quality material [22].

Large areas of III-V binary and ternary compounds with very good thickness uniformities have been grown by atomic layer epitaxy and by migration enhanced epitaxy [55, 56]. Unintentional carbon doping has limited control over doping profiles. The growth of high purity GaAs and AlGaAs with good control over doping profiles has been demonstrated by FME [57], although layer thicknesses were less uniform. These techniques are all low pressure processes and require the installation and maintenance of vacuum equipment.

2.6 Summary

Non-laminar flow, turbulence, and recirculation currents are characteristic of all MOCVD reactors; these problems must be eliminated or controlled to achieve the growth of abrupt heterojunctions. These issues may be addressed by lowering total reactor pressure and/or by various geometrical arrangements. The purpose of all approaches is to strive for laminar flow, suppress recirculation and turbulence, and keep the boundary layer between the free flowing gas phase and the substrate as uniform in thickness as possible. Figure 2-5 illustrates the results of various geometries in achieving these goals. The reduction of total reactor pressure in any given geometric configuration will improve the hydrodynamic characteristics of that reactor.

A comparison of epitaxial techniques available for the growth of quantum-size devices in the GaAs/AlGaAs system is presented in Table 2-1. The growth techniques of MBE, AP-MOCVD, LP-MOCVD, and the AP-IV-MOCVD system used in this work are evaluated and compared in cost, complexity, throughput, scalability, purity of material grown, thickness and compositional uniformity achievable, abruptness of heterojunctions, and concentration of interface traps. For the AP-IV-MOCVD system, the evaluation of material quality, interface abruptness, and concentration of interface traps is deferred to the end of this investigation.

In general, epitaxial systems operating in the kinetically limited regime, such as MBE and MOMBE, demonstrate faster switching of reactants due to the absence of the boundary layer which acts as a reservoir of reactant species. To insure the absence of the boundary layer, these systems require molecular flow rather than fluid flow of gases, and they therefore must operate under ultra-high vacuum conditions. The requirement for molecular flow limits growth rates to 1-2 μm/hr for GaAs. Slower growth rates are associated with increased incorporation of residual contaminants, particularly oxygen [18]. The temperature dependence of growth rate necessitates precise temperature control, as fluctuations in temperature may cause undesirable variations in growth rate. In addition,

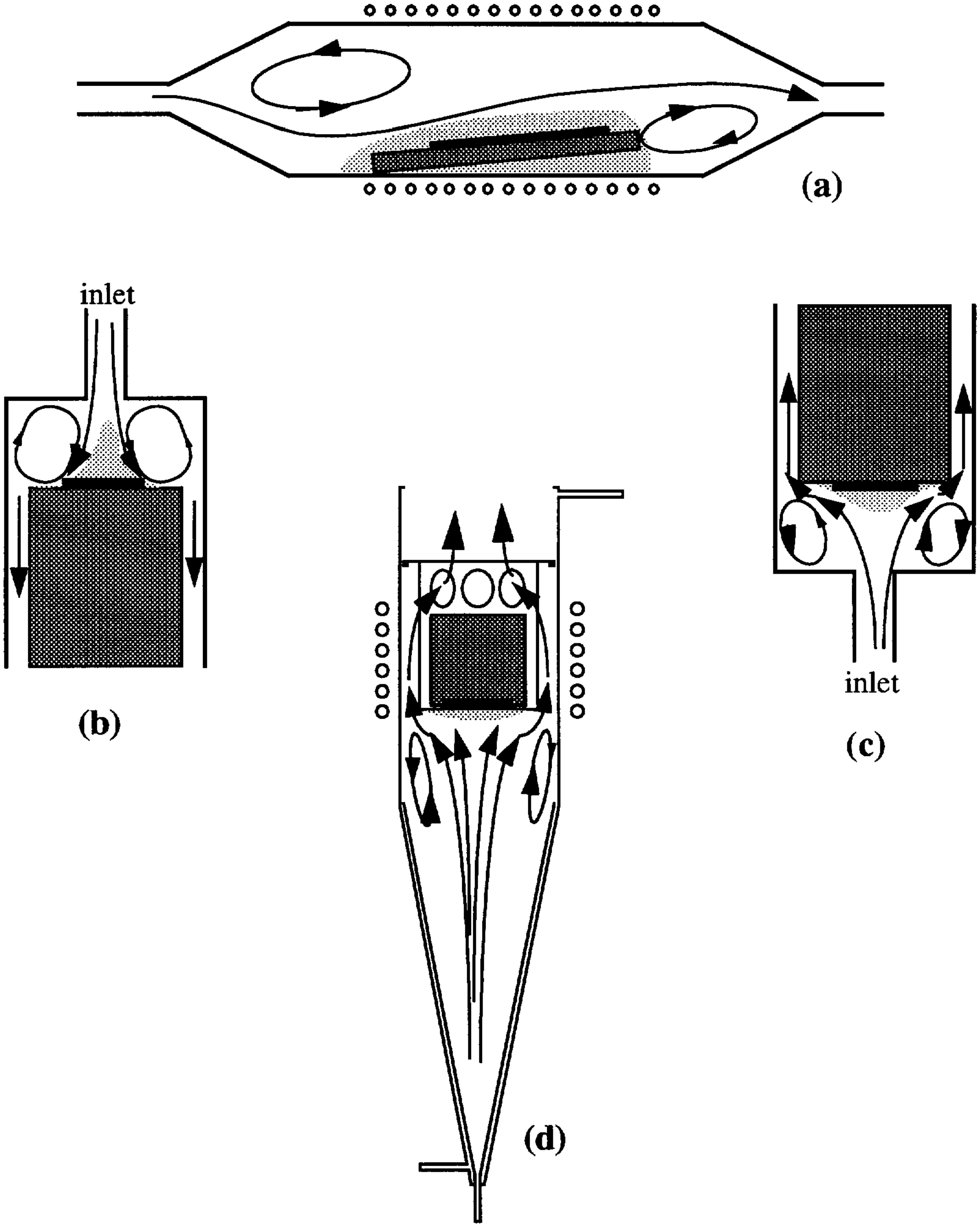

Figure 2-5 Forced Convection and Boundary Layer Formation in (a) horizontal reactor; (b) conventional vertical reactor; (c) IV reactor with nozzle inlet; and (d) AP-IV-MOCVD used here.

Table 2-1 A Comparison of Epitaxial Techniques

Epitaxial Technique	Advantages	Disadvantages
MBE	• High purity. • Good thickness & composition uniformity. • Good interface abruptness. [58-62]	• Cost & complexity (UHV equipment). • Low throughput. • Difficult to scale up. • Oxygen interface traps. [61-63]
AP-MOCVD	• Cost & simplicity (no vacuum equipment). • Improved throughput. • Good interface abruptness with growth interrupt. • Fewer interface traps. [59, 60, 63]	• Difficult to scale up. • Purity depends on precursors. • Some thickness & composition variation. • Graded interfaces without growth interrupt. [18, 22]
LP-MOCVD	• Cost. • Improved throughput. • Scalable. • Higher purity. • Good thickness & composition uniformity. • Good interface abruptness. • Fewer interface traps. [63-65]	• Complexity (vacuum equipment).
IV-MOCVD with fast-switch manifold	• Cost & simplicity (no vacuum equipment). • Improved throughput. • Good thickness & composition uniformity. • [Purity...] • [Interface abruptness...] • [Interface traps...] [54]	• Difficult to scale up.

temperature adjustments during growth may be necessary when growing different materials which are optimized at different growth temperatures, and thus the inherent advantage of fast switching in kinetically limited systems is lost during the temperature adjustment and stabilization interval.

In contrast, epitaxial systems operating in the diffusion limited regime, such as LP-MOCVD and AP-MOCVD, demonstrate slower switching of reactants due to the presence of the reservoir of reactants in the boundary layer. These systems operate under conditions of fluid flow. Switching time can be decreased by operating the system at lower pressures, as discussed in Section 2.3.2. Growth rates in diffusion limited systems are limited by the maximum volume flow of reactants through the system, and can be as high as 10 μm/hr for GaAs. In purely diffusion limited systems, growth rate is independent of temperature from ~600°C to ~800°C [18]. Since growth rates are not sensitive to temperature fluctuations in these systems, material quality may be optimized at different temperatures without affecting the growth rate. To achieve abrupt heterojunctions in diffusion limited systems, it is necessary to introduce a growth interrupt interval of sufficient duration to allow the reservoir of reactants in the boundary layer to entirely deplete before beginning growth of the next layer. These interrupt intervals are associated with increased incorporation of contaminants in certain materials, notably Al(Ga)As.

Epitaxial systems operating in a mixed diffusion limited and kinetically limited regime show the slower switching characteristics of diffusion limited systems and the growth rate dependence on temperature of kinetically limited systems. Growth rates can be as high as 10 μm/hr for GaAs, as in diffusion limited systems. Because of the complexity of the mixed regime, growth rates must be carefully calibrated to both reactant flow and substrate temperature. Precise temperature control is required, as fluctuations in temperature may cause variations in growth rate. A growth interrupt to allow depletion of the boundary layer is necessary for abrupt heterojunctions.

Chapter 3

Crystal Growth in the Atmospheric Pressure Inverted-Vertical MOCVD System

3.1 System Parameters

3.1.1 Materials Specifications

The carrier gas for this investigation was AirCo VLSI grade hydrogen (H_2). AirCo VLSI grade argon (Ar) was used as the purge gas. The reactant sources were AirCo VLSI grade 5.23% arsine (AsH_3) in H_2, Texas Alkyls semiconductor grade trimethyl gallium (TMGa), and Morton International semiconductor grade dimethyl aluminum hydride (DMAlH). All the gases, H_2, Ar, and AsH_3, were passed through Millipore gas purifiers before introduction into the manifold. The liquid sources TMGa and DMAlH were stored in Polycold bubblers which were kept in Neslab refrigerated recirculating heat exchangers to maintain constant liquid vapor pressure.

3.1.2 Reactant Control and Delivery

Precise gas flow control was accomplished by using regulators to maintain the gas pressures and electric mass flow controllers (MFCs) to meter the gas flow rates. Two-stage regulators were used to control the outlet pressure of the H_2, Ar, and AsH_3 cylinders; the downstream stages maintained constant inlet pressures to the MFCs which controlled gas flow from the cylinders to the reactor. In each liquid reactant source line an additional single-stage regulator was used in series with the H_2 gas cylinder regulator to control inlet pressure to the MFCs which controlled hydrogen flow through the bubblers. The purpose of the second regulator was to prevent pressure fluctuations when two or more liquid source lines were fed by the H_2 carrier gas. This configuration is illustrated schematically in Figure 3-1.

The method of transport for the liquid reactants was to have H_2 gas bubble through the liquid, saturate with vapor, and carry the vapor into the manifold. The amount of each liquid source transferred was calculated from the H_2 flow rate and the vapor pressure of the source at the bath temperature. The vapor pressure of TMGa was 33.59 mmHg at the bath temperature of -13°C. With a controllable H_2 flow range through the bubbler of 1-20 sccm (limited by the mass flow controller), the range of Ga source delivery was 1.657 to 41.432 micromoles per minute. The DMAlH vapor pressure of 1.023 mmHg at its bath temperature of 16°C and the controllable H_2 flow range of 10-200 sccm through the DMAlH bubbler resulted in an Al source delivery range from 0.566 to 11.319 micromoles per minute. This range of delivery rates allowed the growth of $Al_xGa_{1-x}As$ over the entire range of Al mole fraction.

The inlet manifold of the system was constructed with a vent/run configuration shown in Figure 3-1, which allowed the development of a steady-state flow of gas in the vent line prior to its introduction into the feed flow to the reactor. A special feature of this system was the fast-switch manifold, located 1.4m upstream from the reactor chamber inlet. The fast-switch manifold consisted of a unique switching valve designed to minimize dead-space and reduce pressure pulses produced by valve closures, an additional "makeup" manifold line complete with vent/run configuration in parallel with each source line, and a four-valve control circuit which allowed the source vent/run valves and the makeup vent/run valves for a given reactant to be switched simultaneously. The makeup line for a given source was set to the identical flow rate (but of H_2 only) as the source line, so that when the source flow was switched from reactor to vent (or vent to reactor), the

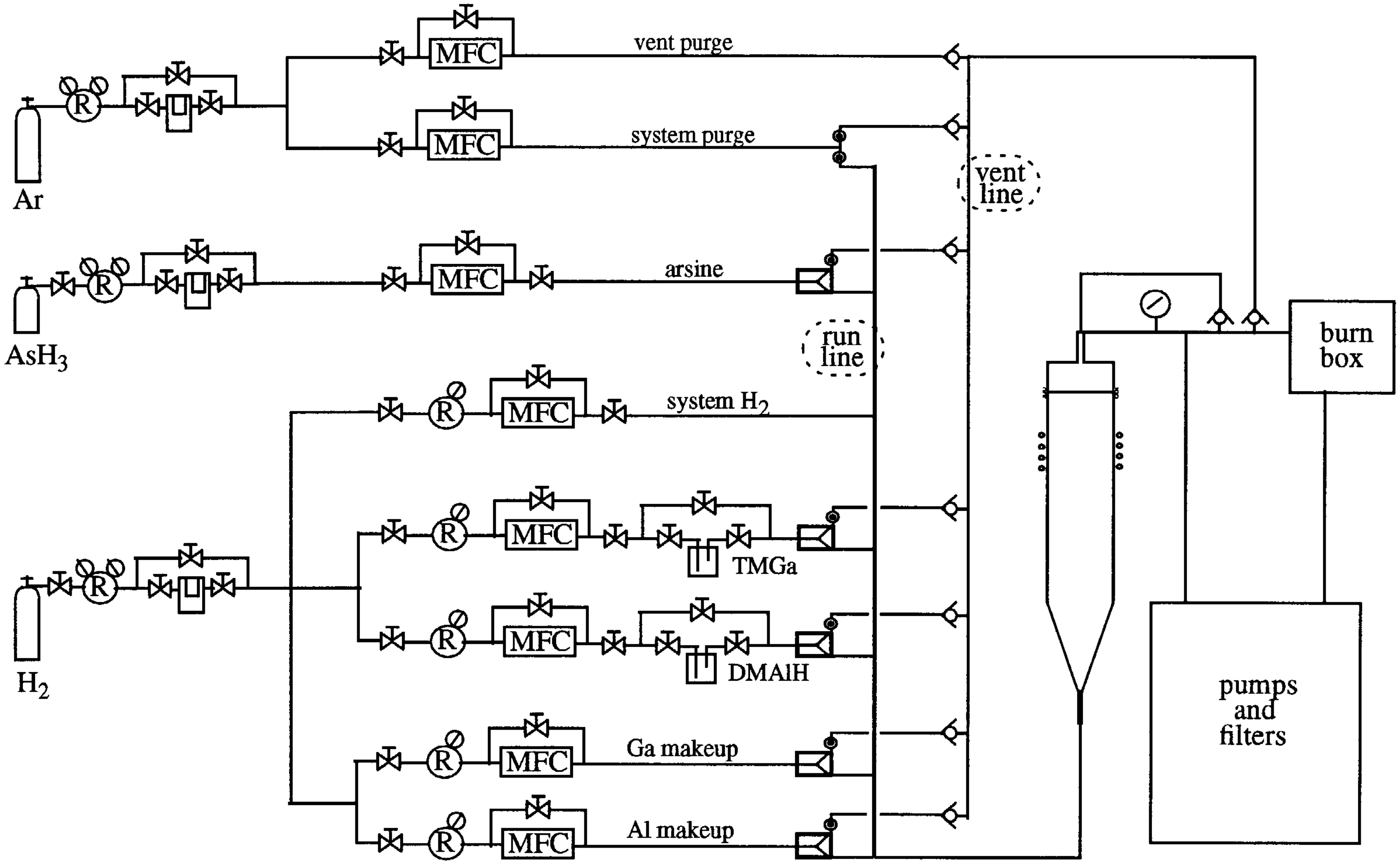

Figure 3-1 Partial Schematic of IV-MOCVD System

same volume flow without reactant in the makeup manifold was switched from vent to reactor (or reactor to vent), equalizing total system pressure as much as possible at all times. The inlets into the manifold for each source and its makeup line were positioned in pairs along the length of the manifold in order to minimize spatial variations during simultaneous switching, as shown in Figure 3-2.

3.1.3 Standard Operating Procedures

After the substrate was mounted and the reactor chamber closed, the system was purged with Ar. Argon flow was terminated and the system was then pumped down to approximately 30 Torr with a rotary vane roughing pump. Leak-tight integrity of the system was verified by further pumping with the turbomolecular pump to approximately 30 mTorr. The system was considered leak-tight if it held 30 mTorr for 5 minutes. There was frequently a slow rise in system pressure to about 50 mTorr during that interval. After the leakcheck, the system was pressurized with Ar to 5 psi for at least 10 minutes for a positive pressure check.

Once proper chamber closure had been verified by leakcheck and positive pressure check, the system was switched to H_2 flow and the heat cycle was initiated. The susceptor was inductively heated with a Lepel 12.6 kVA RF generator under the control of a Micristar PID heat processing controller. The temperature was monitored by an Omega type K thermocouple inserted into the susceptor. The heat cycle for GaAs substrates consisted of a temperature ramp from room temperature to 850°C over an interval of 10 minutes, followed by a rampdown from 850°C to the growth temperature of either 650°C or 750°C over an interval of 5 minutes. Arsine flow into the reactor was started at a rate of 1.57 sccm when the temperature reached 450°C during the ramp-up, increased to 3.14 sccm at 600°C, and increased again to 3.92 sccm at 725°C.

During the heat cycle, group III reactants were stabilized through the vent line at the flow rates desired for growth. For multilayer growth with the fast-switch manifold, H_2

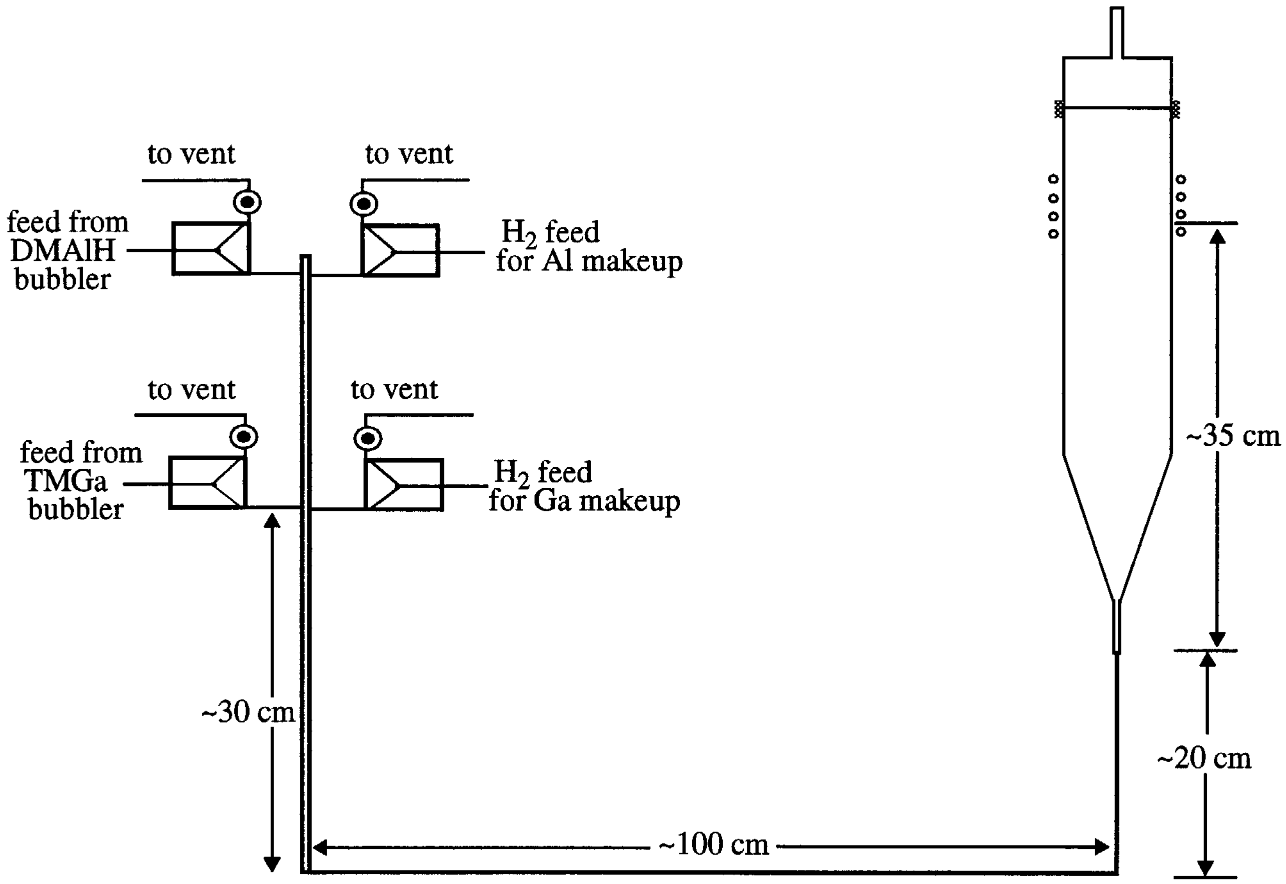

Figure 3-2 Switching Manifold Geometry

flows in the makeup manifold were stabilized through the reactor. Total reactor flow was maintained at 2.9 slpm throughout this process by adjusting MFCs. When the susceptor temperature had stabilized at the growth temperature, usually 3-5 minutes after the completion of the ramp-down, AsH_3 flow through the reactor was adjusted to achieve the required V/III ratio and group III reactant sources were switched from vent to reactor to begin growth. If the makeup manifold was in use, switching a group III source from vent to reactor automatically switched the makeup flow for that source from reactor to vent, keeping the total system flow (and therefore also total system pressure) constant.

After layers of the desired thickness and composition had been grown, group III reactants were switched to vent and the cooldown cycle was started. When the susceptor temperature had dropped to 450°C the arsine flow was stopped. Cooldown under H_2 continued until the temperature reached about 100°C. At this point Ar flow was started and H_2 terminated. The reactor chamber was opened under Ar flow and the grown sample removed.

3.2 Growth of Bulk Material

3.2.1 Substrate Preparation

All GaAs, AlAs, and AlGaAs samples for the growth rate and composition calibration studies were grown on 2 inch diameter mechanical grade semi-insulating (100) GaAs substrates from Bertram Laboratories. All mechanical grade substrates were evaluated for crystallinity by the double crystal rocking curve (DCRC) method. Substrates which diffracted at multiple angles were rejected for epitaxial growth. Only substrates with one diffraction angle were used for epitaxial growth. These substrates were degreased in hot 1,1,1-trichloroethane (TCE), acetone, and methanol for 5 minutes each, then thoroughly rinsed in deionized (DI) water and blown dry with nitrogen (N_2). This procedure was followed by a standard 7:1:1 H_2SO_4:H_2O_2:H_2O etch for 30 seconds to remove oxides and perform an etch-back on the substrate surface. Following the etch the substrates were blown dry in N_2 and immediately loaded into the reactor.

3.2.2 GaAs

Epitaxial layers of GaAs from 1μm to 8μm thick were grown for growth rate calibration at TMGa flow rates varying from 0.186 sccm to 1.500 sccm (8.286 to 41.432 micromoles per minute). In addition, samples were grown at substrate temperatures of both 650°C and 750°C. The V/III ratio was 30 for layers grown at 650°C and 20 for layers grown at 750°C. (The V/III ratio was reduced for the higher substrate temperature to conserve AsH_3. It is known that there is a marked increase in AsH_3 pyrolysis efficiency at higher temperatures [18]. Therefore this decrease in V/III ratio caused no degradation of morphology at the higher growth temperature.) The thicknesses of the layers were evaluated using Nomarski interference microscope photographs of samples etched for 2-3 seconds in A:B dislocation etch for III-V compounds [66-67]. The accuracy of these measurements is ±0.1μm.

Growth rates were calculated from the thickness measurements and the known growth times. The growth rate of GaAs grown at 650°C varied linearly with TMGa flow rate, following $R_g=7.24\times Q[\mathrm{TMGa}]$, where R_g is the growth rate in microns per hour and Q[TMGa] is the flow rate of TMGa in sccm. This fit resulted in a regression coefficient of 0.9777. The growth rate of GaAs grown at 750°C also varied linearly with TMGa flow rate, according to the relation $R_g=10.315\times Q[\mathrm{TMGa}]$ with a regression coefficient of 0.9942. These data and the linear regression functions are shown in Figure 3-3. No saturation of growth rate was seen in the range of reactant flow achievable through the MFCs currently in use on the system.

Other workers have found the growth rate of GaAs to be nearly independent of

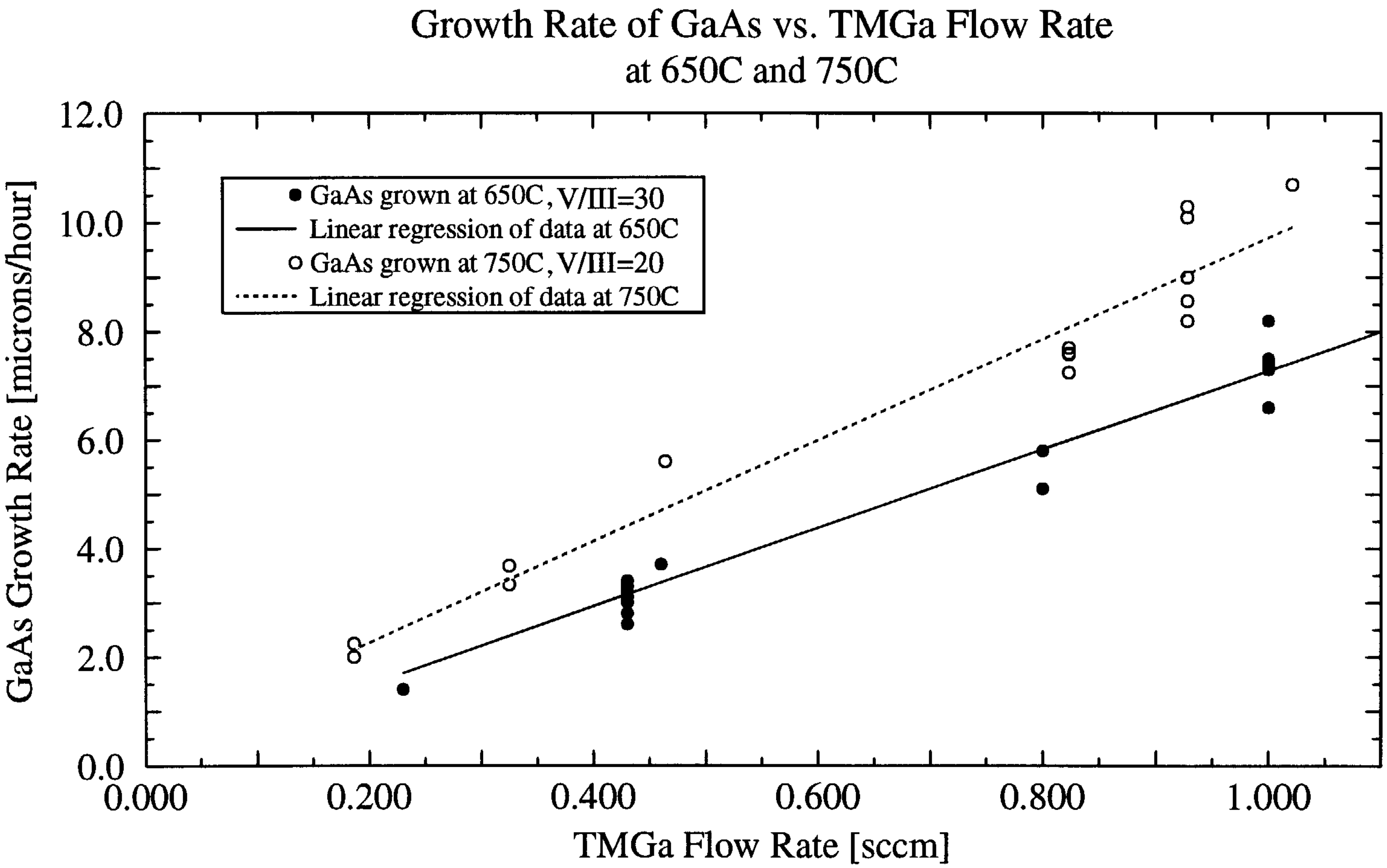

Figure 3-3 Growth Rate Calibration for GaAs

temperature in the range 550°C to 750°C in horizontal MOCVD reactors [68-69], and these observations have been taken as an unambiguous indication that the growth rate is mass transport limited under these conditions [18]. This is inferred from the fact that, since diffusion is nearly temperature-independent, growth rate is also nearly independent of substrate temperature in the mass transport limited case where diffusion is the rate limiting process. The data from the current investigation showing a first order temperature dependence of growth rate support the theory that growth takes place in a mixed mass transport limited and kinetically limited regime in the IV reactor configuration. This reactor geometry decreases pyrolysis efficiency by reducing the residence time in the heated region of the reactor and assists mass transport by reducing the thickness of the boundary layer and increasing the diffusivity of the reactants (see section 2.4.3 for a more detailed discussion of this interaction).

The highest purity GaAs is generally obtained at the lowest growth temperatures, in the range 600°C to 650°C [18]. It has been demonstrated that increasing the growth temperature increases carbon contamination in GaAs grown using TMGa [70]. However, the higher substrate temperature is required for the growth of good quality Al-containing III-V compounds due to the reactivity of Al, which forms strong bonds with both carbon and oxygen [71]. For AlGaAs material a reduction in oxygen contamination results from growth at temperatures above 720°C where the Al suboxide is volatile [72]. Therefore the GaAs growth rate at 750°C is pertinent to the growth of ternary compounds in later stages of this work.

3.2.3 AlAs

Epitaxial layers of AlAs from 1μm to 4μm thick were grown for growth rate calibration at DMAlH flow rates varying from 0.036 sccm to 0.254 sccm (1.641 to 11.318 micromoles per minute) and substrate temperatures of 650°C and 750°C. The V/III ratio was 30 for layers grown at 650°C and 20 for layers grown at 750°C. Layer thicknesses were determined by Nomarski interference microscope photographs of samples etched in A:B dislocation etch. Growth rates were calculated from the thickness measurements and the known growth times. The linear regression function at T_g=650°C was R_g(AlAs)=12.75×Q[DMAlH] (76% higher than GaAs) with a correlation coefficient of 0.9888. At T_g=750°C, the linear regression function was R_g(AlAs)=14.95×Q[DMAlH] (45% higher than GaAs) with a correlation coefficient of 0.9326. The data and the linear regression functions are presented graphically in Figure 3-4.

The growth rate of AlAs also showed a temperature dependence, although it was somewhat weaker than that observed for GaAs. This is possibly due to the more rapid diffusion of the Ga species in the gas phase [18] and the relatively greater stability of the Al precursor (with an activation energy for decomposition at these temperatures of 15-20 kcal/mole [73] as compared to ~5 kcal/mole for TMGa [72]). The temperature dependence does, however, imply that surface kinetics affects the growth rate of AlAs.

The surface morphology and crystal quality of AlAs showed considerable improvement when grown at 750°C. AlAs layers grown at the lower substrate temperature had cloudy, rough surfaces and produced broad, multi-peak rocking curves. In AlAs and AlGaAs growth, substrate temperature is known to play a significant role in residual donor and acceptor levels and in the incorporation of oxygen, which acts as both a deep-level trap and as a nonradiative recombination center [71]. Growth of AlAs at the higher substrate temperature was considered to be optimum for this process in order to improve the crystal quality and reduce oxygen incorporation. The use of DMAlH as a source material has also been shown to reduce oxygen incorporation in AlAs and AlGaAs compared to oxygen concentrations obtained using TMAl as a source, although compensation due to high levels of carbon incorporation was not reduced with the DMAlH precursor [74, 75].

It has been demonstrated that GaAs/AlGaAs quantum wells grown at 720°C have improved PL line widths as compared to QWs grown at 590°C with a two minute growth interruption, presumably because of decreased oxygen incorporation at the heterointerface

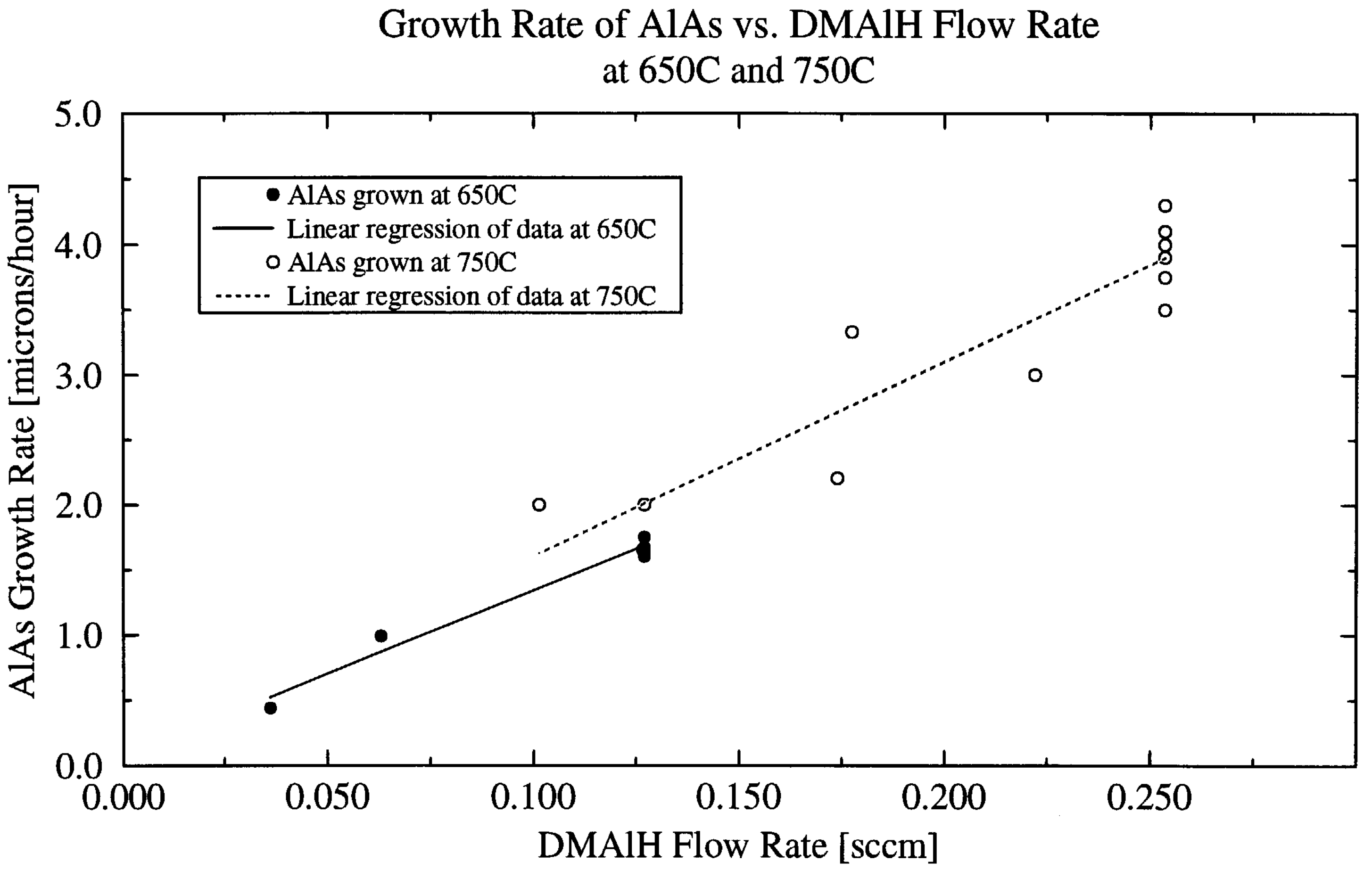

Figure 3-4 **Growth Rate Calibration for AlAs**

[76]. In order to improve the quality of the Al-containing materials, the standard process for all materials in this investigation was optimized for AlAs and all further growth of GaAs, AlAs and AlGaAs was performed at a substrate temperature of 750°C. In choosing to optimize growth conditions for minimum oxygen incorporation in the Al-containing layers, it was understood that the incorporation of carbon into both AlGaAs and GaAs layers would be increased.

3.2.4 $Al_xGa_{1-x}As$

Preliminary calculations of AlGaAs growth rate and composition were based on the assumption that the growth rate of any composition of the ternary compound would be an approximately additive function of the growth rates of binary GaAs and AlAs at the relevant flow rates. Using the growth rate functions for GaAs and AlAs determined from linear regression on the data previously collected, the growth rate of AlGaAs was calculated according to the relation $R_g(\mathrm{AlGaAs})=14.95\times[\mathrm{DMAlH}]+10.32\times[\mathrm{TMGa}]$. Values of Al mole fraction expected in the ternary material were calculated from the ratio of the calibrated growth rate of AlAs to the calculated growth rate of AlGaAs at the flows used, according to the approximate relation $x=R_g(\mathrm{AlAs})/\{R_g(\mathrm{AlAs})+R_g(\mathrm{GaAs})\}$.

Epitaxial layers of $Al_xGa_{1-x}As$ from 1μm to 4μm thick were grown for growth rate and composition calibrations at total Group III flow rates from 0.287 sccm to 1.274 sccm. Within this total flow range the ratio of the DMAlH flow to the total Group III flow was varied from 0.152 to 0.745, covering the range of Al mole fraction $0.20 \leq x \leq 0.80$ calculated as a result of the faster Al incorporation. The substrate temperature was 750°C and the V/III ratio was 20. Layer thicknesses were determined by Nomarski interference microscope photographs of samples etched in A:B dislocation etch.

Actual growth rates were calculated directly from the measured thicknesses and the known growth times. Linear regression was performed on this data and resulted in the growth rate function for $Al_xGa_{1-x}As$ over the entire range of composition investigated of

R_g(AlGaAs)=9.07×{[DMAlH]+[TMGa]} with a correlation coefficient of 0.9716. This relation indicates that the growth rate for ternary AlGaAs is less than the sum of the growth rates of AlAs and GaAs at the flow rates used; thus the relation in which Al and Ga flow rates are lumped in a single variable is not accurate. Since desorption of Ga is known to increase with temperature above 700°C [18, 72], the preferential incorporation of Al over Ga is suspected as the cause of the lowered growth rate. A two parameter fit to the growth rate data results in the function R_g(AlGaAs)=14.95×[DMAlH]+6.15×[TMGa] with a χ^2 of 0.2747. This fit supports the explanation that there is preferential incorporation of Al when Ga and Al are present together at elevated substrate temperatures. The initial growth rate calculation, these data, the linear regression, and the two parameter fit are presented in Figure 3-5. The variation of AlGaAs growth rate with Al to Ga ratio is shown in Figure 3-6. Lines of constant total Group III flow over the Al:Ga range are also shown for three total flow rates.

The composition of the $Al_xGa_{1-x}As$ layers was measured by the double crystal rocking curve (DCRC) technique. The x-ray diffractometry system will be described in detail in the next chapter. DCRC measurements on all AlGaAs samples showed Al mole fractions greater than those calculated using additive growth rates. A quadratic regression was performed on the data, which resulted in the function

$$x = 3.359 \times [Al\text{:III}] - 2.656 \times [Al\text{:III}]^2 \qquad \text{Eqn. 3-1}$$

where Al:III represents the ratio of Al flow to total Group III flow. The preliminary mole fraction calculations, composition data, and the mole fraction calculated using the quadratic fit are shown in Figure 3-7. These data also imply that Ga incorporation is decreased in the presence of another Group III element competing for cation vacancies at a substrate temperature of 750°C.

Six samples were grown at a [DMAlH] to total Group III ratio of 0.35 at growth rates which varied from 2.5 to 9.0 µm/hr in order to confirm a constant composition at different growth rates for the subsequent growth of superlattice and quantum well struc-

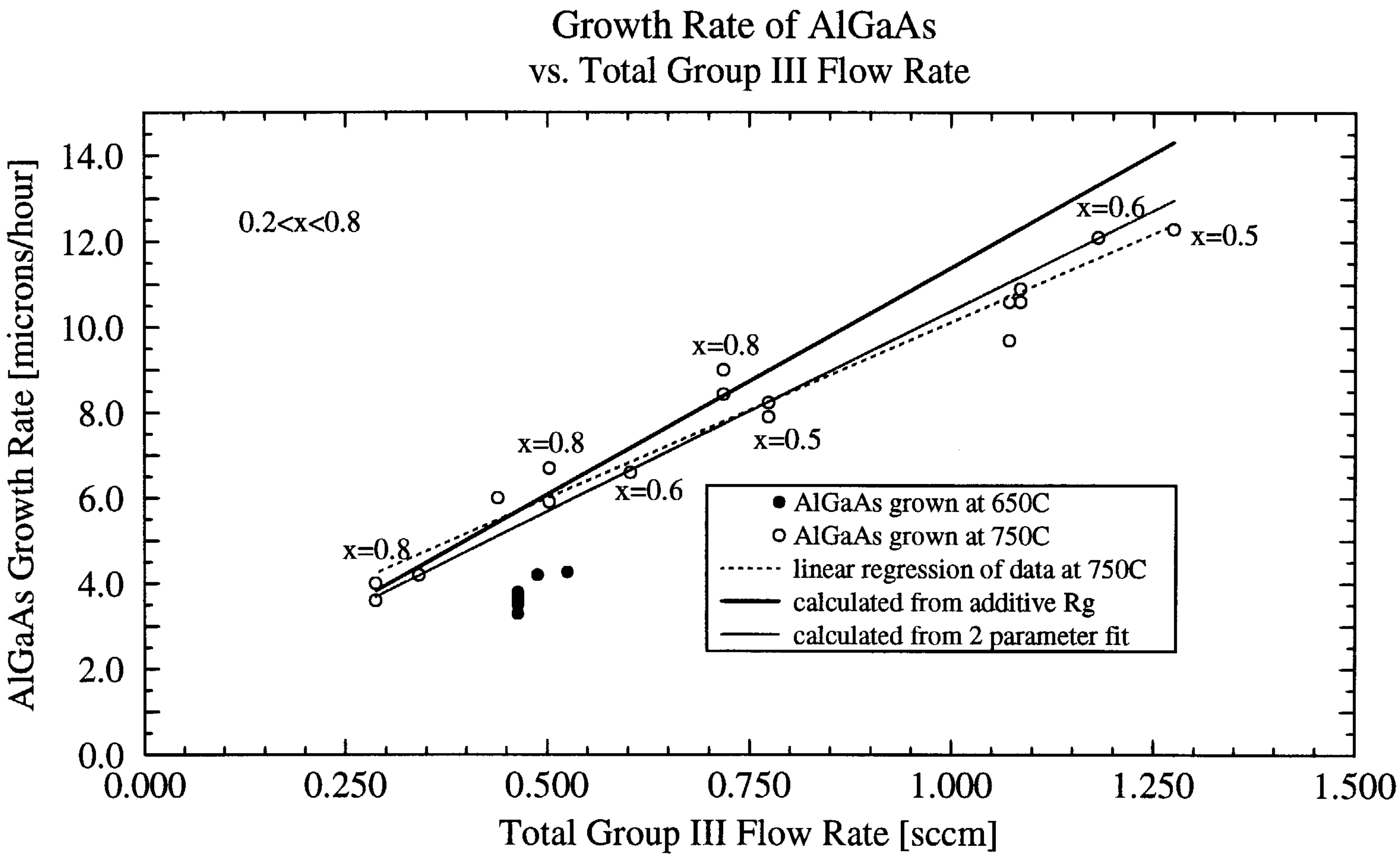

Figure 3-5 Growth Rate Calibration for AlGaAs

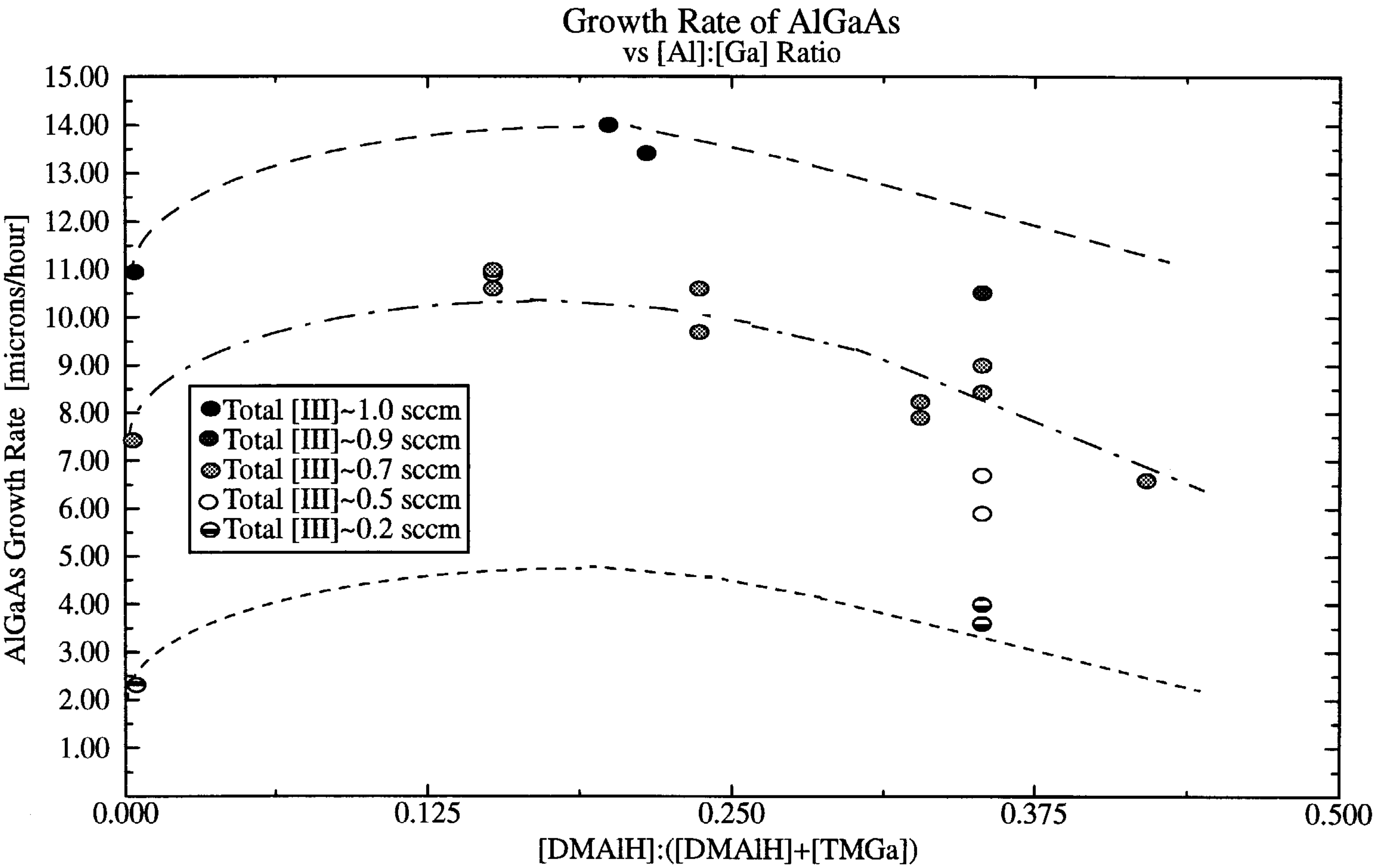

Figure 3-6 Growth Rate Calibration to Al:Ga for AlGaAs

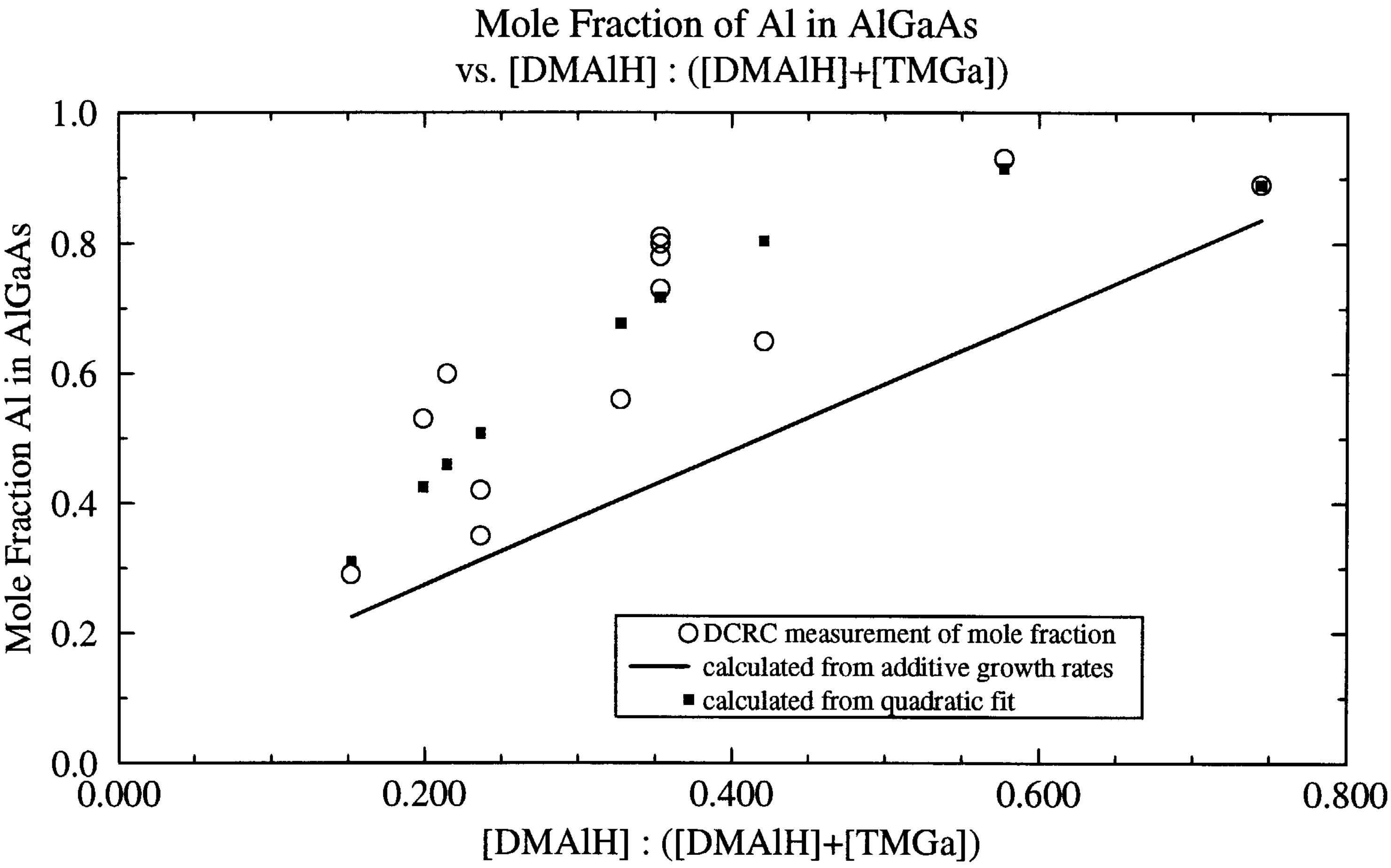

Figure 3-7 AlGaAs Composition Calibration

tures. Average Al mole fraction in these six samples was 0.79±0.03. Superlattices and quantum wells grown with this [DMAlH]:([DMAlH]+[TMGa]) ratio had measured average compositions consistent with this calibration point.

3.3 Growth of Superlattices and Quantum Wells

3.3.1 Constraints

Switching of the reactant sources on the AP-IV-MOCVD system was performed manually, and it was therefore necessary to evaluate system constraints before designing SL and QW structures. Manual switching introduced human error into the growth interval. It was determined that the switching error was ±0.5 seconds and that a growth interval of at least 10 seconds was required to reduce the switching uncertainty to no more than ±10%. This in turn placed a limit on the maximum growth rate which could be switched for a given layer thickness.

In addition to the maximum growth rate restriction imposed by manual switching, the decrease in the accuracy of MFCs in the bottom 10% of their flow range constituted a limit on the minimum flow rates, and therefore on the minimum growth rates. Since the MFC setpoints were controlled by manual potentiometers, it was necessary to set up steady-state flow before the growth period and leave the MFC flows constant throughout the run. Therefore the growth rates of both $Al_xGa_{1-x}As$ and GaAs had to conform to maximum and minimum constraints at constant flow.

Because TMGa vapor pressure at the bubbler temperature of -13°C is greater than that of DMAlH at the bubbler temperature of 16°C, mass transport of the Group III reactants was possible only over a limited range of Al:Ga ratios due to the maximum and minimum MFC volumes. The maximum achievable molar Al:Ga ratio (subject to maximum and minimum growth rate constraints) was therefore an additional limitation in choosing growth parameters. The Al mole fraction 0.80 was chosen for all barrier layers in SL and QW structures in order to meet the growth rate and mass transport constraints imposed by manual operation of the MOCVD system.

A range of appropriate layer thicknesses for the SL structure was determined from the DCRC system constraints on measurable SL satellite peaks (to be discussed in the next chapter). A 20 period superlattice structure was designed in which the nominal GaAs well thicknesses were 125Å and the nominal $Al_{0.8}Ga_{0.2}As$ barrier thicknesses were 225Å. These dimensions were chosen in order to meet the maximum and minimum growth rate requirements of the MOCVD system and simultaneously meet the requirements for measurable SL satellite peaks of the DCRC system. These dimensions are well below the pseudomorphic limit for AlAs on GaAs of ~3μm [17].

In superlattice structures, interface evaluation depends critically on the thickness uniformity of the SL layers, and therefore on switching precision. In QW structures, interface abruptness can be evaluated by PL independent of well width [77-79]; therefore the minimum switching interval was relaxed to 4 seconds for QWs in order to vary the well thickness from 25Å to 100Å at the same range of growth rates used for the SL structures.

3.3.2 Growth Parameters

The two independent variables of interest in this study of interface quality were growth rate and growth interruption interval. The growth rate range was restricted by manual system operation, as described above, to maxima of 3.0μm/hr for GaAs and 5.4μm/hr for AlGaAs, and minima of 1.5μm/hr (GaAs) and 2.7μm/hr (AlGaAs) at flow rates which resulted in a constant Al mole fraction of 0.8. One intermediate growth rate condition, 2.25 μm/hr (GaAs) and 4.0μm/hr (AlGaAs), was also evaluated. The growth parameters for all the SL structures grown in this work are presented in Table 3-1.

Reflection high energy electron diffraction (RHEED) from growing and reconstructed surfaces in MBE has shown that the surface of a material can be smoothed by interrupting the growth before deposition of a different material [80-81]. The smoothing is attributed to the increase in migration time during which the Group III cations may move on the surface to find energetically favorable positions at step edges. Previous work has determined that the improvement in interface quality due to the smoothing effect of growth interruption depends upon the interrupt interval [82-84] and the particular material being smoothed [85-87]. The details of this process will be discussed in Section 6.3.1. The effect of growth interruption on the surface of the material can be observed directly in

Table 3-1 Growth Parameters for SL Structures

Parameter	Minimum Growth Rate	Intermediate Growth Rate	Maximum Growth Rate
[DMAlH]	0.0761sccm	0.1141sccm	0.1521sccm
[TMGa]	0.1392sccm	0.2088sccm	0.2784sccm
Al MFC Setpoint	30%	45%	60%
Ga MFC Setpoint	15%	22.5%	30%
$R_g(Al_{0.8}Ga_{0.2}As)$	2.7μm/hr	4.0μm/hr	5.4μm/hr
$R_g(GaAs)$	1.5μm/hr	2.25μm/hr	3.0μm/hr
$t_g(Al_{0.8}Ga_{0.2}As)$	30s	20s	15s
$t_g(GaAs)$	30s	20s	15s
$d(Al_{0.8}Ga_{0.2}As)$ as designed	225Å	225Å	225Å
d(GaAs) as designed	125Å	125Å	125Å
Interrupt Interval	no interrupt	• no interrupt •10s interrupt	no interrupt

MBE through RHEED. In MOCVD the effect of growth interruption must be evaluated by indirect techniques [65, 84, 88-89]. In this work the effect of growth interruption on interface quality was evaluated by PL and DCRC.

Three SL structures without growth interruption were grown at minimum, intermediate, and maximum growth rates. An additional SL structure grown at the intermediate rate was interrupted at both the GaAs-on-AlGaAs (inverted) surface and the AlGaAs-on-GaAs (normal) surface. Due to the complexity of manual switching, no attempt was made to grow a SL with growth interrupted only at the normal surface. These superlattices were nominally identical and a schematic of the structure as designed is shown in Figure 3-8.

Quantum well structures were designed mainly for evaluation by low-temperature PL. The structures as designed consisted of four GaAs wells 25Å, 50Å, 75Å, and 100Å thick separated by approximately 300Å of $Al_{0.8}Ga_{0.2}As$. Three identical quantum well stacks were grown at the intermediate growth rate under different interrupt conditions: 1) no interrupt; 2) interrupt only at the normal surface; and 3) interrupt at both the normal and the inverted surfaces. The actual dimensions of the wells in each stack were estimated from the bandgap versus thickness model developed in Chapter 5. PL measurements (presented in Chapter 6) provided additional indirect data on actual well widths. A schematic of the quantum well structure as designed is shown in Figure 3-9.

3.3.3 Procedure

All superlattice and quantum well samples were grown on 2 inch diameter prime semi-insulating (100) GaAs substrates from Sumitomo. These substrates were all from the same boule and were certified to be oriented (100)2° off toward the nearest <110>±0.5°. The substrates were positioned for growth so that the major flat to minor flat direction was counterclockwise in order to insure identical orientation for all samples. Substrates were evaluated for crystallinity by the DCRC method and were found to be single crystal with a diffraction peak full width half maximum (FWHM) of ~13 arcsec-

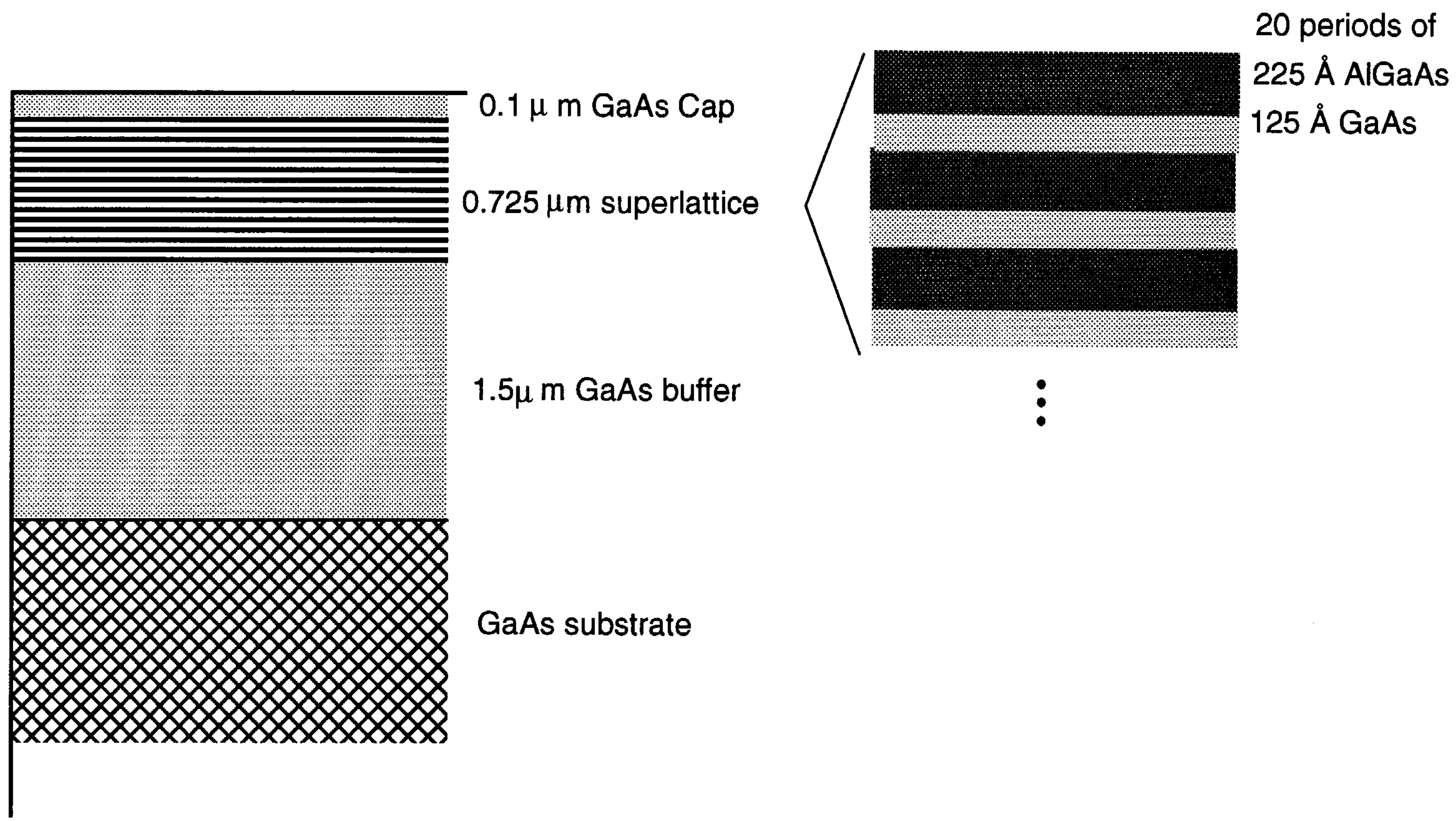

Figure 3-8 Superlattice Stack as Designed

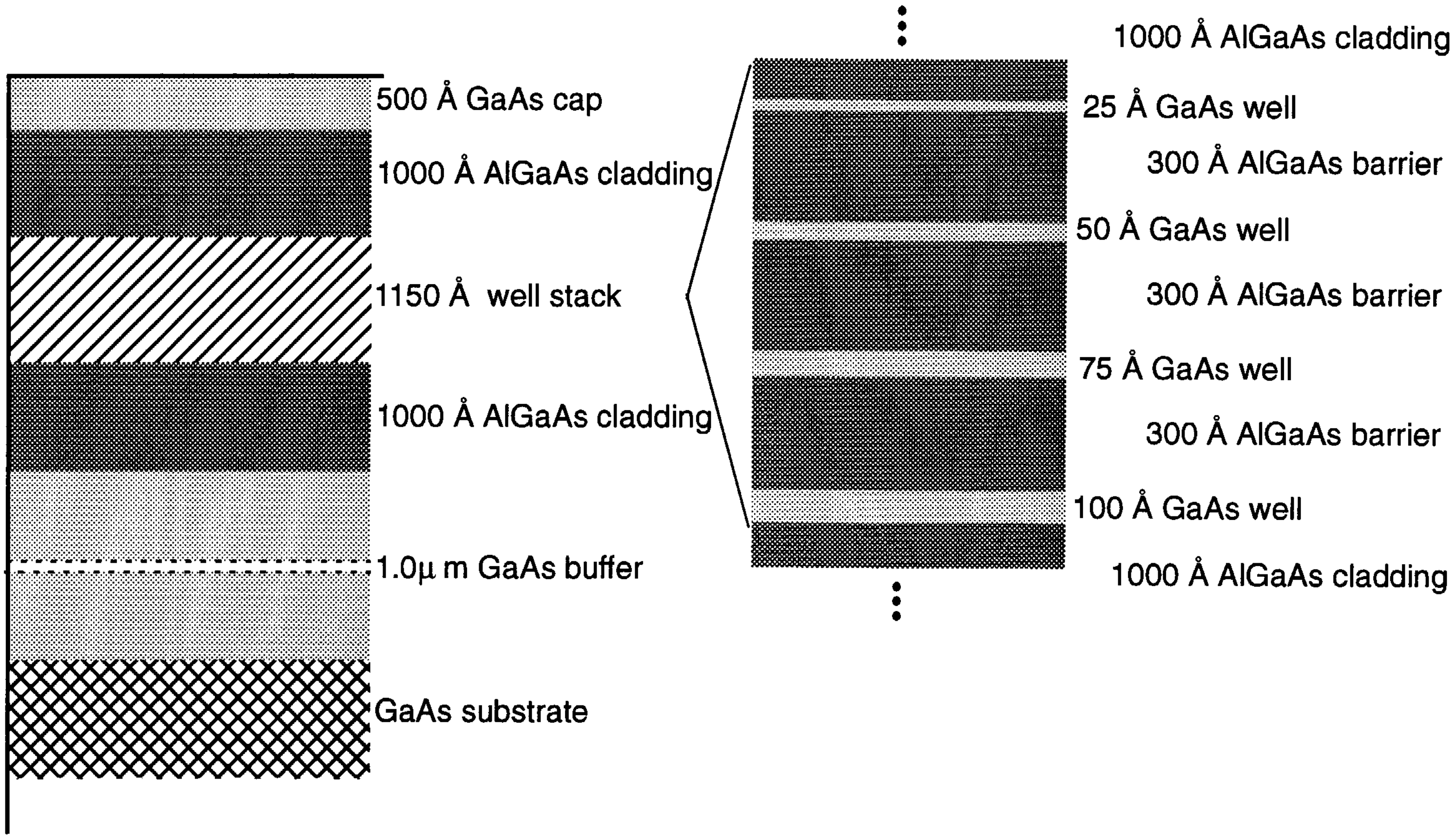

Figure 3-9 Quantum Well Stack as Designed

onds at an azimuthal orientation parallel to the direction of substrate tilt. Prior to growth, substrates were degreased and etched according to the procedure described in section 3.2.1.

Standard procedure was followed for sample mounting, leakcheck, and heat cycle. During heat-up reactants were stabilized to vent and H_2 flow in the makeup manifold was stabilized through the reactor chamber. Total system flow was maintained at 2.9 slpm throughout the growth and cooldown. Before beginning SL or QW growth, a 1.5μm buffer layer of GaAs was grown. To grow the required structures, DMAlH was switched in and out of the reactor chamber using four-valve control (which switched the identical volume flow in the makeup manifold) using a timing chart and a stopwatch. Two operators were present during all SL runs, one to monitor the timing chart and the other to monitor the stopwatch and switch the reactants. For SL and QW runs involving growth interrupts, the TMGa was also switched from run to vent as necessary in the interrupt period. For the runs without interrupt, the TMGa flow was constant throughout the run. After the desired structures had been completed, a 500-1000Å GaAs cap was grown on all samples. TMGa was then switched to vent and cooldown was started. Standard cooldown procedure was followed.

Surface morphology of the grown samples was evaluated by Nomarski interference microscope. The wafers were not cleaved for edge-on thickness measurements, but were kept intact for DCRC measurements across the entire wafer. DCRC measurements on the SL samples included a secondary measurement of total SL thickness. After DCRC had been taken on all SL and QW samples, the wafers were cleaved and specimens were prepared for photoluminescence measurements.

Chapter 4

Double Crystal Rocking Curve Measurements

4.1 X-Ray Diffraction from Semiconductor Crystals

X-ray diffractometry is a well established method for the measurement of the lattice parameter difference between epitaxial layers and substrates [4, 90-92]. Spacing between crystal planes can be determined from diffracted intensity versus angle of incidence data (rocking curves) collected at a constant x-ray wavelength, as the intensity versus angle function is highly sensitive to variations in the separation of reflecting planes [93]. Interpretation and simulation of rocking curves from multilayer structures have been extensively studied [5, 94] and this technique is well suited for the evaluation of interface roughness, thickness uniformity, and compositional grading [95, 96].

4.1.1 General Theory of X-Ray Diffraction

X-ray diffraction from crystals is an electromagnetic interference phenomenon. When an x-ray beam encounters a crystal composed of a regular arrangement of atoms, the x-rays are scattered by the individual atoms of the crystal with the direction of scattering dependent on the wavelength of the x-ray, the angle of incidence, the electronic structure of the atoms, and the atomic weight of the atoms [97, 98]. When the phase difference of the individually scattered x-rays is equal to $2n\pi$ (i.e., the path length difference is an integer multiple of the x-ray wavelength), the scattered x-rays mutually reinforce one another and a diffracted beam of measurable amplitude is created (provided that sufficient beam intensity is incident on the sample) [99]. The condition that the path length difference be an integer multiple of the x-ray wavelength is Bragg's law, $n\lambda = 2d(\sin\theta_B)$, which describes the required condition for constructive interference of scattered waves illustrated in Figure 4-1. When the angle of incidence is such that the path length difference is not an integer multiple of the x-ray wavelength, x-rays diffracted from the crystal planes are not in phase and do not interfere constructively, resulting in essentially no measurable diffracted beam. For radiation to penetrate the surface of a material, the wavelength must be less than the atomic spacing. Radiation with a wavelength on the order of 5Å or less is required in order to probe GaAs with an atomic spacing of ~5.65Å.

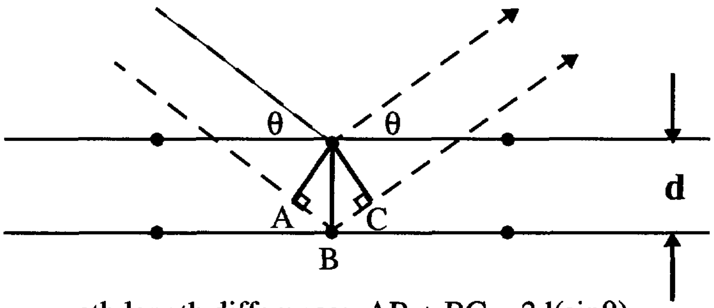

path length difference: $AB + BC = 2d(\sin\theta)$

Figure 4-1 The Bragg Condition

The intensity of the diffracted x-ray beam depends on the intensity of the incident beam, its direction relative to the crystal, and the crystal structure [99]. The diffracted intensity function exhibits sharp maxima for those scattering directions at which the Bragg condition is met for a family of parallel planes in the crystal. The angles at which these maxima occur are determined by the shape and size of the unit cell of the crystalline material [97]. X-ray scattering from planes parallel to the crystal surface (symmetrical reflection planes) and from planes not parallel to the surface (asymmetrical reflection planes) is illustrated in Figure 4-2.

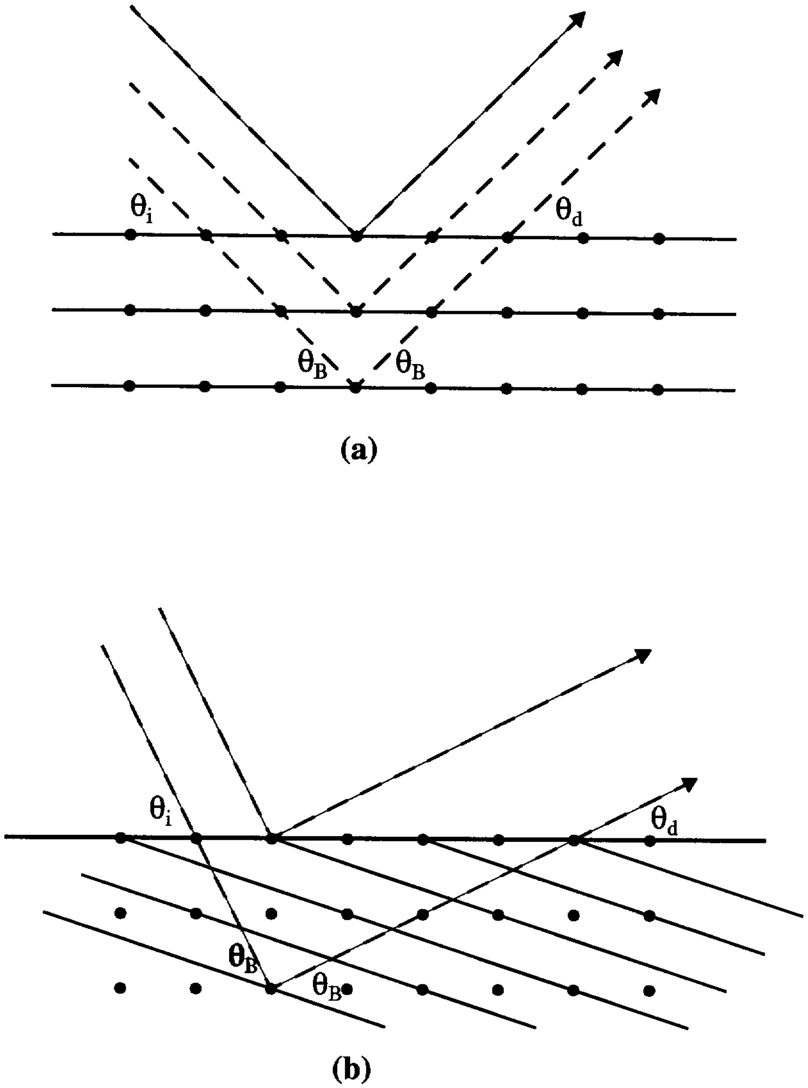

Figure 4-2 X-Ray Diffraction from Crystal Planes
(a) Symmetrical Reflection, and (b) Asymmetrical Reflection

For heteroepitaxial layers there is a difference in atomic spacing which is a function of the lattice mismatch between the layer and the substrate. This difference in interplanar spacing leads to a difference in the angles at which the Bragg condition is met in the epilayer and in the substrate for a given set of reflecting planes, as illustrated in Figure 4-3. The transformation of the angular separation of the diffraction maxima, $\Delta\theta$, into the relative lattice spacing difference, $\Delta d/d$, is accomplished by differentiating the Bragg condition to obtain the relation $\Delta d/d = -(\cot\theta_B) \cdot \Delta\theta$ [100].

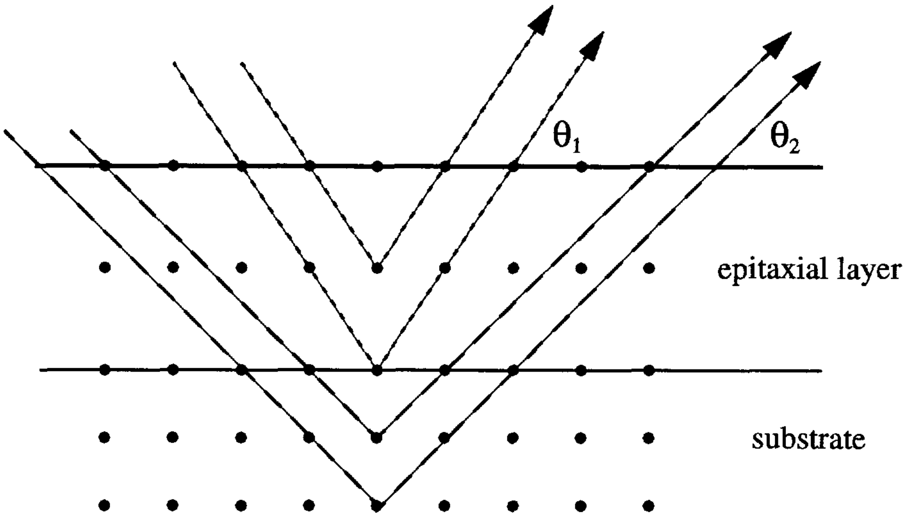

Figure 4-3 Diffraction Angles of Epilayer and Substrate

This relative lattice spacing difference depends upon the degree of tetragonal distortion necessary to accommodate the epilayer to the substrate in coherent epitaxy [102]. The distortion of the epitaxial layer results in a state of elastic strain which is characteristic of the material [15], and thus the elastic behavior of the material must be taken into account in order to determine the unstrained lattice constant and composition of the epitaxial layer.

4.1.2 Strain Measurements

The composition of an epitaxial layer can be calculated if the unstrained, or relaxed, lattice constant of the material is known. However, when a thin layer of a slightly different lattice constant is grown coherently on a single crystal substrate, the relaxed lattice constant of the layer cannot be measured directly due to the distortion of the lattice from its relaxed dimensions. In order to determine the relaxed lattice constant of the epilayer, the amount of distortion must be determined and the anisotropic elasticity of the distorted material must be taken into account [15]. It is necessary to consider the distortion both in the plane of growth and perpendicular to the plane of growth in order to evaluate the quality of the epitaxial layer and determine the exact composition of the layer [100-102]. The relations between the substrate lattice constant, the relaxed epilayer lattice constant, the actual epilayer lattice dimensions parallel and perpendicular to the plane of growth, and the crystalline quality of the epitaxial layer are presented in Figure 4-4.

In perfectly coherent epitaxy, the epitaxial layer has an in-plane lattice constant $a_{//}$ equal to that of the substrate, a_o, and is strained in the direction of growth so that it has a perpendicular lattice constant, $a_{\perp}$, which is equal to neither a_o nor to the relaxed lattice constant of the epitaxial material, a_r. In the case of perfect epitaxy in which $a_{//} = a_o$, the relaxed lattice constant of the layer can be computed directly (via the elasticity relation) from a measurement of the perpendicular strain in the layer. However, the epitaxial process is rarely perfect, even in low lattice mismatch systems such as GaAs/AlAs, and in general both components of strain are necessary for an accurate calculation of the relaxed lattice constant.

The angular separation of the diffraction peaks measured in the rocking curve is related to the relative difference in interplanar spacing of the reflecting planes, $\Delta d/d$ (section 4.1.1), rather than the difference in parallel or perpendicular lattice constants. However, relative difference in interplanar spacing can be expressed in terms of the Miller indices of the planes (hkl) and the angle ϕ between the reflecting planes and the surface of

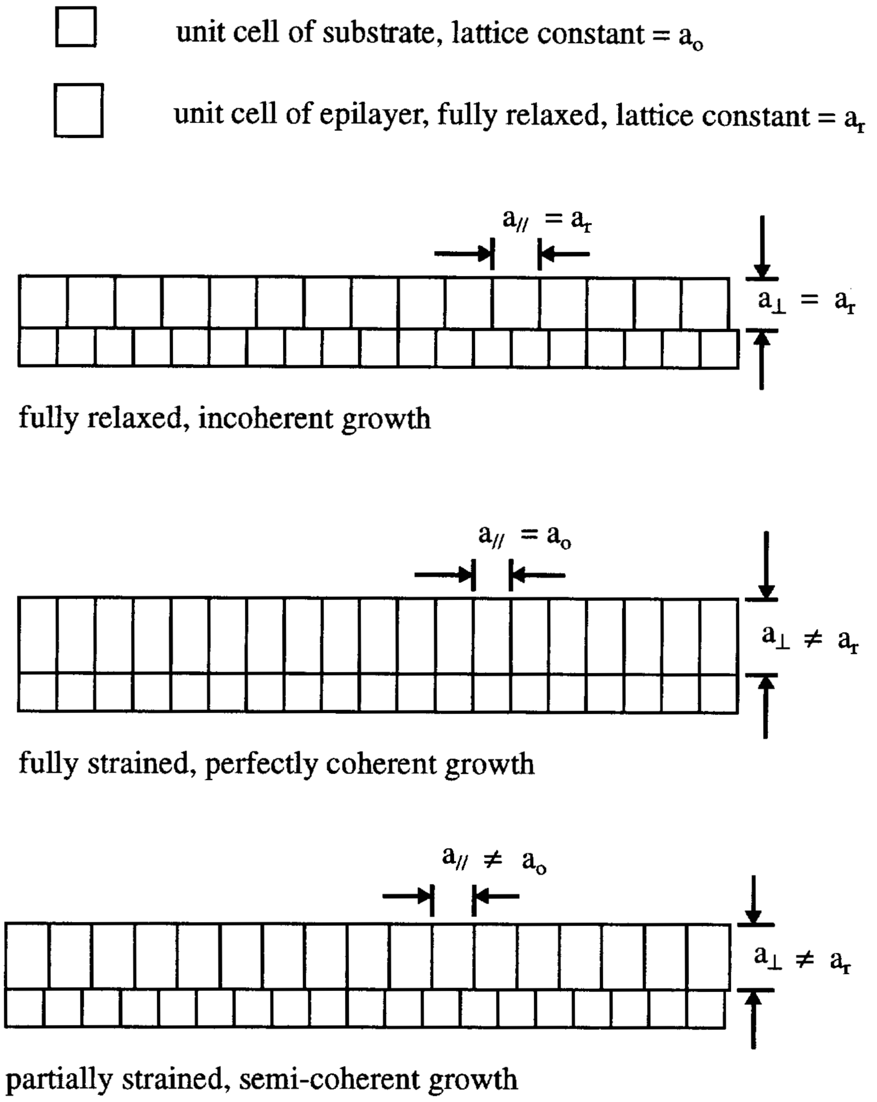

Figure 4-4 Epitaxial Quality & Components of Strain

the crystal using the relative difference in lattice constants, $\Delta a_{\perp}/a_o$ and $\Delta a_{//}/a_0$, as basis vectors according to standard crystallographic transformations for cubic crystals [103]. This results in expressions for lattice mismatch parallel and perpendicular to the direction of growth as a function of θ_B (known), ϕ (known), $\Delta\theta$, and $\Delta\phi$, where $\Delta\theta$ represents the difference in Bragg angle between the substrate and epilayer and $\Delta\phi$ represents the difference in the surface-to-reflecting-plane angle in the substrate and in the epilayer. This angular relationship is illustrated in Figure 4-5. The expressions for lattice mismatch as a function of peak separation are:

$$\frac{\Delta a_{\perp}}{a_o} = (\tan\phi) \cdot \Delta\phi - (\cot\theta_B) \cdot \Delta\theta \qquad \text{Eqn. 4-1}$$

$$\frac{\Delta a_{//}}{a_o} = -(\cot\phi) \cdot \Delta\phi - (\cot\theta_B) \cdot \Delta\theta \qquad \text{Eqn. 4-2}$$

For asymmetrical reflecting planes, the angular separation measured in the rocking curve consists of two components, $\Delta\theta$ and $\Delta\phi$. The difference in Bragg angle $\Delta\theta$ comes from the relative difference in the reflecting plane spacing $\Delta d/d$ between the layer and substrate. The second component $\Delta\phi$ comes from the difference in the inclination to the surface of the corresponding reflecting planes in the layer and in the substrate (Figure 4-5) Therefore the peak separation measured in an asymmetrical reflection rocking curve is not $\Delta\theta$, but rather $\Delta W = \Delta\theta \pm \Delta\phi$. To describe the state of strain of the epitaxial layer, $\Delta\theta$ and $\Delta\phi$ should be obtained separately. For this purpose, ΔW is measured twice from the same asymmetrical reflecting plane but with different geometry, so that $W_1=\theta_B+\phi$ and $W_2=\theta_B-\phi$, resulting in $\Delta\theta=(\Delta W_1+\Delta W_2)/2$ and $\Delta\phi=(\Delta W_1-\Delta W_2)/2$ [101]. These relationships are shown in Figure 4-6.

From Equations 4-1 and 4-2 it is clear that in-plane strain cannot be measured using symmetrical reflections in which ϕ=0. While $\Delta a_{//}/a_o$ is generally small in high quality epitaxy, it does provide information on the degree of relaxation present and on the accuracy of compositional calculations performed using results of symmetrical reflections

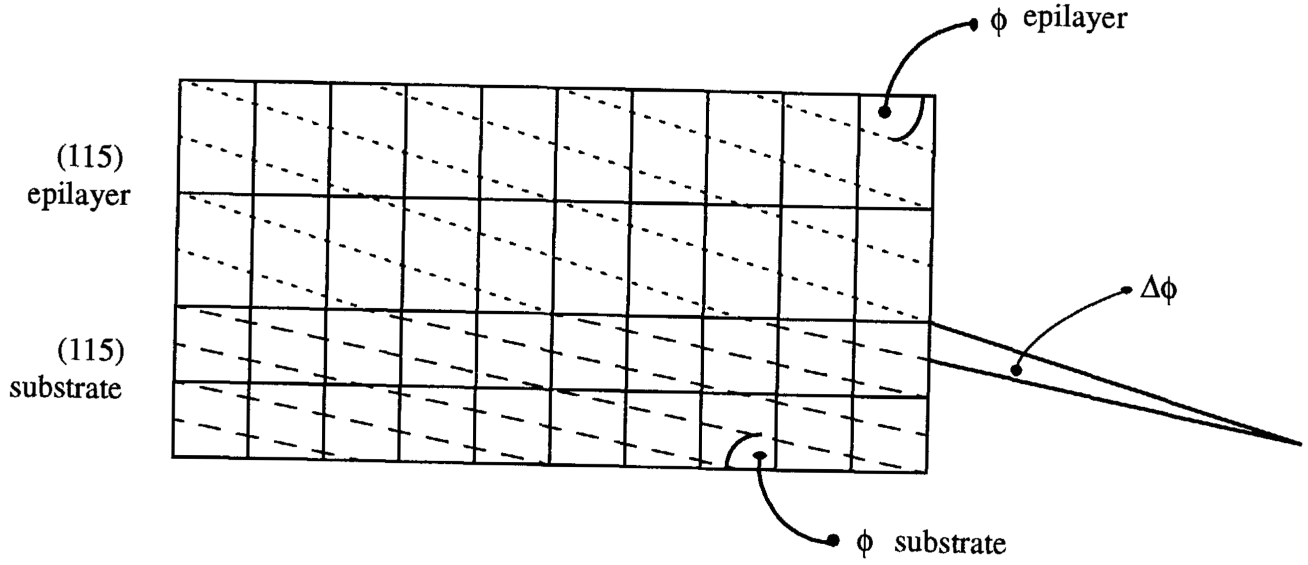

Figure 4-5 Orientation of Asymmetrical Reflection Planes

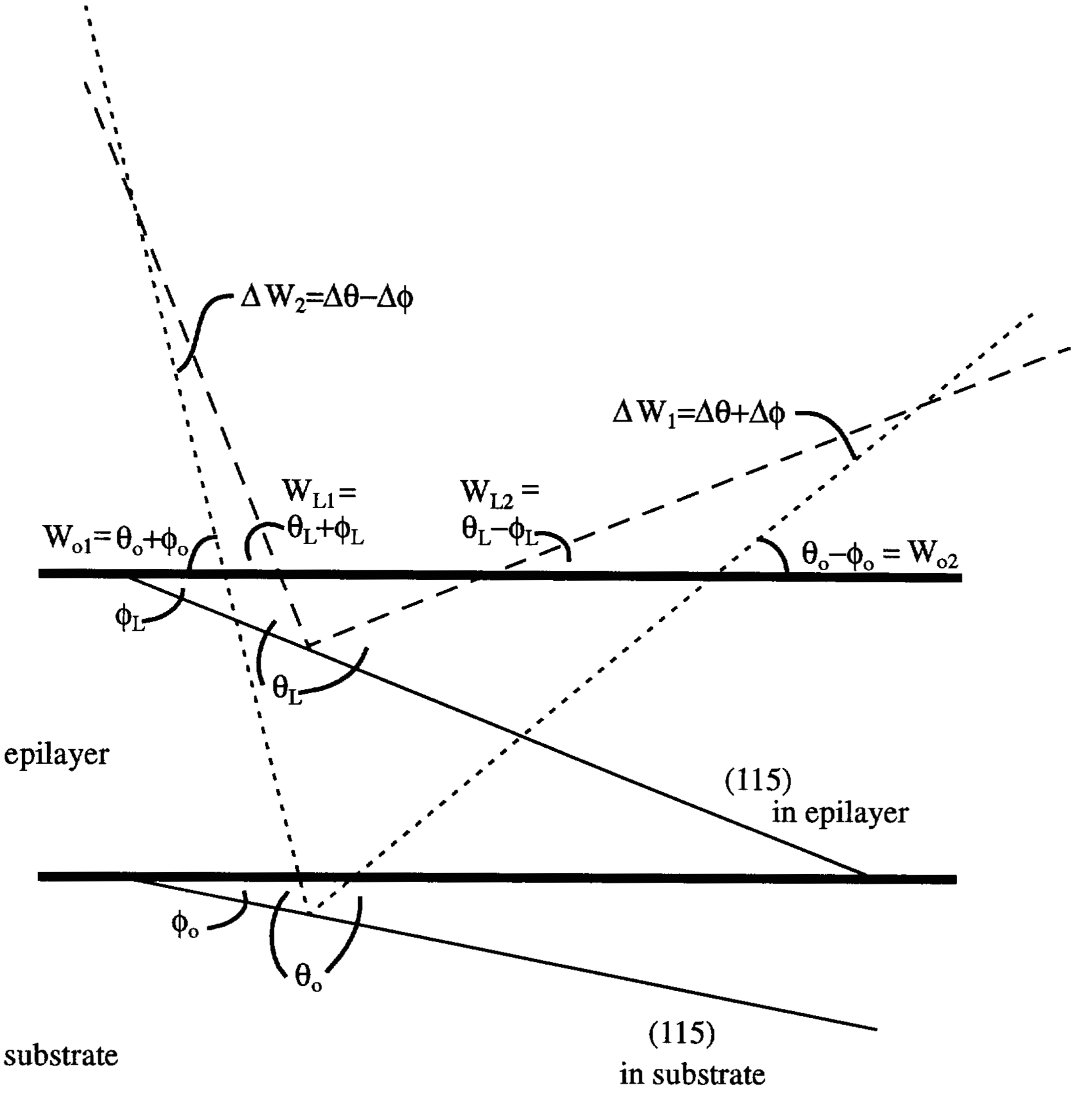

Figure 4-6 Angles Measured in Two Asymmetrical Rocking Curves on a Particular Plane: (115)

[17]. As a figure of merit, $\Delta a_{//}/a_o \leq 10^{-4}$ is considered to be a characteristic of coherent epitaxy [104] and an indication of purely tetragonal distortion in the epilayer and an absence of misfit dislocations at the interface [14, 101]. Thus a minimum of two asymmetrical rocking curves measured for the same plane is required to adequately evaluate the state of strain and degree of relaxation in epitaxial materials.

Rocking curves from symmetrical reflections are generally less dispersive and have stronger diffracted intensities than those from asymmetrical reflections [90, 92]. Symmetrical rocking curves therefore have the advantage of better resolution and are desirable for the improved accuracy of the angular separation measurement. After in-plane strain and degree of relaxation have been determined from the pair of asymmetrical measurements described above, a symmetrical reflection rocking curve is obtained for which the strain as a function of angular separation takes the form $\Delta a_{\perp}/a_o = -(\cot\theta)\Delta\theta$ (Equation 4-1 with $\phi=0$).

In the derivation of this equation it was assumed that the substrate was precisely oriented along a crystallographic direction, usually the (001). Errors may occur in the determination of the perpendicular mismatch if even small substrate miscut angles are not taken into account [105]. Since GaAs and AlGaAs are often grown on substrates intentionally misoriented as much as 4° to improve morphological and optical properties [106], large errors occur unless the misorientation angle is included in the calculation.

It has been shown that the magnitude and direction of the substrate miscut angle, α, can be determined from four symmetrical rocking curve measurements spaced at azimuthal angles of 90° [107]. This information can then be used to modify the strain versus angular separation relation so that it includes the misorientation angle. In this case the perpendicular mismatch relation for any arbitrary azimuthal orientation ψ (defined with respect to the direction of miscut) can be expressed as:

$$\frac{\Delta a_{\perp}}{a_o} = -\left[\frac{\cos\theta\cos\alpha}{\sin(\theta+\alpha\cos\psi)\cos(\alpha\sin\psi)}\right]\cdot\Delta\theta \qquad \text{Eqn. 4-3}$$

When the direction of the miscut angle is known, either from previous measurements on wafers from the same boule or from manufacturer's specifications, two symmetrical rocking curves separated by an azimuthal angle of 180° are sufficient to determine both perpendicular strain and magnitude of miscut if these measurements are taken at azimuthal angles of $\psi=0°$ and $\psi=180°$ relative to the direction of miscut [105]. In this case Equation 4-3 can be written as:

$$\frac{\Delta a_{\perp}}{a_o} = -\cot\theta \cdot \left(\frac{\Delta\theta_{0°} + \Delta\theta_{180°}}{2}\right) \qquad \text{Eqn. 4-4}$$

Magnitude of the miscut angle can be verified from the peak separation measurements taken at $\psi=o°$ and $\psi=180°$ according to the formula:

$$\alpha = arc\tan\left(\frac{\Delta\theta_{0°} - \Delta\theta_{180°}}{\Delta\theta_{0°} + \Delta\theta_{180°}} \cdot \tan\theta\right) \qquad \text{Eqn. 4-5}$$

It is obviously important to know the substrate miscut direction in order to position the sample for the rocking curve measurement so the miscut direction is co-planar with the x-ray beam. For wafers of unknown miscut direction, a minimum of four symmetrical measurements is required to make an accurate determination of perpendicular strain. For wafers of known or specified miscut magnitude and direction, only two symmetrical measurements are needed to accurately determine the perpendicular strain and simultaneously confirm the misorientation magnitude.

It should be noted that Equations 4-3, 4-4, and 4-5 were derived for *small* angular deviations from symmetrical reflections. They are not applicable to asymmetrical reflection geometry. Substrate misorientation with respect to a symmetrical reflection plane is included in the measurement of $\Delta\phi$ (the inclination of of the asymmetrical reflecting plane from a perfectly aligned crystallographic surface plane), so that miscut cannot be resolved using asymmetrical reflections.

A minimum of four rocking curve measurements, two asymmetrical and two symmetrical, are required to evaluate in-plane strain, degree of relaxation, substrate misorientation magnitude, and perpendicular strain in epilayers grown on substrates of known miscut direction. These parameters are important for the accurate evaluation of the epilayer composition and thickness. In-plane strain and degree of relaxation provide a means of assessing the coherency of the epitaxial process, and the magnitude of the in-plane strain determines the accuracy of composition calculations performed using perpendicular strain only. Substrate miscut must be included in calculations of perpendicular strain from symmetrical reflection rocking curves to avoid significant error. The accuracy of the measurement of perpendicular strain will determine the accuracy of the composition and thickness calculations.

4.1.3 Calculating Composition from Strain

Aluminum mole fraction in $Al_xGa_{1-x}As$ can be determined from the relaxed lattice constant of the material. The relaxed lattice mismatch of epilayer to substrate, $(\Delta a/a_o)_r$, can be calculated from the perpendicular strain, $\Delta a_\perp/a_o$, when the in-plane strain meets the criterion for coherent epitaxy. The amount of perpendicular strain present for a given composition is a function of the elastic constants of the compound in the directions of strain. For epitaxial material grown coherently on (001) oriented substrates in the III-V system, the relevant components of strain are the elastic constants C_{11} and C_{12}. These materials constants are related to the magnitude of strain through the Poisson's ratio, which is defined as $\nu = C_{12}/(C_{11}+C_{12})$. For material in which the in-plane strain is small enough to meet the criterion for coherent epitaxy, the relaxed mismatch $(\Delta a/a_o)_r$ is calculated from the perpendicular strain according to [101]:

$$\left(\frac{\Delta a}{a_o}\right)_r = \left(\frac{1-\nu}{1+\nu}\right)\cdot\left(\frac{\Delta a_\perp}{a_o}\right) \qquad \text{Eqn. 4-6}$$

Poisson's ratio for $Al_xGA_{1-x}As$ is assumed to follow Vegard's Law and vary linearly with composition between the endpoints ν_{GaAs} and ν_{AlAs}. The elastic constants of

GaAs have been determined experimentally and ν_{GaAs}=0.311. The hygroscopic nature of AlAs has hindered the accurate determination of elastic constants for this material. Sound velocity experiments indicate that C_{11}(AlAs) is approximately 15×10^{11} dyn/cm^2, compared to C_{11}(GaAs)=12.1×10^{11} dyn/cm^2 [104]. There is consequently some uncertainty in the endpoint ν_{AlAs}.

Some calculations of composition in this system use the elastic constants of the substrate as approximations for the layer constants [15, 100-101], leading to an over-estimate of aluminum mole fraction [104]. In more accurate approximations the Poisson's ratio of $Al_xGa_{1-x}As$ is expressed as (ν_{GaAs}- x$\Delta\nu$), where x is the Al mole fraction and $\Delta\nu$=(ν_{GaAs}− ν_{AlAs}). $\Delta\nu$ can then be treated as an unknown parameter and determined from a quadratic fit to data [7]. This results in an expression for the relaxed mismatch as a function of perpendicular strain and composition.

$$\left(\frac{\Delta a}{a_o}\right)_r = \left(\frac{1-\nu_{GaAs}}{1+\nu_{GaAs}}\right)\cdot\left(\frac{1}{1-\left(\frac{2\Delta\nu x}{1-(\nu_{GaAs})^2}\right)}\right)\cdot\left(\frac{\Delta a_\perp}{a_o}\right) \qquad \text{Eqn. 4-7}$$

The relaxed mismatch is additionally related to the aluminum mole fraction by the standard assumption of Vegard's Law; that is, the relaxed mismatch varies linearly with composition from $(\Delta a/a_o)_r$=0 at x=0 in binary GaAs to $(\Delta a/a_o)_r$=(a_{AlAs}-a_{GaAs})/a_o at x=1 in binary AlAs. The comparison standard is defined as a_o=a_{GaAs}. The lattice constant of GaAs is well known; the value a_o=5.65325Å used in this work [9] is in the range of other published values [92, 100-101]. The relaxed lattice constant for binary AlAs is less well known because the material is extremely hygroscopic; reported AlAs lattice constants range from 5.660Å to 5.670Å [104].

This uncertainty in the relaxed AlAs lattice constant has been addressed by using internal AlAs calibration standards [17] and by performing empirical fits to data [7, 104] to determine the AlAs endpoint for $(\Delta a/a_o)_r$. The use of internal AlAs calibration standards requires the growth of layers of AlAs thick enough to produce a measurable diffracted x-ray signal [5]. Single AlAs layers producing measurable signal are over the pseudomorphic limit for AlAs on GaAs (≥3 μm) and are relaxed to some degree. Internal AlAs calibration standards are therefore not appropriate for determining the AlAs endpoint of $(\Delta a/a_o)_r$ for structures in which the layers are below the pseudomorphic thickness limit, as is the case in superlattices and quantum wells. Consequently, this work follows the approach of Tanner et al. [7] which deduces the lattice parameter mismatch between GaAs and AlAs from a quadratic fit to the data. This is accomplished by setting the Vegard's Law relation for relaxed mismatch as a linear function of composition between the endpoints of lattice mismatch, $(\Delta a/a_o)_r = x(a_{AlAs} - a_{GaAs})/a_o = x(\Delta a_{AlAs}/a_o)$, equal to Equation 4-7. The resulting expression is:

$$\left(\frac{\Delta a_{\perp}}{a_o}\right) = \left(\frac{1+\nu_{GaAs}}{1-\nu_{GaAs}}\right) \cdot \left(\frac{\Delta a_{AlAs}}{a_o}\right) \cdot \left[x - \left(\frac{2\Delta\nu}{1-\nu_{GaAs}^2}\right)x^2\right] \qquad \text{Eqn. 4-8}$$

Equation 4-8 guarantees that the relationship between $(\Delta a_{\perp}/a_0)$ and composition for ternary III-V compounds will be non-linear if the Poisson ratios of the binary compounds are different [104]. Therefore the parameter fit described above is necessary to avoid over-estimation of aluminum mole fraction.

The unknown parameters in this relation, $\Delta a_{AlAs}/a_o$ and $\Delta\nu$, were determined empirically from the best quadratic fit to the data to be 1620 ppm and 0.041 respectively, in good agreement with published values [7]. These values led to a determination of lattice constant and Poisson's ratio for AlAs of a_{AlAs}=5.6624Å and ν_{AlAs}=0.27. This fit resulted in an explicit expression for Al mole fraction as a function of $\Delta a_{\perp}/a_o$. The parameter κ in this expression is equal to the first two RHS factors in Equation 4-8.

$$x = \frac{\left(\frac{1-\nu_{GaAs}^2}{2\Delta\nu}\right) - \sqrt{\left(\frac{1-\nu_{GaAs}^2}{2\Delta\nu}\right)^2 - \left(\frac{4}{\kappa}\right)\left(\frac{1-\nu_{GaAs}^2}{2\Delta\nu}\right)\left(\frac{\Delta a_{\perp}}{a_0}\right)}}{2} \qquad \text{Eqn. 4-9}$$

4.1.4 Thickness Measurements

Two coherent epitaxial layers of identical composition will by definition diffract at the same angle. However, if two layers of identical composition are separated by a third layer of a different composition, the diffracted beams from the identical layers will travel different distances from diffraction site to detector due to the intervening material (see Figure 4-7), producing a path length difference which is proportional to the thickness of the sandwiched material. This difference in path length produces a phase difference between the diffraction peaks of the two identical layers. The layers both produce diffraction maxima at the Bragg angle for the given material and reflection geometry; however, the sum of the two out-of-phase x-ray beams results in a short-period beating of the summed signal, known as Pendellösung fringes [92, 109]. The angular period of these fringes provides information on the path length difference, and consequently the thickness of the intervening layer can be determined. For symmetrical reflections this relation takes the form:

$$\Delta\omega_{PF} = \frac{\lambda \cdot \cos\alpha}{2t \cdot \cos\theta_B} \qquad \text{Eqn. 4-10}$$

where λ is the x-ray wavelength, t is the thickness of the intervening layer, α is the substrate misorientation angle, and $\Delta\omega_{PF}$ is the angular separation between fringes [105].

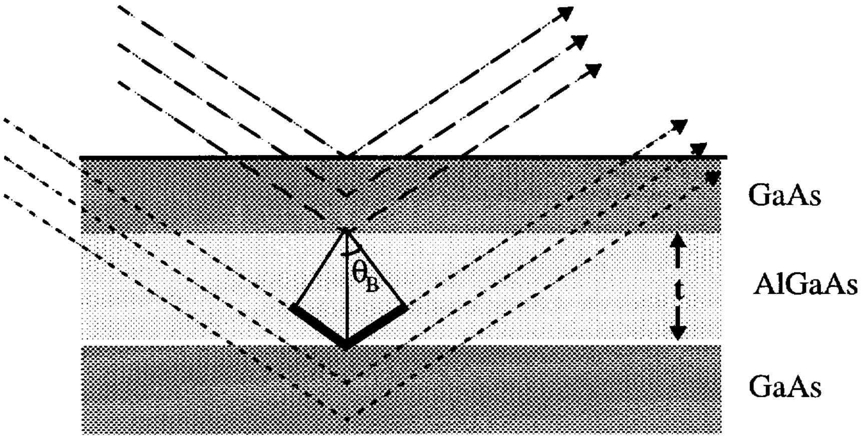

Figure 4-7 Path Length Difference Resulting in Pendellösung Fringes

Any discontinuity in boundary conditions for diffraction at the same Bragg angle will produce Pendellösung fringes. These fringes are visible in the rocking curve only when the two layers diffracting at the same angle produce signals of approximately equal amplitude. Since the magnitude of the diffracted signal is directly proportional to the thickness of the diffracting layer and inversely proportional to the depth below the surface at which the diffraction event takes place, the thickness-to-depth ratio of the two cladding layers must be of the same order of magnitude for the Pendellösung fringes to be apparent. Fringes may also be obscured when the separation is so small that the period of the fringes is large and therefore far from the maximum (as in a narrow quantum well), or when the separation is so large that the period of the fringes is too small to resolve (as in layers more than 5μm thick). Sandwiched layers from 50Å to 5μm can be measured using this technique [92, 102]. Fourier transform spectra of the rocking curves have been shown to be useful in extracting thicknesses in the 3 to 5μm range [109-110].

4.1.5 Interference Effects in Superlattices

An additional periodicity is imposed on the Bragg condition for in-phase diffraction in structures where there are many epitaxial layers with alternating compositions. In this situation the rocking curve shows multiple maxima which are the result of interference of x-rays diffracted from the various epilayers. For these multilayer structures there is no longer a one-to-one correlation of rocking curve maxima to individual epilayers [102, 111]. Figure 4-8 illustrates the change in the rocking curve as the number of layers is increased from three to eleven. The inset plots on the left show material composition versus depth. When large numbers of layers are present only one strong superlattice peak is observed, as in Figure 4-8d. The angular position of this peak corresponds to the mean mismatch of the entire stack of thin layers [4].

The long period interference fringes evident in the rocking curves of multilayer structures (as in Figure 4-8d) are referred to as superlattice satellite peaks. They provide

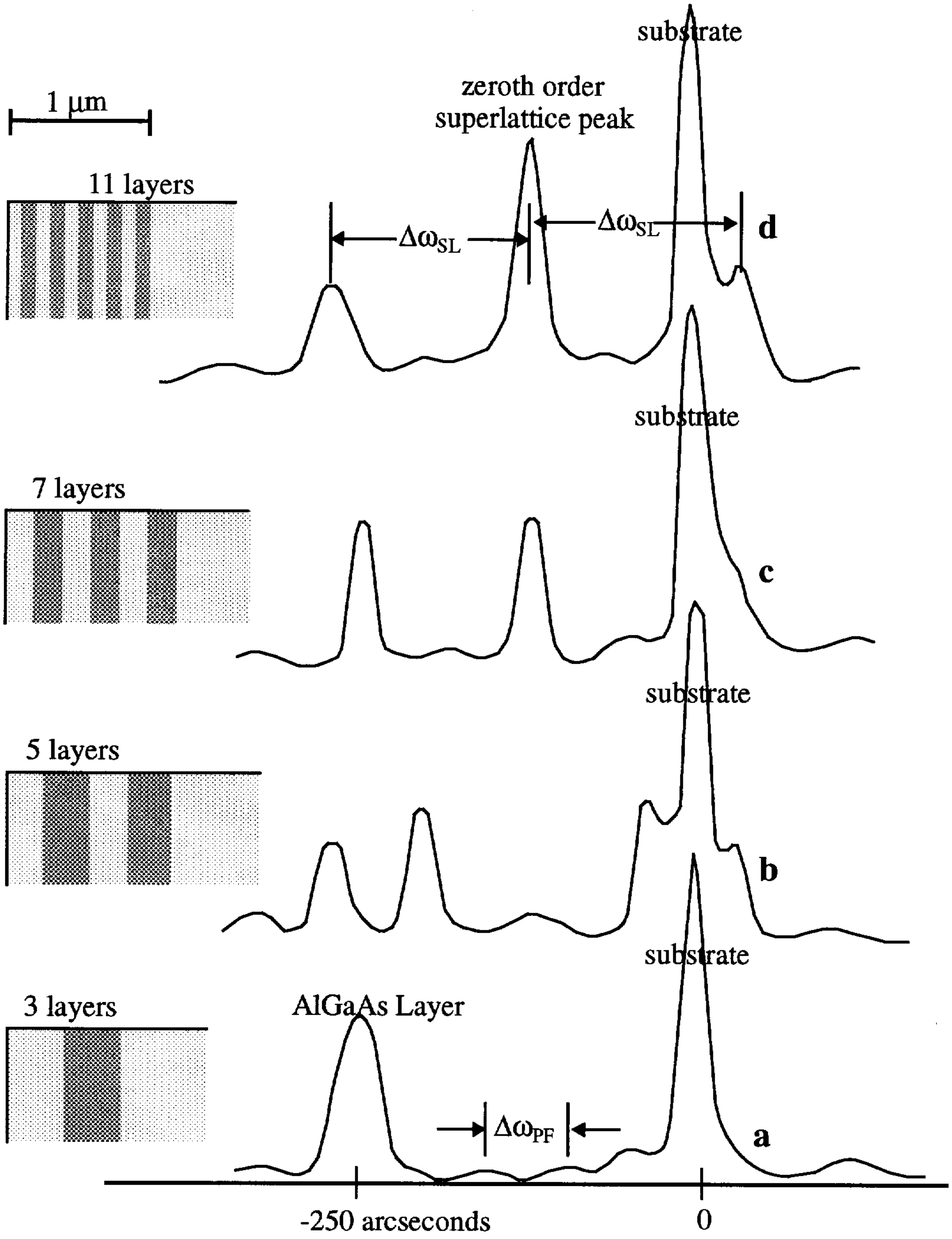

Figure 4-8 Interference Effects in Multilayer Structures

an accurate method of determining the thickness of an individual superlattice period [102, 110, 112]. For symmetrical reflections, this relation is:

$$p = \frac{\lambda \cdot \cos\alpha}{2 \cdot \Delta\omega_{SL} \cdot \cos\theta_B} \qquad \text{Eqn. 4-11}$$

where p is the period of the superlattice, λ is the x-ray wavelength, α is the substrate misorientation angle, and $\Delta\omega_{SL}$ is the angular separation between the superlattice maxima. The thickness of the entire superlattice stack can be determined by the short period Pendellösung fringes according to the relation given in Equation 4-10 [92, 112]. Consequently, rocking curves on superlattices can measure mean composition $\bar{x}$ from the main peak separation $\Delta\theta$ (Equation 4-9), superlattice stack thickness from the Pendellösung fringe separation $\Delta\omega_{PF}$ (Equation 4-10), and superlattice layer period from the superlattice satellite separation $\Delta\omega_{SL}$ (Equation 4-11). The relevant measurements are defined graphically in Figure 4-9.

Rocking curve sensitivity to interface compositional gradients is enhanced in SL structures since many interfaces contribute to the diffraction profile [102]. Abruptness of SL interfaces can be evaluated qualitatively from the rocking curves. The qualitative approach to the interpretation of rocking curves provides information on interface grading [4, 14, 113], interface coherence [94-96], and thickness uniformity [94, 114] of the SL layers. This approach was used in the current investigation, and the magnitude and spatial extent of compositional gradients at interfaces were inferred from the qualitative analysis of the data (see section 4.4.2).

For quantitative evaluation of diffraction profiles, however, it is necessary to use kinematic or dynamic simulations of the diffraction behavior of the structure [90-94]. Conditions under which the kinematic or dynamic theory is appropriate have been discussed in detail in the literature [115-118]. The variables in these simulations are layer thickness, layer composition, and interface abruptness. These variables are adjusted in the simulation until a best fit to the experimental rocking curve is obtained. The best fit thick-

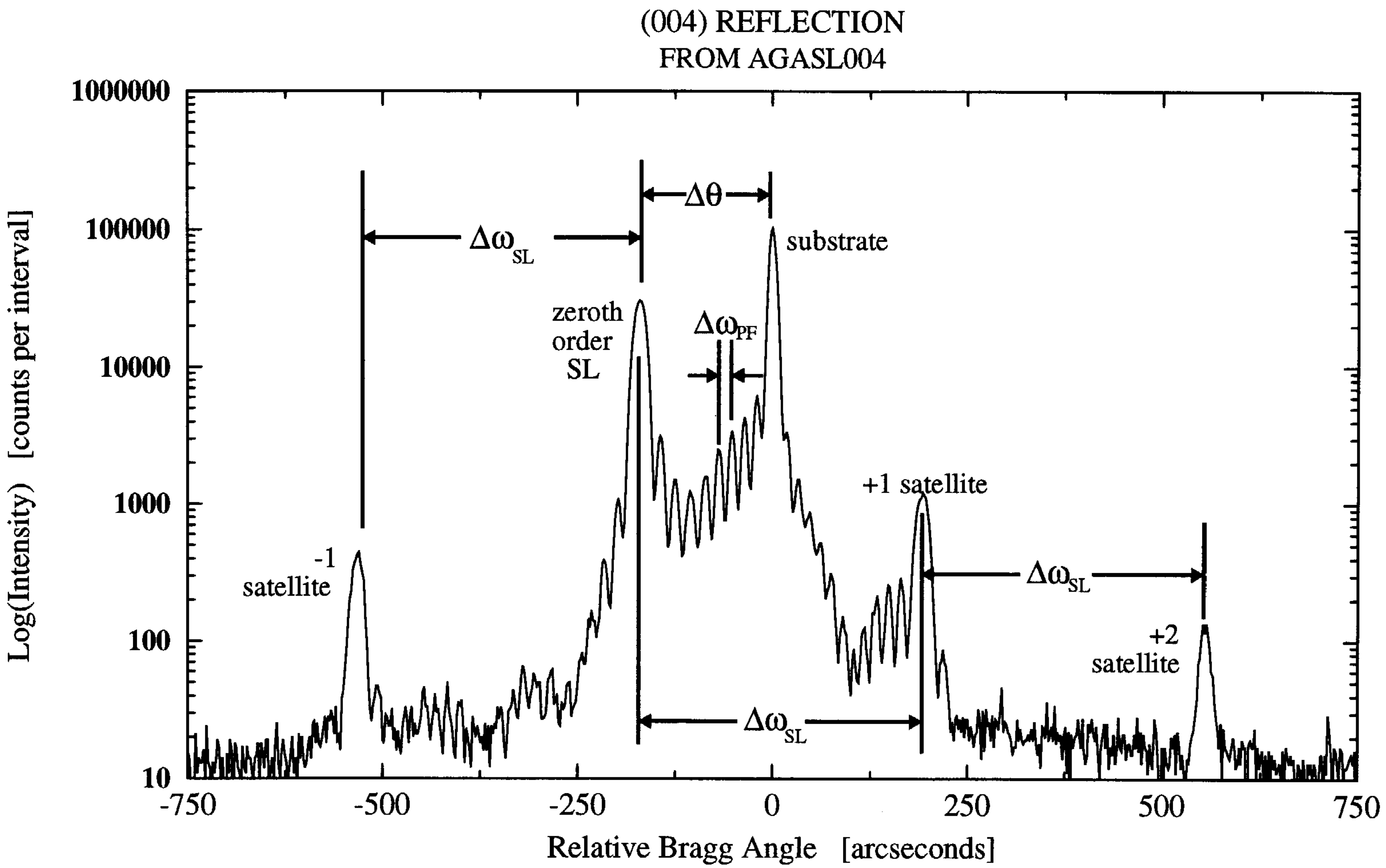

Figure 4-9 Definition of Angular Separations

ness, composition, and abruptness are considered to be unique quantitative descriptions of the structure. The magnitude and extent of compositional gradients at the heterointerfaces can be determined directly by this method.

4.2 The X-Ray Rocking Curve System

Rocking curve measurements were performed on a Siemens DACO-MP computer-controlled diffractometer with a four-crystal monochromator, shown schematically in Figure 4-10. The Siemens AEG FK 1.5 kW x-ray tube produces CuKα_1 and CuKα_2 radiation. The x-ray beam is introduced into the four-crystal monochromator through a 3 x 3 mm slit in order to maximize beam intensity at the specimen. The monochromator consists of two u-shaped blocks of silicon crystal cut parallel to the (220) reflecting planes. This monochromator arrangement produces a highly collimated monochromatic CuKα_1 beam (λ=1.541Å) of perpendicular (π) polarization only [90]. The four-crystal arrangement overcomes the limitations of the standard double-crystal diffractometer and provides the resolution necessary (2 arcseconds) to resolve higher order superlattice peaks [119]. The intensity of the x-ray beam is considerably decreased in the monochromator due to the four reflection geometry. This is compensated for by operating the x-ray source at maximum power, setting wide entry slits, and scanning with the detector open (rather than using an entry slit) for longer step intervals.

The collimated CuKα_1 beam exits the monochromator through a 0.5 x 1.5 mm slit to minimize variation in the angle of incidence at the specimen without increasing beam divergence. The beam size at the sample is approximately 1mm^2 for symmetrical reflections. The goniometer is rotated by a stepper motor under the control of the DACO-MP system. The NaI scintillation counter is fixed at the $2\theta_B$ position. The fixed detector limits the range around the Bragg angle which can be accurately scanned.

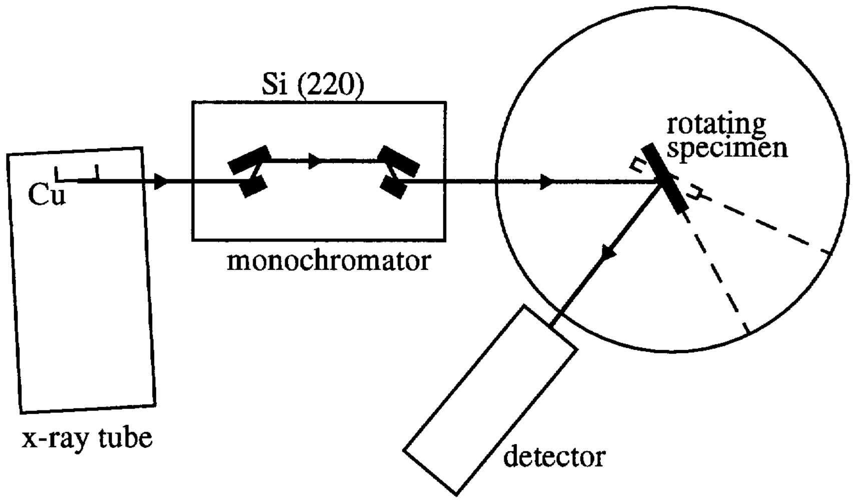

Figure 4-10 The X-Ray Diffractometer with 4-Crystal Monochromator

4.3 Collecting Double Crystal Rocking Curve Data

In order to evaluate GaAs/$Al_xGa_{1-x}As$ superlattices, it is necessary to determine the in-plane strain $\Delta a_{//}/a_o$ from asymmetrical rocking curves, the substrate misorientation angle α from symmetrical rocking curves, and the perpendicular strain $\Delta a_{\perp}/a_o$ from the most accurate possible measurement of $\Delta\theta$. In addition, accurate measurements of $\Delta\omega_{SL}$ and $\Delta\omega_{PF}$ are required to determine the SL period and the thickness of the entire stack. The process of collecting this information includes choosing appropriate crystal reflections, careful evaluation of the substrate, and optimization of the system parameters (scan range, step interval, and step duration) to obtain clear data on Pendellösung fringes and higher order satellite peaks.

4.3.1 Choosing Appropriate Reflections

The intensity, degree of dispersion, and sensitivity to changes in composition in rocking curve measurements are independent functions of the angle of x-ray incidence [91-92, 120-121]. Consequently different reflection geometries result in different combinations of signal magnitude, accuracy, and sensitivity. These rocking curve characteristics are all related to the angle of incidence θ_i through the so-called structure factor of the material. In order to choose reflection geometries which are most appropriate for the variables being measured, it is necessary to consider the structure factor for a particular material and reflection geometry in some detail.

Calculation of the structure factor is based on the atomic scattering factor, which is the ratio of the radiation amplitude scattered by the charge distribution in a particular atom to that scattered by a point electron [122]. Atomic scattering factors are tabulated for elements and their isotopes as a function of $(\sin\theta_i)/\lambda$, so that intensities can be calculated for various x-ray wavelengths and diffraction directions [123]. The structure factor for a given reflection is the sum of the atomic scattering factors of the elements in the unit cell convolved with the geometric structure factor for that reflection [122]. For binary zincblende crystals, this relation takes the form:

$$F = 4\left[f_1 + f_2 e^{(\pi i/2)\,(h+k+l)}\right] \qquad \text{Eqn. 4-12}$$

In this equation f_1 and f_2 represent the atomic scattering factors (calculated from tabulated values for the appropriate angle of incidence) of the cation and anion, respectively, of the compound, and the Miller indices (hkl) define the reflecting plane. The scattering factors for ternary compounds are calculated assuming a linear relationship between atomic scattering magnitude and composition [4]; thus for $Al_xGa_{1-x}As$, $f_1 = xf_{Al} + (1-x)f_{Ga}$.

The structure factor describes the interference conditions within each unit cell of a specified material for a particular diffraction direction, and these interference conditions determine the intensity of the diffracted x-ray beam. The intensity is directly proportional to the squared magnitude of the structure factor, which in the case of zincblende materials results in the following cases [97]:

$$|F|^2 = 16\left(f_1^2 + f_2^2\right) \qquad \text{when (h+k+l) is odd} \qquad \text{Eqn. 4-13}$$

$$|F|^2 = 16\,(f_1 + f_2)^2 \qquad \text{when (h+k+l)=(2n)2; n=any integer} \qquad \text{Eqn. 4-14}$$

$$|F|^2 = 16\,(f_1 - f_2)^2 \qquad \text{when (h+k+l)=(2n+1)2; n=any integer} \qquad \text{Eqn. 4-15}$$

The first case, (h+k+l) odd, holds for all asymmetrical rocking curve geometries which are physically realizable on the diffractometer used in this work. This is due to the fact that the detector fixed at $2\theta_B$ prevents the use of those asymmetric reflections for which $\theta_B<\phi$. The remaining asymmetric reflection geometries with sufficiently large structure factors are (113) and (115). The geometry of (113) requires near grazing angle of incidence ($\theta_i<2°$), which greatly reduces the power per unit area incident on the sample, and the resulting diffracted intensity is reduced below measurable levels unless the x-ray source uses a rotating anode and can be operated at higher power [124]. As the x-ray source in this system is already being operated at maximum power, the (113) reflection cannot be obtained. The asymmetric rocking curve measurements for determining in-plane strain and evaluating the coherence of the epitaxy were therefore performed in (115) geometry. The GaAs to $Al_{0.8}Ga_{0.2}As$ signal ratio, $|F_{GaAs}|^2 : |F_{AlGaAs}|^2$, is 3:2, resulting in greater sensitivity to GaAs than AlGaAs in this reflection.

The case of Equation 4-14, where (h+k+l) is an even multiple of two, produces the maximum diffracted intensity from zincblende lattices. Symmetrical reflections for which this case holds show minimum dispersion and maximum sensitivity in $\Delta\theta$ to changes in relative lattice constant [125]. In particular, the (004) reflection has strong diffracted intensity and suitable geometry for the diffractometer. This reflection has the additional advantage that Pendellösung fringes down to 10 arcseconds in separation can be easily resolved [90]. The (004) reflection was used to obtain rocking curve measurements with maximum accuracy in $\Delta\theta$ and $\Delta\omega_{PF}$. Substrate evaluation to determine miscut angle α was also performed using this reflection. The GaAs to $Al_{0.8}Ga_{0.2}As$ signal ratio for this reflection is 5:3. This results in a poor signal to noise ratio for the interference effects caused by AlGaAs barriers in the superlattice. The main superlattice peak can be easily identified, but higher order satellite peaks are weak and difficult to distinguish from background noise.

It is clear from Equation 4-15 that when the sum of the Miller indices of a reflection is an odd multiple of two, the diffracted intensity is decreased. Reflections for which this case applies are termed "quasi-forbidden" reflections. Quasi-forbidden reflections from binary GaAs, in which the atomic scattering factors of Ga and As are close in magnitude, produce weak diffracted intensity as $|f_{Ga}-f_{As}|$ approaches zero. However, there is an appreciable difference in the magnitudes of the atomic scattering factors f_{Al} and f_{As} in ternary $Al_xGa_{1-x}As$, especially when $x>0.5$, which results in a relatively strong diffracted signal from the quasi-forbidden reflection in AlGaAs. A quasi-forbidden reflection therefore has increased sensitivity to aluminum content [126]. The GaAs to $Al_{0.8}Ga_{0.2}As$ signal ratio for the (002) reflection is 1:110. Because the GaAs signal is comparatively weak, the interference effects due to the AlGaAs barrier layers in the superlattice show an improved signal to noise ratio and higher order satellite peaks are easily distinguishable from background noise. In addition the (002) reflection is more sensitive to thin epitaxial layers, since the Bragg angle for this reflection (15.8°) is such that there is less diffraction from the GaAs substrate in the measured signal [92]. Because of this increased sensitivity to SL interference effects, rocking curves from (002) reflections were chosen for the evaluation of superlattice quality.

4.3.2 Substrate Evaluation

All superlattice samples were grown on Sumitomo prime semi-insulating (100) GaAs substrates sequentially cut from the same boule. These wafers were certified by the manufacturer to be 2°±0.5° off (100) toward the nearest <110>. In order to confirm this intentional misorientation and determine the direction of the miscut, a series of rocking curves was obtained from the (004) geometry with the wafer rotated about the surface normal. In this rotation $\Psi=0°$ was defined as the orientation in which the major flat was horizontal at the top of the wafer and the minor flat was vertical to the left. Positive rotation was defined as clockwise, as illustrated in Figure 4-11. Figure 4-12 shows that the peak separation $\Delta\theta$ between the substrate and main superlattice peak was indeed strongly affected when the azimuthal angle was changed, even in the case of the symmetric (004) reflection.

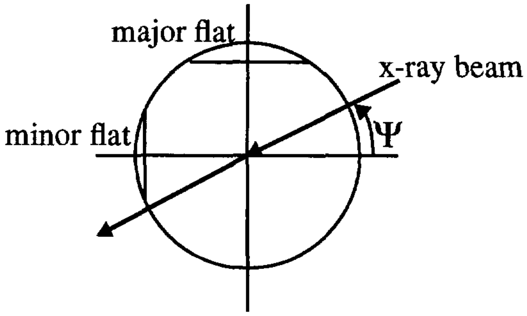

Figure 4-11 Orientation of GaAs Substrate

When the x-ray beam is co-planar with the direction of substrate miscut, maximum tilt of the substrate away from the (001) surface is seen by the x-ray [105]. Rocking curves obtained 180° apart along this direction will show maximum difference in peak separation, thus determining the direction of tilt [106, 107]. When this direction of misorientation is known, only two rocking curves 180° apart in azimuthal rotation are required to determine the magnitude of the tilt. Figure 4-12(a) shows that the azimuthal

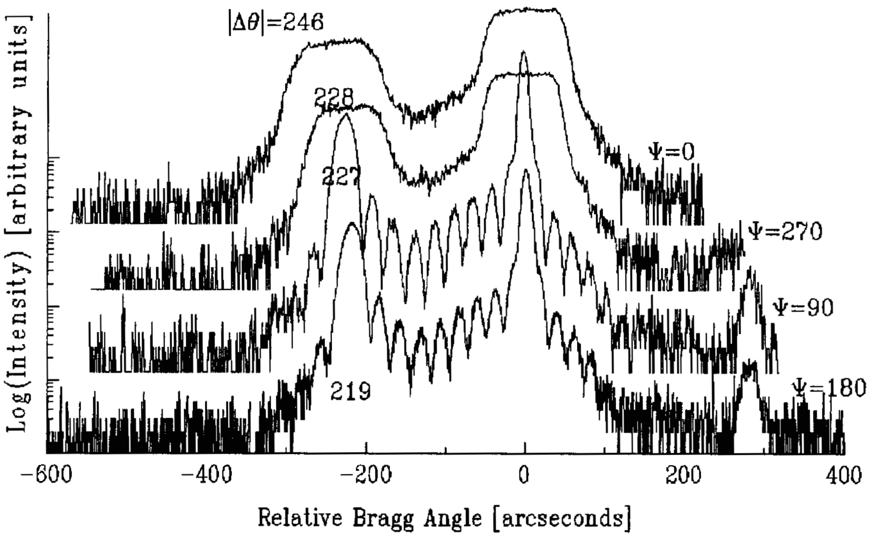

(a) Peak Separation at Ψ=0, 90, 180, and 270°

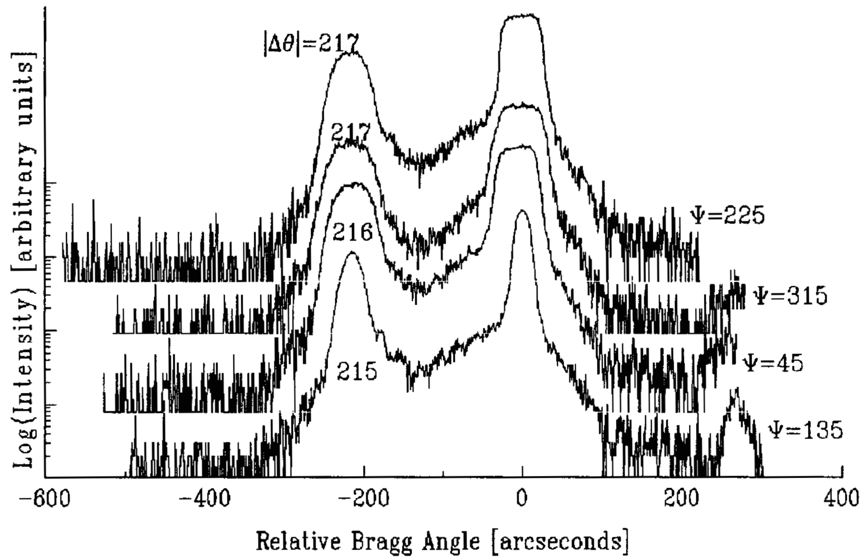

(b) Peak Separation at Ψ=45, 135, 225, and 315°

Figure 4-12 Determination of Substrate Misorientation from Symmetric (004) Reflection

angles defined as Ψ=0° and Ψ=180° produced the maximum difference in $\Delta\theta$, thus determining that the direction of miscut is parallel to the major flat. Figure 4-12(b) confirms that the direction of miscut is along the Ψ=0–180° axis.

Dispersion of the signal is a function of the ratio of the direction cosine (with respect to the sample surface) of the diffracted beam to that of the incident beam [120, 121]. In the case of substrate miscut and symmetrical geometry, this ratio takes the form $\sin(\theta_B + \alpha)/\sin(\theta_B - \alpha)$ for Ψ=0° and the inverse for Ψ=180°. Thus the sense of the miscut can be determined from a comparison of the full width half maxima of the two measurements taken at 0° and 180°. From the data presented in Figure 4-12 it is clear that this ratio is greater in the Ψ=0° rotation and that the tilt in therefore down toward the minor flat. This completes the determination of the direction and sense of the miscut with respect to the major and minor flat locators on the wafer. These relations are illustrated in Figure 4-13.

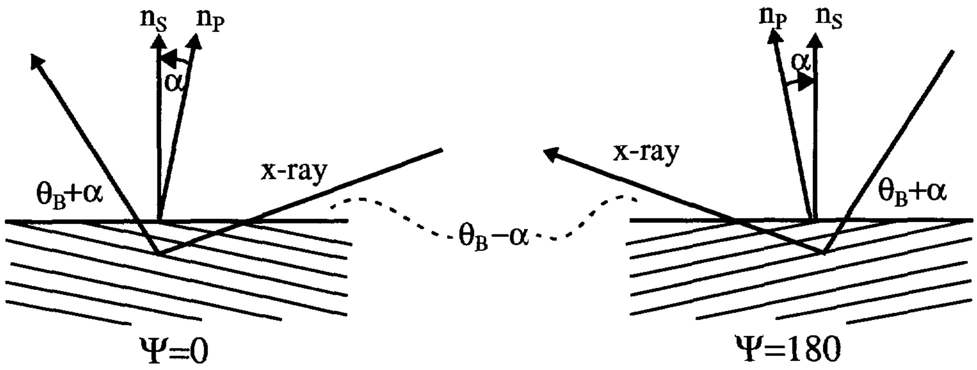

Figure 4-13 Direction and Sense of Substrate Miscut

The manufacturer's specification of a 2° miscut was confirmed using the Ψ=0° and Ψ=180° measurements according to the relation in Equation 4-5 [105], which resulted in a measured substrate misorientation of α=2.17°. Once the misorientation magnitude, direction, and sense were known, subsequent measurements were obtained with the wafers positioned so that the x-ray beam was co-planar with the direction of tilt in the $\Psi=0$ °and $\Psi=180°$ orientations. In this case Equation 4-3 can be simplified to:

$$\frac{\Delta a_{\perp}}{a_o} = -\left[\frac{\cos\theta_B \cdot \cos\alpha}{\sin(\theta_B \pm \alpha)}\right] \cdot \Delta\theta \qquad \text{Eqn. 4-16}$$

The positive sense of α applies for $\Psi=0°$; the negative sense applies for $\Psi=180°$.

A comparison of perpendicular strain calculated using Equation 4-16 (requiring only one rocking curve) to that calculated using Equation 4-4 (requiring two rocking curves) indicated that Equation 4-16 produced accurate results from a single rocking curve when the tilt magnitude, direction, and sense were known. Therefore only one symmetrical rocking is required for the accurate evaluation of superlattice structures when the substrate is completely charaterized [127, 128]. Since the $\Psi=180°$ arrangement produces the least dispersive diffracted beam, this configuration was used to obtain the remaining symmetrical rocking curves.

4.3.3 Obtaining Rocking Curves on Superlattices

Once the substrates had been evaluated, four additional rocking curve measurements were obtained on each specimen: Two (115) reflections to determine in-plane strain, one (004) reflection for accurate determination of $\Delta\theta$ and $\Delta\omega_{PF}$, and one (002) reflection to determine $\Delta\omega_{SL}$ and provide as many higher order satellite peaks as possible for qualitative evaluation.

The two asymmetrical (115) rocking curves were obtained, one at $\Psi=0°$ in low angle of incidence geometry and the other at $\Psi=180°$ in high angle of incidence geometry (see Figure 4-6) in order to evaluate the same set of (115) planes in each measurement [101]. Superlattice satellite peaks and Pendellösung fringes are generally irregular in this reflection, so only the separation between the substrate peak and the main superlattice peak was of interest in this measurement. Therefore the rocking curve scan range was limited to 750 arcseconds around the substrate peak. The measurement interval was 5 seconds and the step per measurement was 2 arcseconds.

A typical pair of (115) rocking curves is shown in Figure 4-14. The measurements of $\Delta W_{1,2}$ and calculations of $\Delta\theta$, $\Delta\phi$, $\Delta a_{//}/a_o$, and $\Delta a_{\perp}/a_o$ from the (115) reflections for all specimens are tabulated in Table 4-1 and discussed in further detail in Section 4.4.1.

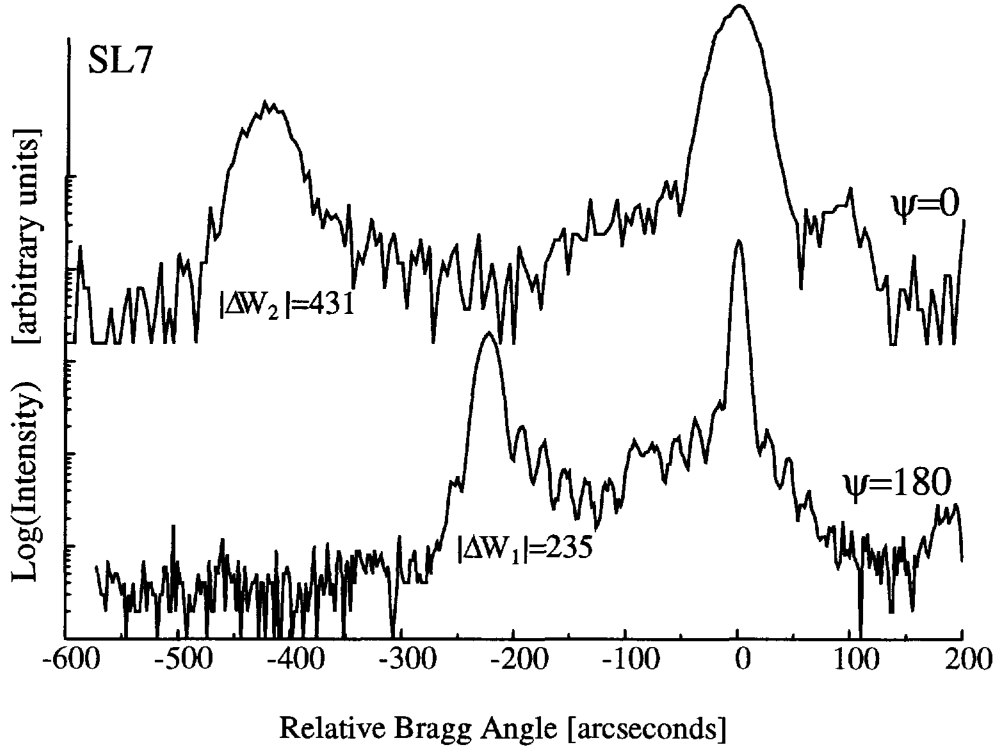

Figure 4-14 Asymmetrical Reflection Pairs

A single rocking curve from the (004) planes was obtained in Ψ=180° configuration for each specimen. This reflection has the greatest sensitivity to changes in composition and the highest resolution for Pendellösung fringes of the geometries achievable on the available diffractometer (see Section 4.3.1). Higher order satellite peaks may also be visible in this reflection, although they will be several orders of magnitude weaker than the substrate peak. Therefore the rocking curve scan range was extended to 2400 arcseconds around the substrate peak. The measurement interval was 10 seconds and the step per measurement was 2 arcseconds. Rocking curves from the (004) reflection on four SL specimens grown at different rates and/or growth interrupted at interfaces are shown in Figure 4-15. Superlattice peaks up to second order are resolvable in these rocking curves. Measurements of $\Delta\theta$ and $\Delta\omega_{PF}$ and calculations of $\Delta a_{\perp}/a_o$ are listed in Table 4-2 in Section 4.4.1, where they are discussed in detail.

A rocking curve from the (002) planes in Ψ=180° configuration was obtained for each specimen. In this reflection geometry the Pendellösung fringes are more difficult to resolve, but higher order SL peaks are visible due to the greatly decreased intensity of the GaAs peak relative to the SL stack. The scan range was 2400 arcseconds around the substrate peak, the measurement interval was 10 seconds, and the step per measurement was 2 arcseconds. Rocking curves from the (002) reflection on the four SL specimens are shown in Figure 4-16. Measurements of $\Delta\omega_{SL}$ and calculations of the SL period are tabulated and discussed in Section 4.4.1.

Symmetrical (004) and (002) reflections were also taken on the three quantum well stacks designed for photoluminescence measurements. In these structures there is no regular periodicity to produce superlattice peaks. The maximum well thickness is 100Å, so that the Pendellösung fringes from these wells are far from the Bragg angle (as indicated in Equation 4-10; this limitation is discussed in Section 4.1.4). The interference fringes which were seen in the quantum well stacks corresponded to the thickness of the entire stack. Individual wells could not be resolved. The rocking curve from the (004) reflection of QW1 is shown in Figure 4-17. The other quantum wells produced similar rocking curves with no measurable difference in peak separation.

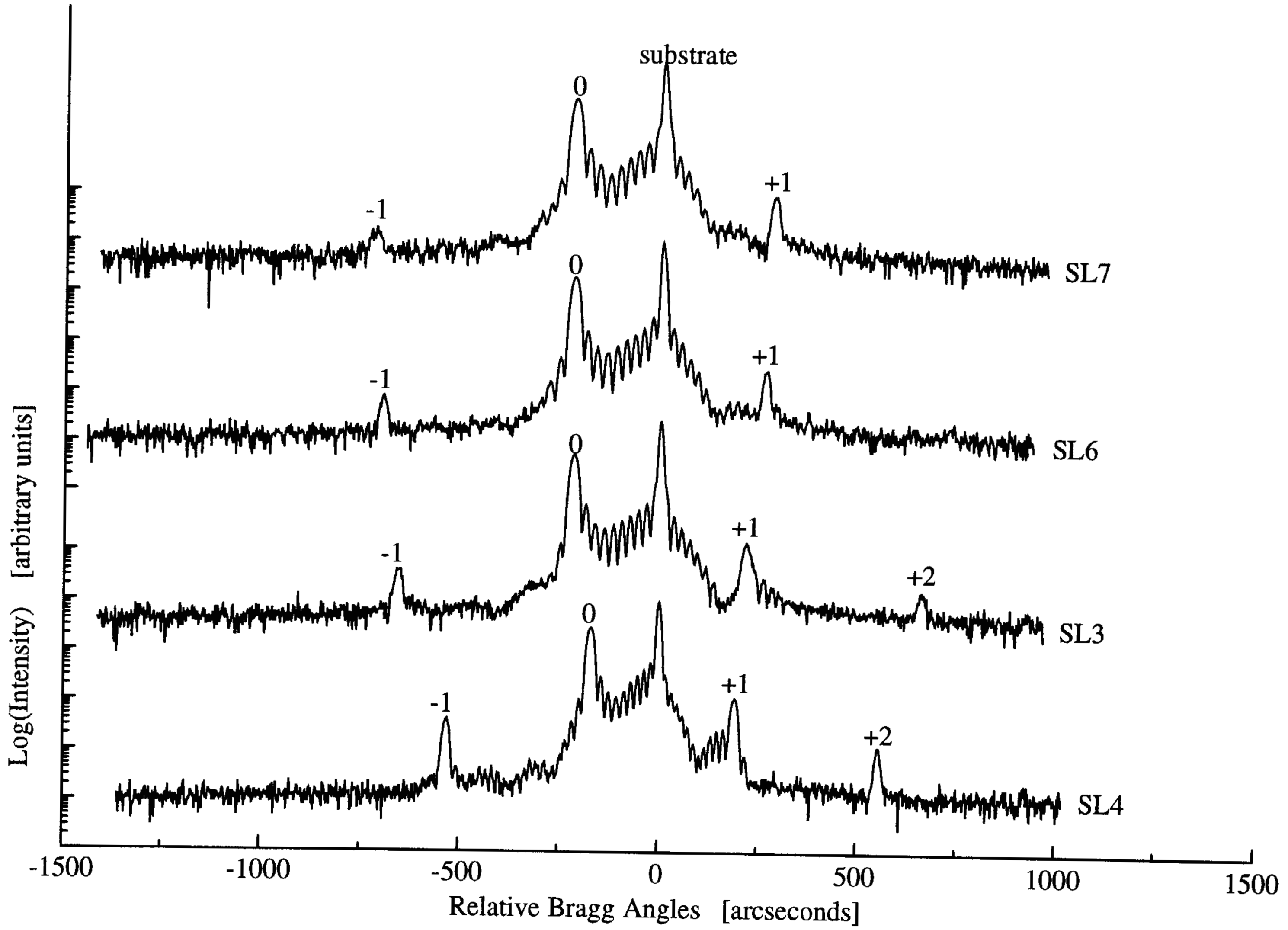

Figure 4-15 Superlattice Rocking Curves from (004) Reflections

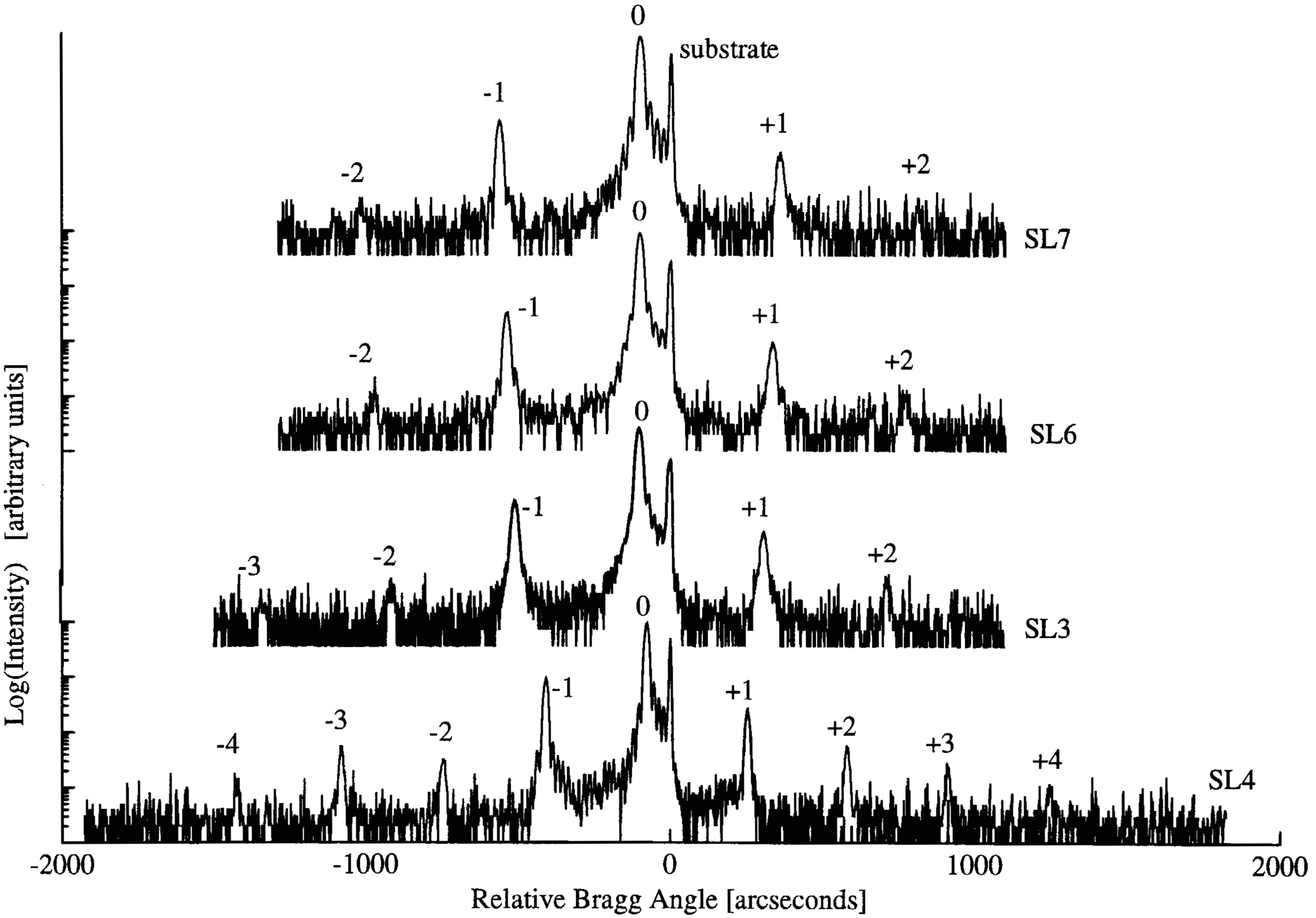

Figure 4-16 Superlattice Rocking Curves from (002) Reflections

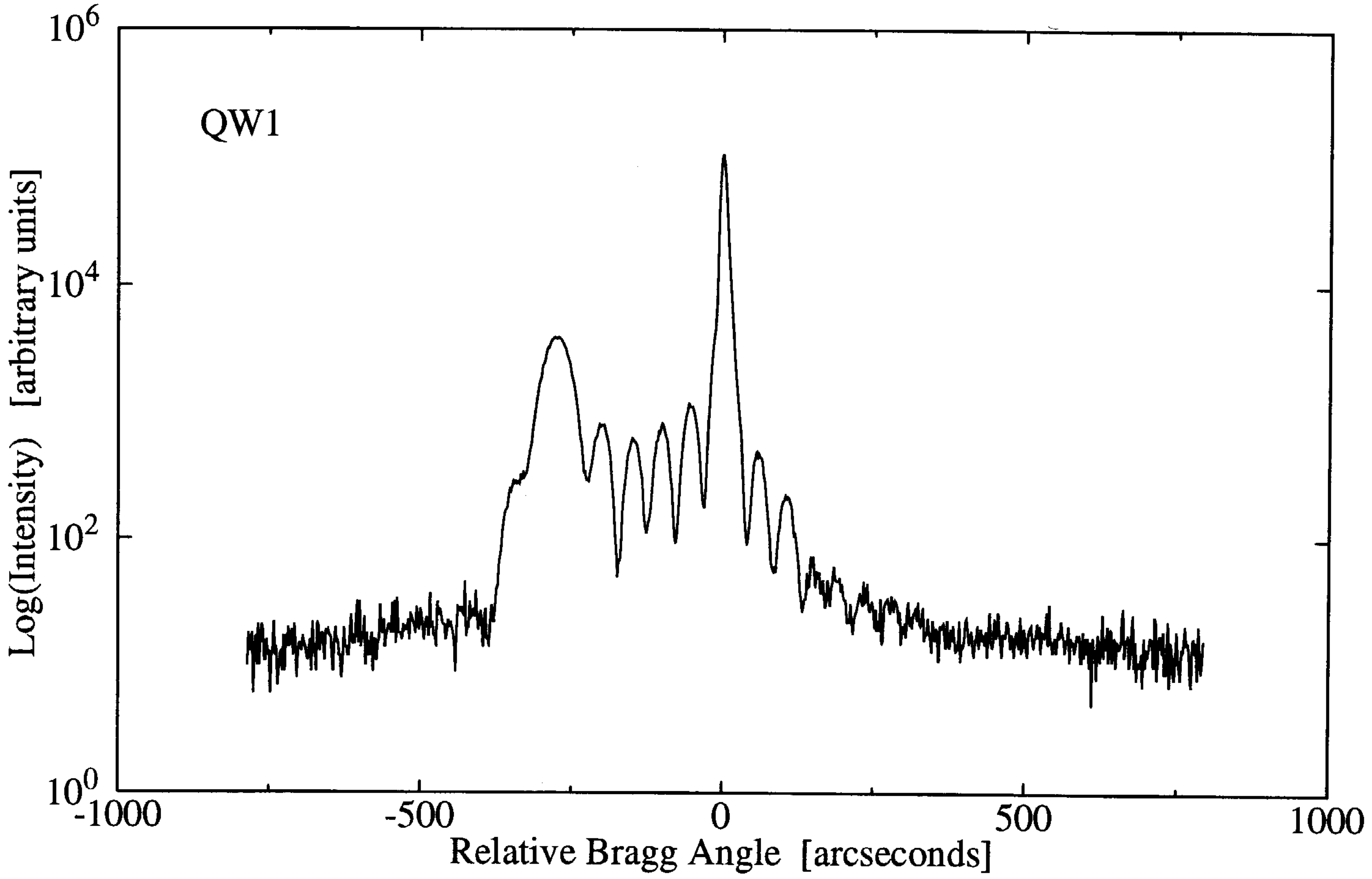

Figure 4-17 Quantum Well Rocking Curve from (004) Reflection

4.4 Interpreting Double Crystal Rocking Curve Data

Quantitative interpretation of the rocking curve data involved the transformation of $\Delta W_{1,2}$, $\Delta\theta$, $\Delta\omega_{PF}$, and $\Delta\omega_{SL}$ into in-plane strain, perpendicular strain, composition, total stack thickness, and superlattice period thickness. These calculations are discussed in detail in Section 4.4.1. The measured data and the strain calculations are listed in Table 4-1 for (115) reflections and in Table 4-2 for (004) and (002) reflections. Composition calculations are tabulated in Table 4-3, and stack thickness and SL period are presented in Table 4-4.

There were two comparison sets for these samples. The first set consisted of superlattices labeled SL3, SL6, and SL7, in which the growth rate for $Al_{0.8}Ga_{0.2}As$ was 2.7μm/hr, 4.0μm/hr, and 5.4μm/hr respectively, all grown with no interruption at heterointerfaces. The second set consisted of the superlattices labeled SL4 and SL6, both grown at the intermediate rate of 4.0μm/hr, with SL4 growth interrupted for 10 seconds at all heterointerfaces and SL6 grown without interruption. The growth data and nominal SL parameters are summarized in Table 3-1.

The qualitative interpretation of the rocking curves required a definition of interface roughness and an understanding of its effect on satellite peak line shape, line width, uniformity, and amplitude. These relations will be presented and discussed in Section 4.4.2.

4.4.1 Calculating Composition, Thickness, and Period

The peak separations measured for each pair of asymmetrical (115) rocking curves on the four superlattice specimens are listed as ΔW_1 and ΔW_2 in Table 4-1. The difference in reflecting plane inclination to the surface between the substrate and epilayer was calculated from the measured peak separations according to the relation $\Delta\phi = (\Delta W_1 - \Delta W_2)/2$, as discussed in section 4.1.2. The difference in Bragg angle

Table 4-1 Rocking Curve Measurements from (115) Reflections

Sample #	Growth Rate & Interrupt	$\Delta W_{0°}$ [arcsec]	$\Delta W_{180°}$ [arcsec]	$\Delta\theta$ [arcsec] ±1 arcsec	$\Delta\phi$ [arcsec] ±1 arcsec	$\Delta a_{//}/a_o$ $[10^{-3}]$ $\pm 0.02\times10^{-3}$	$\Delta a_{\perp}/a_o$ $[10^{-3}]$ $\pm 0.006\times10^{-3}$
SL3	low; no GI	-437	-238	-337	99	0.074	1.768
SL4	medium; 10s GI	-332	-187	-260	73	0.017	1.353
SL6	medium; no GI	-432	-236	-334	98	0.064	1.749
SL7	high; no GI	-431	-235	-333	98	0.072	1.743

Table 4-2 Rocking Curve Measurements from (004) and (002) Reflections

Sample #	(004) Reflection				(002) Reflection			
	$\Delta\theta$ [arcsec] ±1 arcsec	$\Delta\omega_{PF}$ [arcsec] ±1 arcsec	$\Delta\omega_{SL}$ [arcsec] ±1 arcsec	$\Delta a_{\perp}/a_o$ $[10^{-3}]$ $\pm 0.008\times10^{-3}$	$\Delta\theta$ [arcsec] ±1 arcsec	$\Delta\omega_{PF}$ [arcsec] ±1 arcsec	$\Delta\omega_{SL}$ [arcsec] ±1arcsec	$\Delta a_{\perp}/a_o$ $[10^{-3}]$ $\pm 0.020\times10^{-3}$
SL3	-217	22	439	1.713	-93	19	393	1.840
SL4	-170	18	362	1.342	-71	16	327	1.405
SL6	-219	23	475	1.729	-94	20	420	1.859
SL7	-219	24	500	1.729	-95	21	447	1.879

between substrate and epilayer was calculated according to $\Delta\theta = (\Delta W_1 + \Delta W_2)/2$. In-plane strain and perpendicular strain were then calculated from these quantities using Equations 4-1 and 4-2 for lattice mismatch as a function of peak separation. The results for $\Delta a_{//}/a_o$ (see Table 4-1) indicated that the epitaxy was coherent by the criterion that in-plane strain be less than 10^{-4}. Characterization of the layers using perpendicular strain only is justified by this determination of coherent epitaxy.

The main peak separation $\Delta\theta$, the Pendellösung fringe spacing $\Delta\omega_{PF}$, and the superlattice higher order peak separation $\Delta\omega_{SL}$ are tabulated for the (004) and (002) reflections for all specimens in Table 4-2. Perpendicular strain was calculated for each sample using Equation 4-16, which takes the substrate misorientation angle into account.

The magnitudes of perpendicular strain calculated from the (115) and (004) data were in agreement within the error of the calculation, $\varepsilon=\pm0.006\times10^{-3}$ for the (115) reflection and $\varepsilon=\pm0.008\times10^{-3}$ for the (004) reflection. This was expected due to the similar GaAs to $Al_{0.8}Ga_{0.2}As$ signal ratio for these reflections (see Section 4.3.1). The (004) and (115) reflections are both more sensitive to GaAs than to AlGaAs. For instance, at x=0.17 the (004) structure factor of $Al_{0.17}Ga_{0.83}As$ is an order of magnitude smaller than that of GaAs, and therefore AlGaAs of composition less than 0.17 is not distinguishable in these reflections.

However, the magnitudes of perpendicular strain calculated for the (002) reflections are substantially larger even within the calculation error for this reflection of $\pm0.020\times10^{-3}$. The larger calculation error for this reflection is a result of the smaller Bragg angle, for which small differences in angular separation produce large differences in the perpendicular strain due to the magnitude of $\tan\theta_B$. The increase in perpendicular strain calculated for this reflection is due to the increased sensitivity of this reflection to Al content in the layers. For this reflection, the structure factor of AlGaAs at x=0.17 is almost twice that of GaAs. The structure factor of AlGaAs at x=0.05 is 30% that of GaAs.

Thus the (002) reflection sees aluminum at concentrations well below the sensitivity of the (115) and (004) reflections, down to $x=0.05$. This increased sensitivity is expected to result in a larger perpendicular strain associated with greater average aluminum concentration. This difference in average Al concentration consequently provides a measure of the amount of ternary material in the $0.05<x<0.17$ range, indicating the presence of a low-aluminum interface layer which will be correlated to gas interdiffusion in the manifold in Chapter 5.

The specimen which was growth interrupted at all heterointerfaces, SL4, showed less perpendicular strain than those without growth interruptions, indicating that the average aluminum concentration in this superlattice stack was less than the concentration in the uninterrupted SLs. The implications of this finding, that GaAs continues to grow during the interrupt interval, will be discussed in conjunction with the model of gas interdiffusion in the manifold in Chapter 5.

The perpendicular strain values from all reflections were used to calculate the average mole fraction $\bar{x}$ of aluminum in the SLs. One series of calculations was made using the assumption, common in the literature, that the elastic constants of the epilayer can be approximated by the well known constants of the GaAs substrate [100, 101]. The relation used to calculate this series follows from Equation 4-8 with $\Delta\nu=0$:

$$\bar{x} = \left(\frac{1-\nu_{Ga}}{1+\nu_{Ga}}\right) \cdot \frac{(\Delta a_{\perp}/a_o)}{(\Delta a_{AlAs}/a_o)} \qquad \text{Eqn. 4-17}$$

The lattice mismatch used for binary AlAs was 1620 ppm as discussed in Section 4.1.3 [7]. These composition calculations are listed in Table 4-3 under the heading $\bar{x}[\nu=\nu_{GaAs}]$. A second series of calculations was made using the quadratic fit of a_{AlAs} and ν_{AlAs} which resulted in Equation 4-9. These composition results are listed under the heading $\bar{x}[\nu=\nu_{GaAs}-\bar{x}\Delta\nu]$.

Table 4-3 Average SL Composition Calculated from Strain

Sample #	$\bar{x}[\nu=\nu_{Ga}]$			$\bar{x}[\nu=\nu_{Ga}-\bar{x}\Delta\nu]$		
	(115) ±0.002	(004) ±0.003	(002) ±0.006	(115) ±0.002	(004) 0.003	(002) ±0.007
SL3	0.57	0.56	0.60	0.61	0.59	0.63
SL4	0.44	0.44	0.46	0.46	0.45	0.48
SL6	0.57	0.56	0.60	0.60	0.59	0.64
SL7	0.57	0.56	0.61	0.60	0.59	0.65

The composition calculations using the substrate elastic constants to approximate those of the epilayer produced results indicating less average aluminum in the structures than the calculations in which the Poisson's ratio was adjusted for composition. This is due to the fact that AlAs is a stiffer material than GaAs, requiring more force (i.e., a greater difference in lattice constant) to achieve the same degree of elastic deformation. That is, if AlGaAs had the same Poisson's ratio as GaAs it would deform more easily, thus increasing the amount of perpendicular strain for a given composition. The Poisson's ratio for AlGaAs is smaller than that for GaAs, so more aluminum in the ternary is necessary for AlGaAs to deform to a degree resulting in the same perpendicular strain. The calculations using Poisson's ratio $\nu = \nu_{Ga} - x\Delta\nu$ are more accurate because they take the changing elastic characteristics of ternary AlGaAs into account. All further calculations requiring the average mole fraction of aluminum were performed using the results obtained with the adjusted Poisson's ratio.

The composition results for the (002) reflections indicated a greater average mole fraction of Al in the SL stacks for all samples, consistent with the greater sensitivity of this reflection to AlAs and its reduced sensitivity to GaAs. In the (004) reflection the $|F_{GaAs}|$: $|F_{AlGaAs}|$ ratio is large for $0<x<0.2$ and material in this composition range effectively diffracts as GaAs. In the (002) reflection, in contrast, the $|F_{GaAs}| : |F_{AlGaAs}|$ is small, even for compositions of $0.05<x<0.2$, so that material with any Al content greater than $x=0.05$ will effectively diffract as AlGaAs, thus increasing the average Al mole fraction measured in the SL stack.

The growth-interrupted specimen showed a reduced average Al mole fraction consistent with the continued growth of GaAs during the interrupt interval. This will be addressed in greater detail in the discussion of layer thicknesses.

The SL stack thickness and period can be calculated independently from either Pendellösung fringes or satellite peaks [96]. It is then possible to compute approximate well and barrier thicknesses from the number of periods, the average Al mole fraction, and either the total stack thickness or the SL period. Results obtained using each method can be compared to confirm the consistency of the measurements These two approaches to the calculation of stack thickness and SL period are presented in Table 4-4.

In the first section, Table 4-4(a), the stack thicknesses were calculated according to Equation 4-10 using the angular separation between the Pendellösung fringes. The stack thickness results from (004) and (002) reflections were in good agreement given the accuracy of the measurements. The angular separation measurement had an error of ±1 arcsecond, leading to an error in the thickness of approximately ±350Å for the (004) reflection and ±400Å for the (002) reflection in the range of the Pendellösung fringe separation. The other entries in Table 4-4(a) are SL period, barrier, and well thicknesses calculated indirectly from the total stack thickness and the measured average Al mole fraction. These calculations were based on a two-layer SL model with abrupt interfaces and $x=0.80$ in the AlGaAs barriers, which is clearly an over-simplification for these structures. A more rigorous three-layer model with exponentially decaying mole fraction in the third (interfacial) layer will be developed in Chapter 5.

These simplified calculations do provide information on the relative thicknesses of wells and barriers in the SL as compared to the nominal thicknesses. The barriers were

Table 4-4 Stack Thickness, SL Period, and Layer Thickness

Sample #	Stack Thickness D [Å] (Eqn. 4-10)		SL Period p(D) [Å]		Barrier Thickness t_b(D) [Å]		Well Thickness t_w(D) [Å]	
	(004) ±350Å	(002) ±400Å	(004) ±17Å	(002) ±20Å	(004) ±12Å	(002) ±15Å	(004) ±5Å	(002) ±5Å
SL3	8612	8681	416	418	302	326	114	92
SL4	10526	10309	512	501	282	295	230	206
SL6	8237	8247	397	397	289	314	108	83
SL7	7894	7854	381	378	277	304	104	74

(a) SL Period and Layer Thicknesses Calculated from Stack Thickness

Sample #	SL Period p [Å] (Eqn. 4-11)		Stack Thickness D(p) [Å]		Barrier Thickness t_b(p) [Å]		Well thickness t_w(p) [Å]	
	(004) ±2Å	(002) ±2Å	(004) ±4Å	(002) ±4Å	(004) ±2Å	(002) ±2Å	(004) ±4Å	(002) ±4Å
SL3	432	419	8954	8706	314	326	118	93
SL4	524	505	10768	10397	288	297	236	208
SL6	399	393	8270	8157	290	311	109	82
SL7	379	369	7856	7677	276	297	103	72

(b) Stack and Layer Thicknesses Calculated from SL Period

increased from the designed thickness of 225Å by about 50-75Å, and the wells in the uninterrupted samples were decreased from their nominal thickness of 125Å by 10-40Å, a pattern which is consistent with continued growth of $Al_xGa_{1-x}As$ for some time after the Al source had been switched to vent. The increase in barrier thickness was seen for all samples, including SL4 with growth interruption. In that specimen, however, the well thickness was actually increased by 75-100Å, consistent with the continued growth of GaAs during the interrupt interval following the switch to vent of the Ga source.

In the second section of the table, Table 4-4(b), the SL period was calculated directly from the angular separation of the higher order satellite peaks according to Equation 4-11. SL period results calculated directly from $\Delta\omega_{SL}$ for (004) and (002) reflections were in reasonable agreement given the magnitude of error in the angular separation measurements. The error in the angular measurements, ±1", resulted in an error in the period of ±2Å for both reflections in the range of satellite peak separation. The other entries in Table 4-4(b) are total stack, barrier, and well thicknesses calculated indirectly from the period thickness and the measured average Al mole fraction. These calculations were based on the same two-layer model used in Table 4-4(a), with the same limitations.

Relative barrier and well thicknesses calculated from $\Delta\omega_{SL}$ using the simplified model showed the same variation as they did when calculated from $\Delta\omega_{PF}$. Barrier thicknesses were increased from designed values in all SLs by approximately 50-75Å. Well thickness were decreased from designed values by 10-30Å in the uninterrupted samples, but increased by 75-100Å in the interrupted sample. These barrier and well thicknesses calculated from SL period and those calculated from stack thickness were in good agreement, indicating that both $\Delta\omega_{PF}$ and $\Delta\omega_{SL}$ provided consistent measures of stack and layer thickness.

Total stack thickness as measured was 0.75-0.86 μm for the uninterrupted samples and 1.02-1.06 μm for the SL with growth interruption. This is an increase over the stack thickness as designed, which was 0.72 μm. Since this increase was seen even in the samples for which there was no Ga switching (the uninterrupted samples), this part of the thickness difference may be associated with an Al switching transient caused by interdiffusion of DMAlH in the manifold. This transient will be modelled as a function of the increase in stack thickness in Chapter 5.

The increase in stack thickness in SL4, grown with interrupts at both interfaces, was greater than that measured in the uninterrupted samples. Preliminary calculations of barrier and well thickness for this sample indicated that the barrier thickness was approximately the same in the interrupted sample and the uninterrupted samples, but the well thickness was more than doubled in SL4. Since this increase in well thickness is observed only in the growth-interrupted sample, it may be associated with a switching transient caused by interdiffusion of TMGa in the manifold. This transient will be characterized as a function of the increase in well thickness in Chapter 5.

The stack thicknesses listed in Table 4-4(a) and the SL periods in Table 4-4(b) were values calculated directly from measurements of $\Delta\omega_{PF}$ and $\Delta\omega_{SL}$ and will be used as parameters in the model. The barrier and well thicknesses listed in Table 4-4 were all calculated indirectly based on the abrupt junction two-layer SL model and are therefore not an accurate description of the structures. The comparison of these calculated well and barrier thicknesses can, however, be used as a motivation for the three-layer model with two distinct transients, one for DMAlH and the other for TMGa, which will be developed in Chapter 5. In addition, the apparent inverse relation between growth rate and thickness of the transient-induced layer seen in the data for SL3 (2.7μm/hr), SL6 (4.0μm/hr), and SL7 (5.4μm/hr) will be investigated in Chapter 5.

4.4.2 Qualitative Interface Evaluation

The x-ray diffraction technique measures average material parameters over a volume of material defined by the spot size of the incident x-ray and the extinction depth of that x-ray wavelength for the particular material and reflection geometry [129]. Thus the lineshape and magnitude of rocking curves on SLs represent structural characteristics of the material averaged over a fairly large volume. These rocking curve parameters are highly sensitive to both random and non-random variations in thickness and composition because these effects are cumulative in SL structures [4-5, 129-131]. A limited amount of qualitative information on random layer thickness variation, random composition variation, and uniform interface grading can consequently be deduced from the satellite peak line shape, line width, symmetry with respect to the main SL peak, and amplitude [92-94, 110-114].

The full width half maximum (FWHM) of a higher order SL satellite peak increases with order due to the increasing deviation from non-dispersive geometry which occurs as the angle of incidence deviates from the Bragg angle during the scan [102]. Thus the FWHM of a SL peak increases with the order of the peak. In addition, the cumulative effects of random variations in layer thickness result in symmetrical broadening of SL peaks of all orders [129,130]. A consistent symmetrical broadening of satellite peaks independent of order is generally attributed to random variations in the SL period due to layer thickness fluctuations [92, 112, 124].

In the specimens examined for this investigation, the angular range of the scan was within ±1200 arcseconds of the Bragg angle for both (004) and (002) reflections, so that higher order peak broadening due to deviation from the Bragg angle was expected to be small. In the (004) reflections there was no measurable difference in FWHM of the main SL peak (about 40 arcseeconds in uninterrupted samples and 30 arcseconds in SL4) and the FWHM of the plus and minus first order peaks in any of the SL specimens except SL7, for which the FWHM of the -1 peak was increased to 50 arcseconds (see Figure 4-14). From this it was inferred that the layer thicknesses of the barriers and wells in the SLs were fairly uniform, although no quantitative measure of the maximum variation could be computed without complete simulation of the rocking curves.

In the (002) reflections (see Figure 4-15) the main peak and higher order peak

FWHM were identical for all peaks measured in SL3 and SL6 (40 arcseconds in both specimens). The (002) results for SL7 showed main peak and first order peaks to be 40 arcseconds in width, and the second order peaks to be 50 arcseconds. (SL7 may be less uniform than the other SLs due to the increase in manual switching error at the higher growth rate.) Results from SL4, the growth-interrupted sample, showed main peak and first order peaks to be 30 arcseconds in width, and the second and third order peaks to be 40 arcseconds. From this is was concluded that variations in barrier and well thicknesses through the entire stack in all specimens were small compared to the error in the measurement (±2 arcseconds). The decreased linewidths in the growth-interrupted sample may indicate that thicknesses are more uniform in this sample. This point will be investigated in the model in Chapter 5.

Higher order peaks decrease monotonically in amplitude in ideal SL structures [93, 112]. An additional decrease in satellite amplitude is associated with an increase in the uncertainty of the interface position due to random fluctuations in composition at the interface [5, 124, 129]. When the random compositional fluctuation has a broad spatial distribution, the higher order peaks are suppressed entirely [131]. Therefore the number of higher order peaks in the rocking curve and their relative amplitudes provide qualitative information on the spatial extent of random compositional fluctuations. The number of satellite peaks must be interpreted with caution, however, because it is also a strong function of the x-ray intensity incident on the sample. In rocking curves from the less sensitive (004) reflection, all samples showed first order satellite peaks easily distinguishable from the background. Rocking curves on SL3 and SL4 also showed +2 peaks. In the more sensitive (002) reflection, all samples showed first and second order satellite peaks. SL4 also showed third and fourth order peaks. Since the incident x-ray intensity is relatively low in these measurements, it is not possible to distinguish higher order peak suppression due to random compositional variation from the monotonic decrease in satellite amplitude predicted for ideal SLs.

Regular variation in composition (grading) at interfaces has been shown to result in asymmetrical broadening of the higher order satellite peaks [102, 109, 131]. The SL peaks of SL4, SL6, and SL7 in both (004) and (002) geometries were slightly asymmetrical. This asymmetry was visible only in linear-linear plots magnified near each satellite. Thermodynamic interdiffusion of reactants in the gas manifold would result in a decaying concentration of DMAlH after this reactant had been switched to vent, causing a regular graded interface layer at each AlGaAs-to-GaAs interface. The satellite peak asymmetry seen in these measurements supports the presence of such a graded layer. Rocking curves for SL3 in both (004) and (002) geometries showed a more distinct asymmetry of the higher order peaks. This is the specimen which was grown at the lowest growth rate, R_g(AlGaAs)=2.7μm/hr. It is likely that interdiffusion of reactants would have a greater effect on the composition of the epitaxial material when the growth rate is reduced. This possibility will be discussed in connection with the bandgap models in Chapter 5.

A difference in amplitude between a +n satellite peak and its -n counterpart is associated with additional distinct layers in the SL. Best fits determined from simulation programs indicate that such asymmetrical amplitudes of ±n peaks can be reproduced in simulations by the addition of interfacial layers [93-94, 117-119]. Without simulation it is not possible to determine the spatial extent or the composition of these additional layers, but their presence may be inferred from higher order peak amplitude asymmetry. The ±1 peaks in both reflections for all samples showed amplitude asymmetry. In the (002) reflection, in which more higher order peaks were obtained, this amplitude asymmetry was visible in ±2 and ±3 higher order pairs. This observation also supports the conclusion that there is an additional distinct layer in these structures.

The qualitative interpretation of the rocking curves can be summarized as follows: Random variation in layer thickness is probably small in all samples; no qualitative description of random variation in composition is possible from these data; and a layer of graded composition is expected at every AlGaAs-to-GaAs interface. Two predictions from the qualitative interpretation are made, first that layer thicknesses are uniform and second that there is an additional distinct layer in these SL structures between the $Al_{0.8}Ga_{0.2}As$ barriers and the GaAs wells in which the Al composition varies from 0.8 to zero as a function of a decaying concentration tail of DMAlH in the gas manifold.

The stack thicknesses and SL periods calculated directly from $\Delta\omega_{PF}$ and $\Delta\omega_{SL}$ in Section 4.4.1 will be used in conjunction with these qualitative predictions to develop a model of reactant interdiffusion in the manifold which will best describe the resulting structures and allow improved control of structural parameters in the future.

Chapter 5

Model of Reactant Concentration in System Manifold

The purpose of this work was to characterize the fast-switch manifold in the IV-MOCVD system and evaluate its effectiveness in rapid control of the concentration of reactants. In order to predict system behavior, a model of the switching transient in the manifold was constructed using DCRC data. The model was intended to be a starting point for systematic process control adjustments to achieve the growth of low-dimension structures with good control of layer thickness and composition. This chapter addresses the construction of the model of gas dynamics in the manifold, the derivation of layer thicknesses from the concentration model, the calculation of bandgaps and luminescence energies from the model, and the prediction of photoluminescence results.

5.1 Extracting Switching Coefficients from Rocking Curve Data

The fast-switch manifold was designed with four-valve control and a make-up manifold intended to provide pressure equalization during switching. Characterization of the unique valve design has demonstrated that concentration pulses in the manifold are free of spikes and fluctuations caused by pressure variation [132]. This previous characterization of the manifold was performed by mass spectrometer measurements of gas concentrations in the manifold itself. However, measurements taken in the manifold may not accurately describe the time-dependent behavior of the reactant concentration at the growing surface due to the fact that, as the concentration pulse travels down the manifold toward the reactor and the growing surface, the reactant species interdiffuses with the carrier gas at the leading and lagging edges of the pulse. This produces a time-dependence of concentration which is no longer a square pulse. Figure 5-1(a) shows the ideal concentration pulse as a function of time. Figure 5-1(b) shows the interdiffused pulse. It is necessary to describe the rise and fall times of the actual concentration pulse in order to predict growth rates, thicknesses, and compositions of material grown.

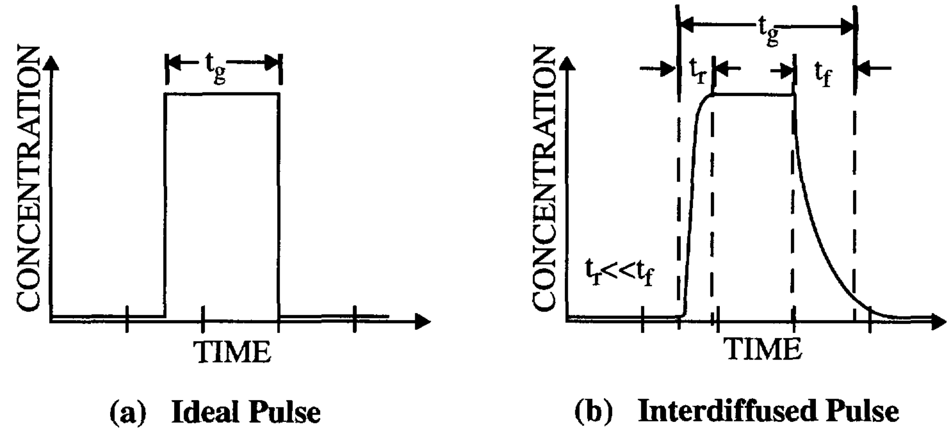

(a) Ideal Pulse **(b) Interdiffused Pulse**

Figure 5-1 Ideal and Interdiffused Concentration Pulses

The net forward velocity of the gas stream inhibits interdiffusion at the leading edge of the pulse and enhances interdiffusion at the lagging edge. For this model, interdiffusion of reactant with carrier gas at the leading edge t_r was considered to be negligible compared to the duration of the pulse t_g. This assumption was based on the previous characterization of the pulse in the manifold [132]. However, the enhanced interdiffusion at the lagging edge was not negligible, as shown by the DCRC measurements of layer thickness which were 5% to 20% greater than designed. The finite gradient of the concentration pulse at the lagging edge resulted in the growth of an additional $Al_xGa_{1-x}As$ layer with decaying Al mole fraction between the barrier layer of $Al_{0.8}Ga_{0.2}As$ and the well layer of GaAs. DCRC data indicating increased period and stack thickness can be used to evaluate the temporal and spatial extent of the lagging edge interdiffusion.

It should be noted that this gradient at the lagging edge of the concentration pulse may be due not only to interdiffusion during transit from the switching point to the growing surface, but also to residence time of the reactant species in recirculation loops near the substrate. Recirculation loops in this reactor geometry have been shown to be localized to the reactor wall [47], as shown in Figure 2-5(d), but no determination of residence time is possible with the current instrumentation. Further analysis of the concentration pulse at the growing surface is based on the assumption that the time dependence of the concentration is a composite function of both interdiffusion during transit and residence time in recirculation loops which can be described by a decaying exponential with a single time constant.

5.1.1 Layer Thickness as a Function of Concentration

The growth rate of epitaxial material in this system is a linear function of the Group III reactant concentration at the growing surface under conditions of constant V:III ratio and substrate temperature (see Sections 3.2.2, 3.2.3, and 3.2.4). The thickness and composition of material grown are in turn functions of the growth rate and the ratio of DMAlH concentration to total Group III concentration. Consequently both thickness and composition can be expressed as functions of the time-dependent concentration of reactants at the growing surface, according to the relations:

$$R_g(AlGaAs) = C_A[Al(t)] + C_G[Ga(t)] \qquad \text{Eqn. 5-1}$$

$$d = \int_{t_g} R_g(t)\,dt = \int_{t_g} \{C_A[Al(t)] + C_G[Ga(t)]\}\,dt \qquad \text{Eqn. 5-2}$$

$$x = \frac{R_g(AlAs)}{R_g(AlGaAs)} = \frac{C_A[Al(t)]}{C_A[Al(t)] + C_G[Ga(t)]} \qquad \text{Eqn. 5-3}$$

In these equations R_g is the solid phase growth rate, the square brackets [ ] represent gas phase concentration of Group III sources, $C_{A,G}$ are the constants relating gas phase concentration to growth rate for AlAs and GaAs respectively, d is the thickness of material grown in a given interval, and x is the mole fraction of Al in the material at a given time.

In the ideal case of perfectly abrupt switching, the reactant concentration in the manifold can be represented by the square pulse shown in Figure 5-1(a) and the growth rate, thickness, and composition may be expressed as functions of the steady state reactant concentrations, $[Al_0]$ and $[Ga_0]$, over the interval of growth:

$$R_g(AlGaAs) = C_A[Al_0] + C_G[Ga_0] \qquad \text{Eqn. 5-4}$$

$$d = \{C_A[Al_0] + C_G[Ga_0]\} \cdot t_g \qquad \text{Eqn. 5-5}$$

$$x = \frac{C_A[Al_0]}{C_A[Al_0] + C_G[Ga_0]} \qquad \text{Eqn. 5-6}$$

This ideal case description is accurate for bulk materials in which the interval of a single switching event, t_g, is very much greater than the decay time of the switching transient, τ_f. Under these circumstances, Equations 5-1, 5-2, and 5-3 are well approximated by Equations 5-4, 5-5, and 5-6 as $(\tau_f/t_g) \rightarrow 0$. The calibration of growth rates from thick layers of bulk material was performed under these conditions.

When the interval of a switching event is comparable in duration to the decay time of the switching transient, Equation 5-2 must be evaluated using an explicit time-dependent function for growth rate. In the case of superlattice growth, repeated switching leads to an accumulation of switching transients comparable in duration to the intervals of barrier and well growth. The results of these transients can be measured as a difference in SL period and also as a difference in total stack thickness. The reactant concentration at the growing surface can be modeled by piecewise continuous functions over the time interval of one SL period. Relevant sections of the switching interval are defined in Figure 5-2 for the case of uninterrupted growth (no switching of the TMGa source).

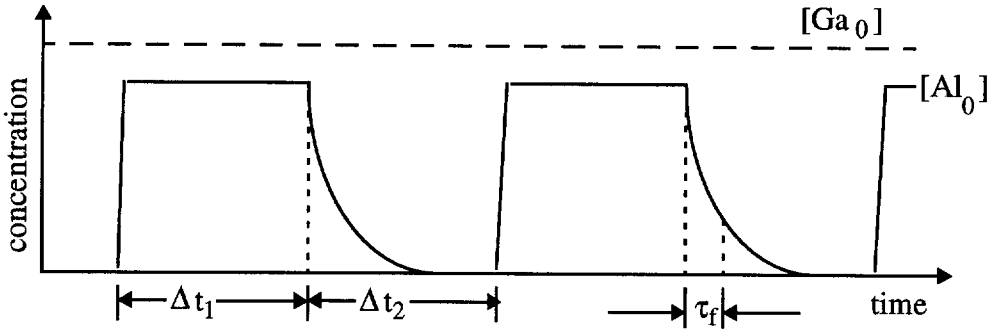

Figure 5-2 Integration Segments of Switching Interval

The interval designated Δt_1 is the nominal growth time of the $Al_{0.8}Ga_{0.2}As$ barrier layers, Δt_2 represents the growth time of the GaAs wells, and τ_f is the interval in which the DMAlH concentration at the growing surface drops to $[Al_0]e^{-1}$. Al concentration during the interval Δt_1 is described by its steady state value. Al concentration during the interval Δt_2 is modeled as the decaying exponential function $[Al(t)] = [Al_0]\exp(-t/\tau_A)$. The fall time τ_f of the Al concentration in this expression is specified as τ_A. Substituting these functions into Equation 5-2 and integrating over the interval of one period results in an expression for the thickness of the SL period, p:

$$p = \int_{\Delta t_1} (C_A[Al_0] + C_G[Ga_0])\,dt + \int_{\Delta t_2} \left(C_A[Al_0]\,e^{-t/\tau_A} + C_G[Ga_0]\right)dt \qquad \text{Eqn. 5-7}$$

The growth intervals for barriers and wells were identical in all specimens grown for this investigation, that is, $\Delta t_1 = \Delta t_2 = \Delta t$, and Equation 5-7 can therefore be further simplified to:

$$p = (C_A[Al_0] + 2C_G[Ga_0]) \cdot \Delta t + (C_A[Al_0]) \int_{\Delta t} e^{-t/\tau_A}dt \qquad \text{Eqn. 5-8}$$

The first RHS term in Equation 5-8 is identical with the results obtained from applying Equation 5-5 over an entire SL period. It represents the thickness of one SL period as calculated from the bulk growth rate calibrations. The measured period, p, is composed of the contribution of the steady state portions of the period, p_0, and the thickness of the additional material grown in each period, Δp, due to the decaying exponential tail of the Al concentration. The difference between the period thickness as measured and the period thickness as designed can be expressed as a function of the composite time constant of DMAlH at the growing surface:

$$p - p_0 = \Delta p = (C_A [Al_0]) \int_{\Delta t} e^{-t/\tau_A} dt = C_A [Al_0] \cdot \tau_A \cdot \left(1 - e^{-\Delta t/\tau_A}\right) \qquad \text{Eqn. 5-9}$$

This expression can be evaluated numerically using period thickness measurements obtained on the SL specimens grown without interruption.

Equation 5-9 is valid only when the switching time constant τ_A of DMAlH is less than the growth interval for the GaAs well, as is the case in Figure 5-2. If the switching time constant is greater than the growth interval for the well, the Al concentration during barrier growth cannot be described by its steady state value alone. An additional term representing the concentration of DMAlH still present from the previous barrier must be included in the calculation. This accumulation of additional Al from previous periods is illustrated in Figure 5-3.

Inclusion of additional Al from the preceding barrier results in Equation 5-10, in which the exponential in the integrand of the first RHS term represents the additional Al concentration still present from the previous switching period. If the diffusion coefficient is sufficiently large that this term is not negligible in the next well (the interval of the second integrand), then a third term of the form $C_A[Al_0]\exp\{-(t+2\Delta t)/\tau_A\}$ must be added to the second RHS integrand in Equation 5-10.

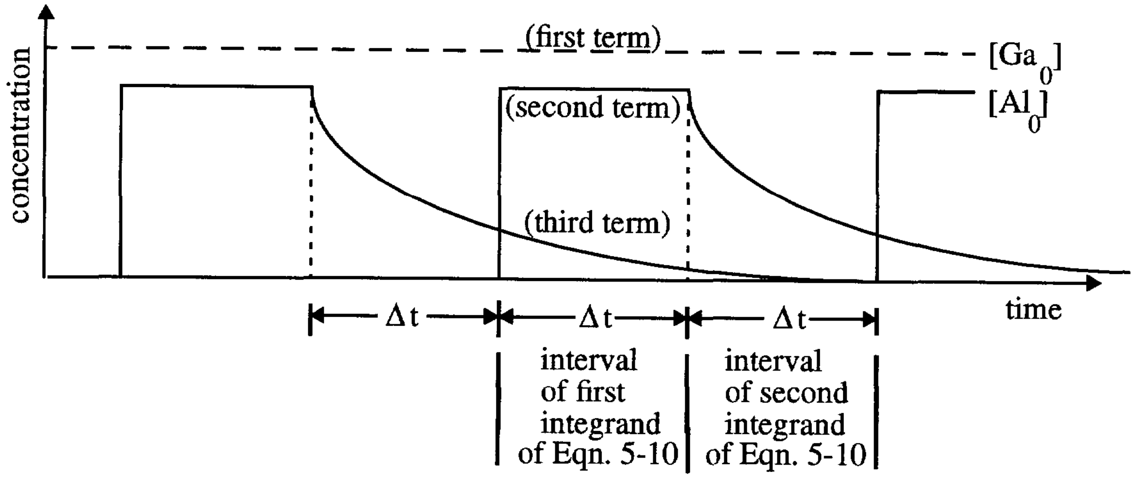

Figure 5-3 Additional Reactant Concentration

$$p = \int_{\Delta t} \left(C_G [Ga_0] + C_A [Al_0] + C_A [Al_0] e^{-(t+\Delta t)/\tau_A} \right) dt$$

$$+ \int_{\Delta t} \left(C_G [Ga_0] + C_A [Al_0] e^{-t/\tau_A} \right) dt \qquad \text{Eqn. 5-10}$$

Comparison of the period calculated from Equation 5-10 with that from Equation 5-5 results in an expression for the difference in measured and designed periods. This relation is Equation 5-11, which can be evaluated numerically subject to the condition that the third term in the second integration interval is negligible, that is, $\exp(-2\Delta t/\tau_A) \leq 0.01$.

$$\Delta p = C_A [Al_0] \left(1 + e^{-\Delta t/\tau_A} \right) \int_{\Delta t} e^{-t/\tau_A} dt = C_A [Al_0] \cdot \tau_A \cdot \left(1 - e^{-2\Delta t/\tau_A} \right) \qquad \text{Eqn. 5-11}$$

If the requirement that the Al diffusion tail from the previous period be no more than 1% of steady state is not met, the addition of the third term in the second integration interval results in Equation 5-12, which can be evaluated numerically subject to the condition that $\exp(-3\Delta t/\tau_A) \leq 0.01$.

$$\Delta p = C_A[Al_0] \cdot \tau_A \cdot \left(1 - e^{-3\Delta t/\tau_A}\right) \qquad \text{Eqn. 5-12}$$

5.1.2 DMAlH Switching Coefficient as a Function of Growth Rate

DMAlH switching coefficients were determined by numeric evaluation of Equations 5-11 and 5-12 for the three SL specimens grown at different growth rates without interface growth interruption. The results are listed in Table 5-1. Using the switching coefficients obtained from Equation 5-12, the three-term model for concentration versus time was evaluated for each of the specimens. The results represent the switching cycles for each specimen and are presented graphically in Figure 5-4. These switching cycles indicate that the DMAlH concentration at the growing surface does not go to zero during the interval of well growth for the growth rates and intervals used here. The additional concentration of DMAlH which is always present in these SLs results in deviation from the designed structure. Bandgap models developed in Section 5.2 will demonstrate some of these structural changes.

Table 5-1 Numeric Evaluation of Switching Coefficients.

Sample #	$C_A[Al_0]$ [Å/sec]	Δt [sec]	τ_A [sec] from Eqn. 5-11	$e^{(-2\Delta t/\tau_A)}$	τ_A [sec] from Eqn. 5-12	$e^{(-3\Delta t/\tau_A)}$
SL3	3.2	30	28	0.12	24	0.01
SL6	4.7	20	10	0.02	10	0.00
SL7	6.3	15	4	0.00	4	0.00

The composite time constants in Table 5-1 show an inverse dependence on growth rate. An increase in the gas phase diffusivity of the reactant due to longer residence time for lower growth rates does not seem feasible, since the total flow through the system was constant at 2.9 slpm for all growth rates, as measured in previous experiments [47]. Resi-

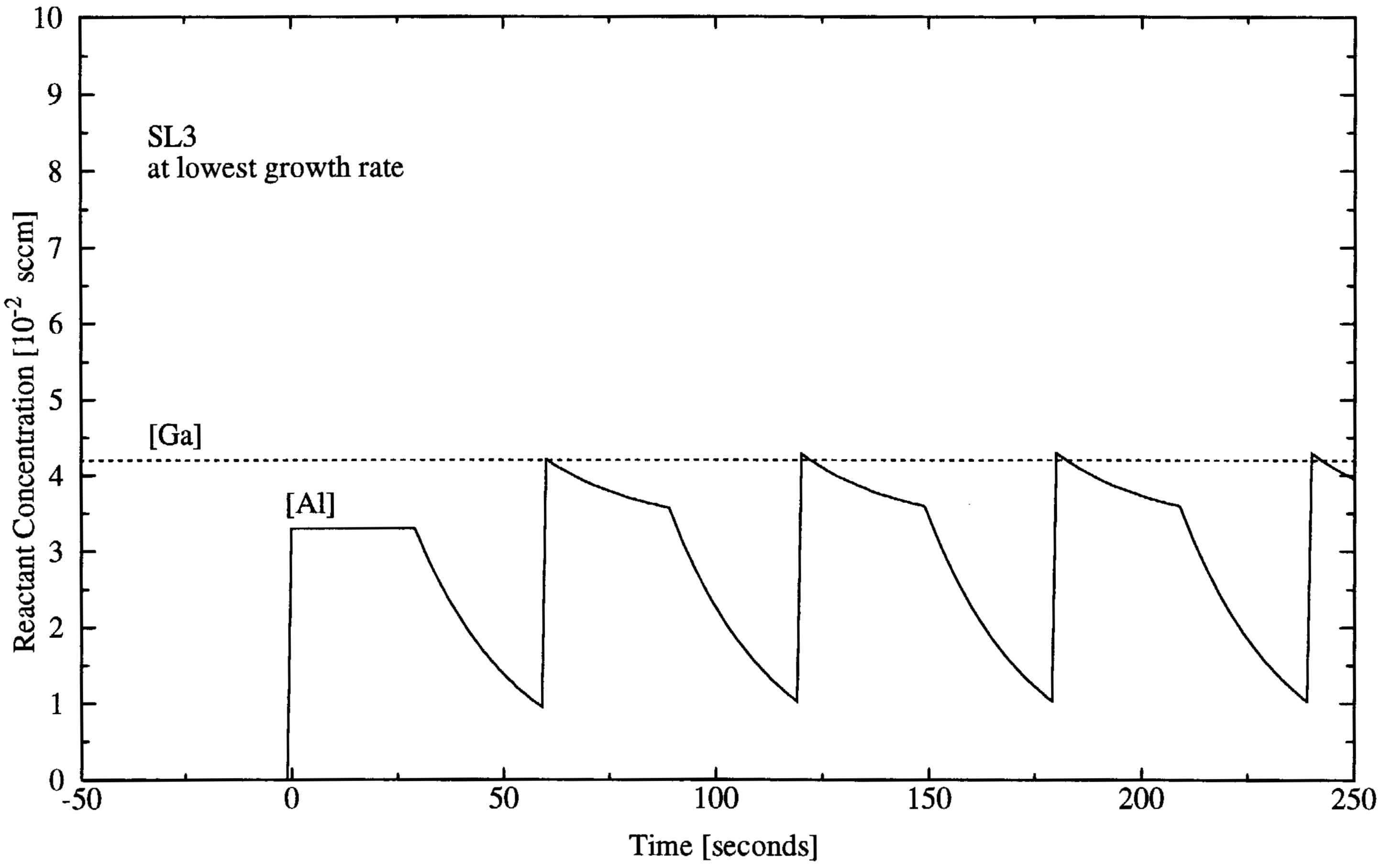

Figure 5-4 (a) Switching Cycle of SL3

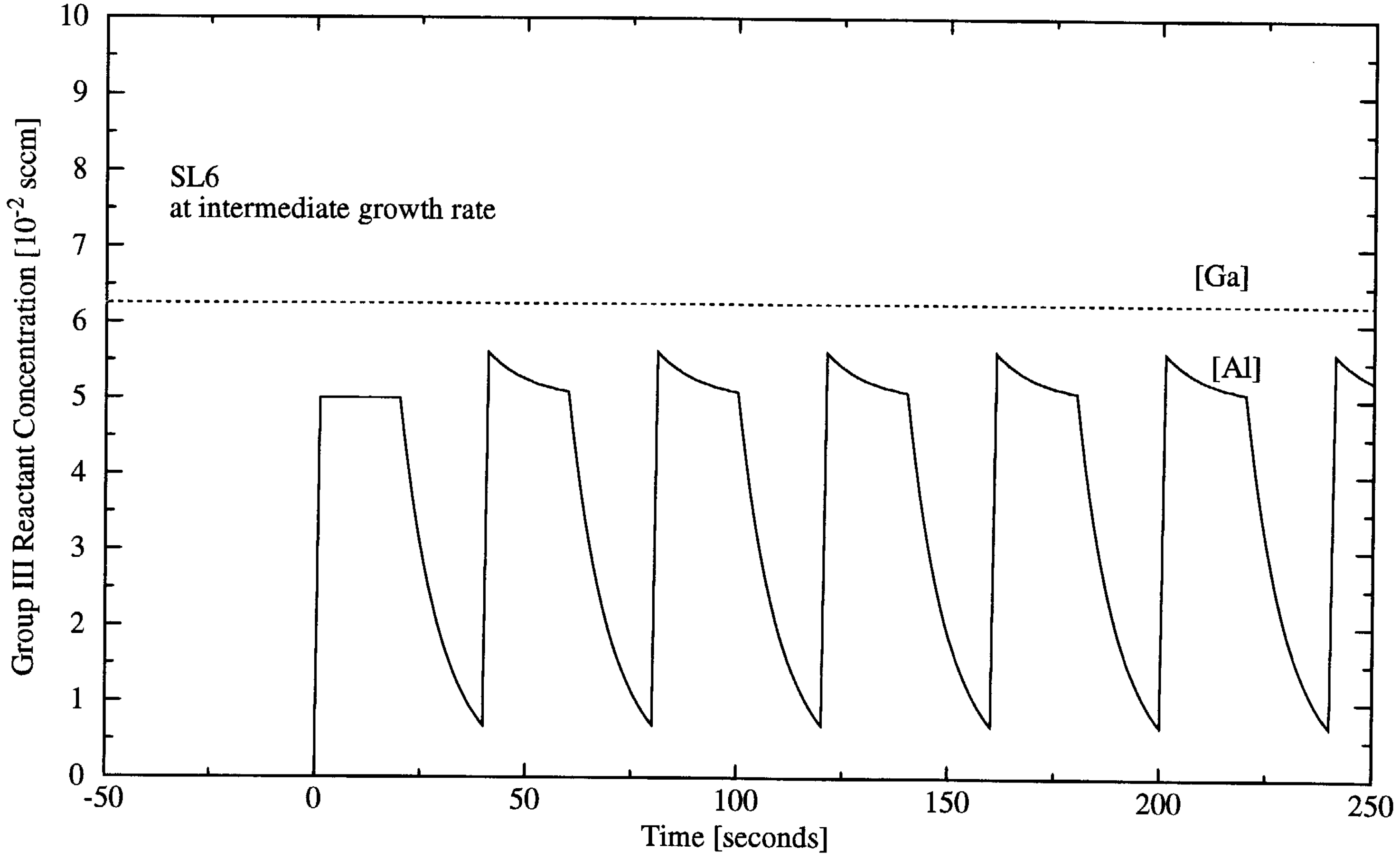

Figure 5-4 (b) Switching Cycle of SL6

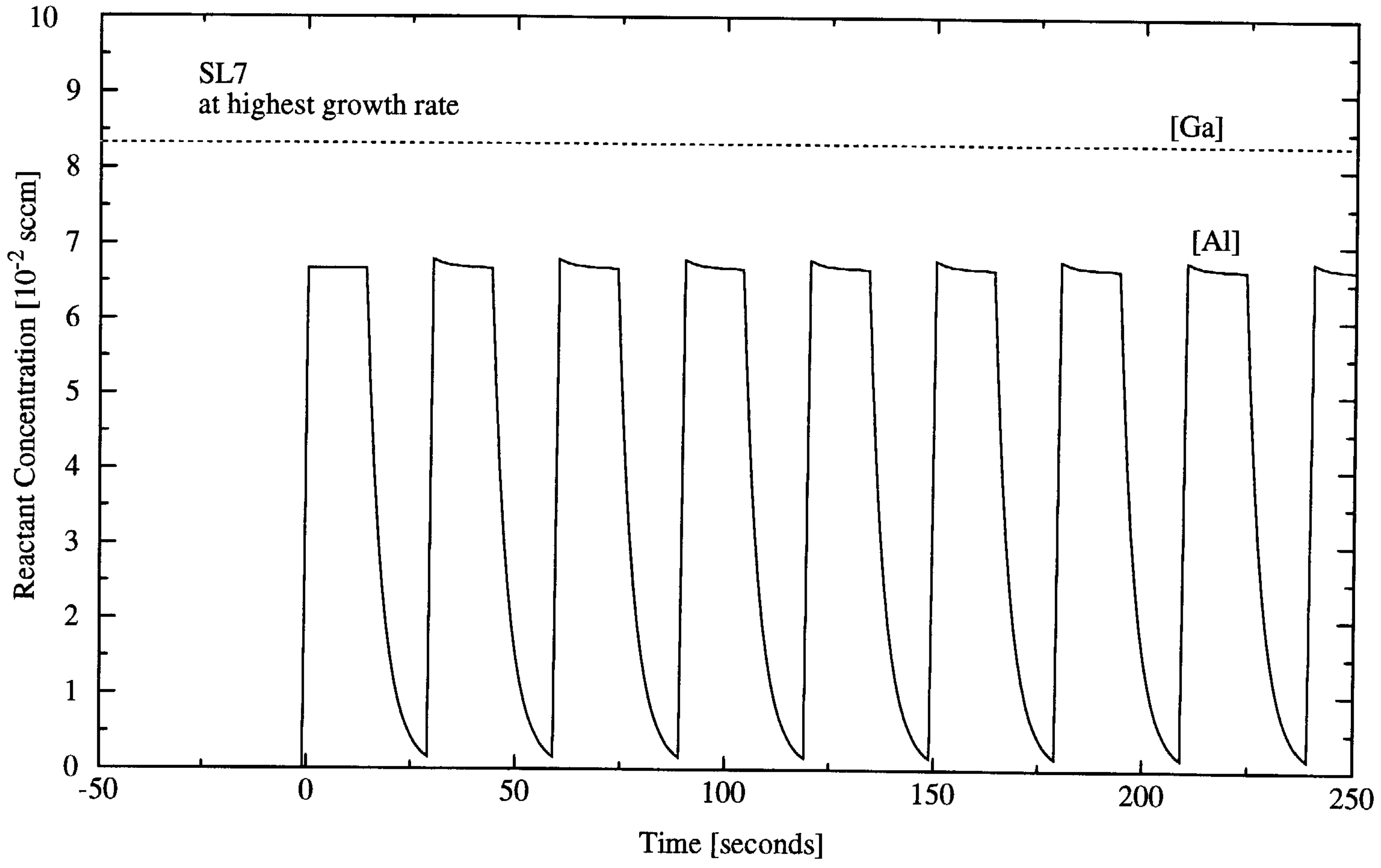

Figure 5-4 (c) Switching Cycle of SL7

dence time of gas species in the reactor chamber is generally assumed to be dependent on total system pressure and flow rate and independent of growth rate in the mass transport limited regime with dilute reactants [18]. The Al concentrations for all growth rates investigated here are dilute relative to total system flow. If this inverse dependence of switching coefficient on growth rate can be reproduced, it may indicate that this reactor geometry operates in a mixed kinetic and mass transport limited regime. When the growth rate is limited by the temperature-dependent rate of reactions on the growing surface, the solid/vapor interface is not depleted of Group III reactants and a reservoir of reactants may exist in the boundary layer. Further investigations at varying growth rates and temperatures are necessary for a convincing explanation of this behavior.

5.1.3 TMGa Switching Coefficient

TMGa flow through the reactor was interrupted only for the growth of SL4. The switching coefficient of TMGa was evaluated for this single sample using a similar approach to that detailed in Section 5.1.2. The switching cycle for interrupted growth with perfectly abrupt concentration pulses is shown in Figure 5-5(a). The switching cycle for concentration pulses with diffusion tails is shown is Figure 5-5(b). The DMAlH pulse is characterized by the switching coefficient determined from SL6, grown at the same growth rate without interruption. For this superlattice there are four integration intervals in which the components contributing to reactant concentration must be determined: 1) the interval of barrier growth, 2) the interval of interruption between AlGaAs and GaAs, 3) the interval of well growth, and 4) the interval of interruption between GaAs and AlGaAs. These intervals constitute one SL period and are designated I, II, III, and IV in Figure 5-5(b).

In interval I, the components contributing to reactant concentration are the steady state DMAlH and TMGa concentrations and an undetermined number of diffusion tails from previous TMGa pulses. There is no component from the previous DMAlH pulse,

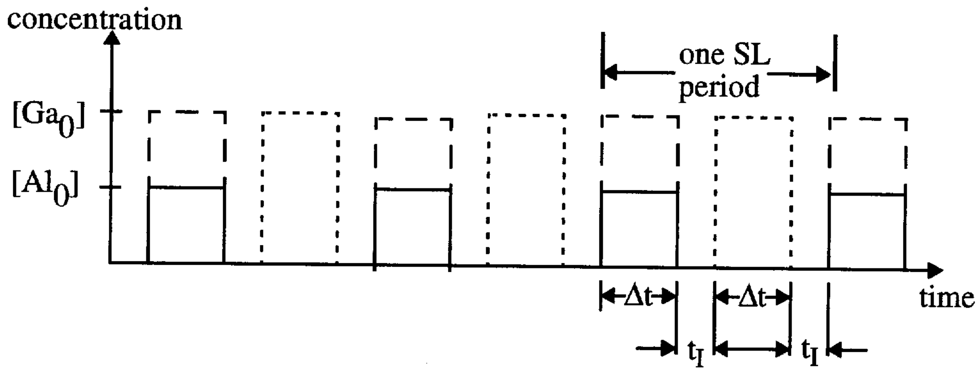

(a) Ideal Switching Cycle of Growth Interrupted SL

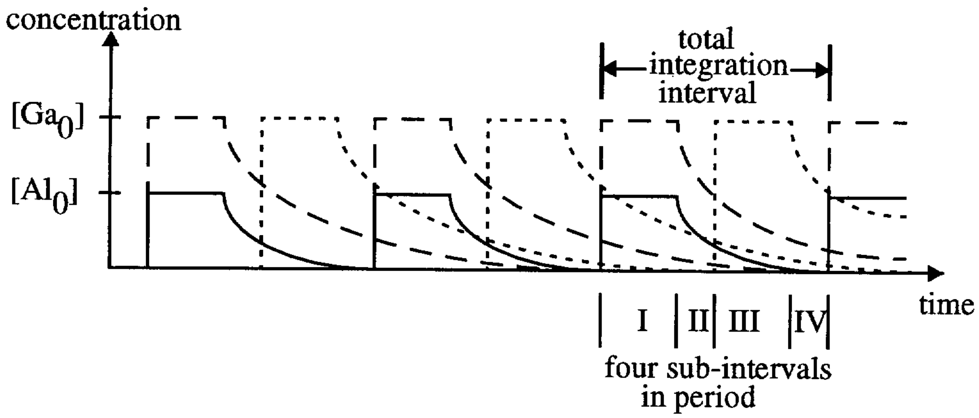

(b) Switching Cycle of Growth Interrupted SL with Diffused Pulses

Figure 5-5 Switching Cycles of Growth Interrupted Superlattice since the DMAlH diffusion coefficient determined for this growth rate in Section 5.1.2, τ_A=10s, results in the magnitude of the previous DMAlH tail being ~1% of steady state at the beginning of interval I, and thus negligible for these calculations.

In interval II, the components are the diffusion tails of the DMAlH and TMGa pulses which have just been switched to vent, and the same undetermined number of diffusion tails from previous TMGa pulses. In interval III, the components are the steady state TMGa concentration, the diffusion tails of the DMAlH and TMGa from the previous barrier, and the undetermined number of diffusion tails from previous TMGa pulses. In interval IV, the components are the diffusion tail of TMGa from the pulse which has just been switched to vent, the DMAlH and TMGa tails from the previous barrier, and the undetermined number of diffusion tails from previous TMGa pulses.

When the growth rate as a function of concentration in these intervals is integrated individually for each integration segment and then summed, the total thickness grown in a single period is obtained. When the steady state terms representing the period as designed are subtracted, an expression for the difference between measured period and designed period results:

$$\Delta p = \tau_A C_A [Al_0]\left(1 - e^{-(\Delta t + 2t_I)/\tau_A}\right) + 2\tau_G C_G [Ga_0]\left(1 - e^{-n(\Delta t + t_I)/\tau_G}\right) \quad \text{Eqn. 5-13}$$

In this equation the number of TMGa pulses from previous periods considered in the solution is represented by n, an integer. The first RHS term in Equation 5-13 can be evaluated explicitly from the results obtained in Section 5.1.2 for the DMAlH switching coefficient at this growth rate. Equation 5-13 can then be evaluated numerically to determine the TMGa switching coefficient τ_G for various numbers of diffusion tails from TMGa pulses in previous periods. The test of the accuracy of a given solution is that $\exp[-n(\Delta t+t_I)/\tau_G]$ be less than 0.01. For n=1, the solution τ_G=15s has an error of exp(-60/15)=0.02. For n=3 the solution is also τ_G=15s, with a reduced error of exp(-90/15)=0.00. This indicates that the diffusion tails of the previous two TMGa pulses must be included as terms of the integrand. Figure 5-6(a) illustrates the concentration pulses of TMGa for τ_G=15s and DMAlH for τ_A=10s during interrupted SL growth at this growth rate. Figure 5-6(b) shows the total reactant concentration in the manifold versus time for these conditions.

It is clear from Figure 5-6(b) that the reactant concentration in the manifold never goes to zero for the growth and interrupt intervals used here. It can therefore be inferred that no actual growth interruption occurred during the growth of this superlattice. As a consequence, several deviations from the structure as designed can be identified. First, an additional layer of $Al_xGa_{1-x}As$ with the mole fraction a decaying exponential is present at the $Al_{0.8}Ga_{0.2}As$ to GaAs interface. Second, during the growth interval of the GaAs well the material grown actually consists of $Al_xGa_{1-x}As$ of low mole fraction, as ternary growth was extended beyond the designed interval. Finally, an additional layer of $Al_xGa_{1-x}As$ of low mole fraction is grown during the GaAs to $Al_{0.8}Ga_{0.2}As$ interrupt interval.

5.1.4 Summary

The total concentration of a switched reactant is either 1) the sum of a steady state value (during reactant to process line intervals) and several diffusion tails from previous pulses, or 2) the sum of several diffusion tails from previous pulses only (during reactant to vent intervals). It is important to note in Figure 5-4 (a), (b), and (c) and in Figure 5-6 (b) that, although the switched reactant concentration is definitely not a square pulse, these sums are a periodic function of time after the first two diffusion tails have accumulated. If the total concentration were not periodic for the majority of SL layers, then the regular periodicity of the superlattice structure would not be produced and no SL satellite peaks would be seen in DCRC measurements. The higher order peaks observed in the rocking curves indicate that SL structures with regular spatial periodicity are present. The deviation of these structures from the original design provides a means of characterizing the concentration in the manifold in order to achieve improved process control.

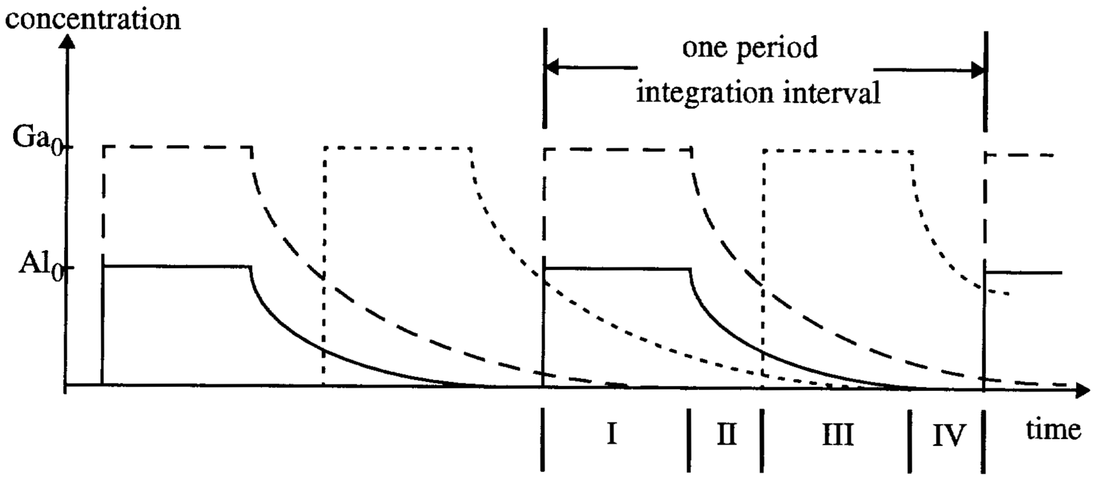

5-6 (a) Concentration Pulses During Interrupted Growth

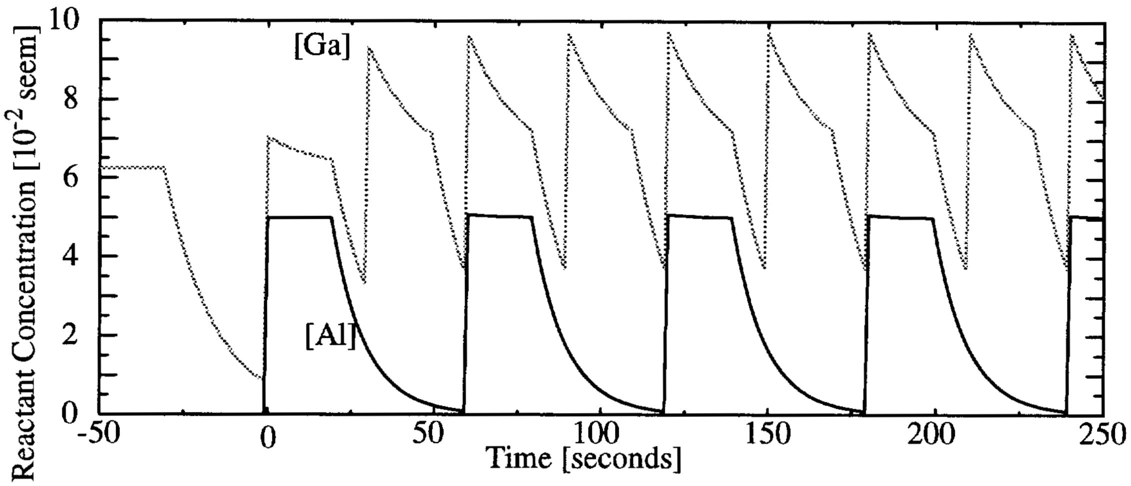

5-6 (b) Total Concentration versus Time During Interrupted Growth

Figure 5-6 Reactant Concentration During Interrupted Growth

5.2 Modeling Bandgap versus Thickness

5.2.1 Superlattice Structures

The deviation of the SL specimens from the dimensions and composition of the structure designed can be analyzed by transforming the total concentration versus time models developed thus far into bandgap versus depth relations.

The thickness of material grown is related to the total reactant concentration as a function of time through Equation 5-2. In the previous sections expressions for the growth rates of AlAs and GaAs as a function of time were developed as a series of terms specified over the sub-intervals of one SL period. In the next stage of modeling, these concentration versus time functions were used as spreadsheet instructions to calculate cumulative thickness at any given time during the growth. The interval δt for each integration step was 1 second. The integration approximation was the forward Euler method, which over-estimated the thickness of material grown by less than 4% during a 1 second interval in which both [Al(t)] and [Ga(t)] were decaying exponentials of the form $[III_0]\, e^{-t/\tau}$, where $[III_0]$ was the steady state reactant concentration. The over-estimate was less than 1% during intervals in which the concentrations were the sum of a steady state value and decaying exponentials.

The mole fraction of Al in the material at any given time was calculated from the ratio of [Al(t)] to [Al(t)]+[Ga(t)] according to the quadratic fit to data obtained in Section 3.2.4 (see Figure 3-7). This relationship, Equation 3-1 on page 36, was:

$$x = 3.36\left(\frac{[Al(t)]}{[Al(t)] + [Ga(t)]}\right) - 2.66\left(\frac{[Al(t)]}{[Al(t)] + [Ga(t)]}\right)^2 \qquad \text{Eqn. 5-14}$$

The mole fraction value at each interval was used to calculate the bandgap of the material grown during that interval. Both the direct (Γ) and indirect (X) bandgaps as a function of composition were calculated for each interval and min[E_Γ, E_X] was set equal to E_{AlGaAs} for bandedge offset calculations. Bandedge offsets were calculated according to the analysis by Kroemer [10], resulting in the expressions $\Delta E_V=0.50x$ eV for $0 \le x \le 1$, $\Delta E_C=0.81x$ eV for $0 \le x \le 0.43$, and $\Delta E_C=(0.43-0.19x)$ eV for $0.43 \le x \le 1.0$.

For the purpose of predicting photoluminescence behavior, all bandgaps were adjusted to their 10K values, as this was the temperature at which PL measurements were obtained. The temperature dependence of E_{GaAs} was taken to be [9]:

$$E_{\Gamma,\,GaAs}(T) = \left(1.519 - \frac{5.408 \cdot 10^4 \cdot T^2}{(T+204)}\right) eV \quad \text{for T in K} \qquad \text{Eqn. 5-15}$$

This resulted in a 10K bandgap for GaAs of $E_{\Gamma,GaAs}=1.516$eV. The 10K bandgap of the X valley was determined graphically from Reference 9 to be $E_{X,GaAs}=2.03$eV. The 10K Γ and X bandgaps for AlAs were also determined graphically from the data quoted in Reference 9, resulting in values of $E_{\Gamma,AlAs}=3.11$eV and $E_{X,AlAs}=2.28$eV. The room temperature bandgap versus mole fraction relation for ternary $Al_xGa_{1-x}As$ was adjusted to the 10K Γ and X endpoints for GaAs and AlAs, resulting in the expressions:

$$E_{\Gamma,\,AlGaAs} = 1.516 + 1.087x + 0.53x^2 \qquad \text{Eqn. 5-16}$$

$$E_{X,\,AlGaAs} = 2.03 + 0.10x + 0.09x^2 \qquad \text{Eqn. 5-17}$$

For every one second time interval the spreadsheet calculation of Equation 5-14 was used to determine the values of x input to Equations 5-16 and 5-17 for that interval. The lesser of the two bandgap values was set equal to E_{AlGaAs} and the band offsets calculated as functions of composition, as described above. The conduction and valence band energies for a given interval were calculated according to $E_C=(\Delta E_C+E_{GaAs})$ and $E_V=-\Delta E_V$, referencing all energies to the GaAs valence band maximum $E_{V,GaAs}=0$. These energy levels were plotted versus the cumulative thickness determined for each interval. The resulting energy band diagrams for the four SLs are shown in Figures 5-7 and 5-8.

The band diagrams calculated from this model showed considerable deviation from the intended SL structure, which was designed to have 225Å $Al_{0.8}Ga_{0.2}As$ barriers

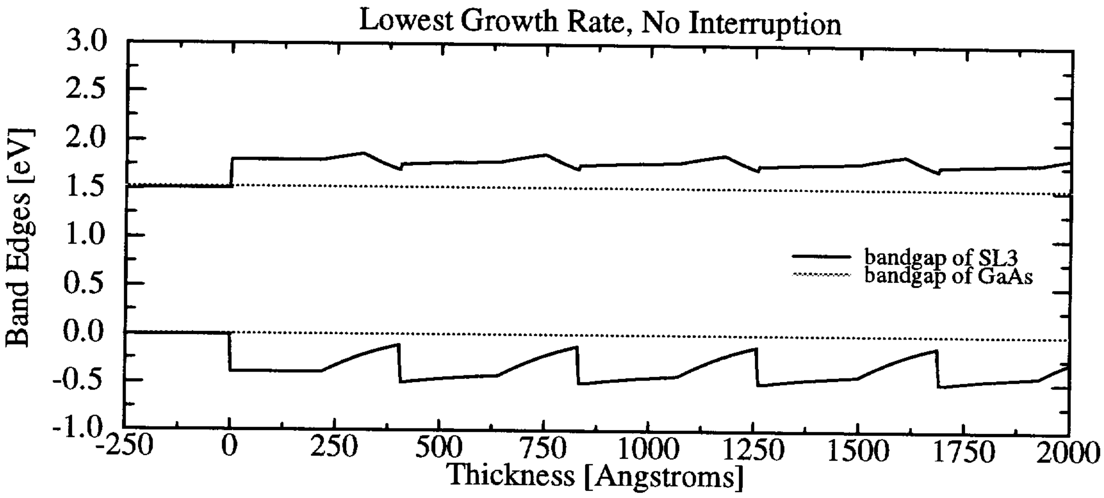

(a) SL3

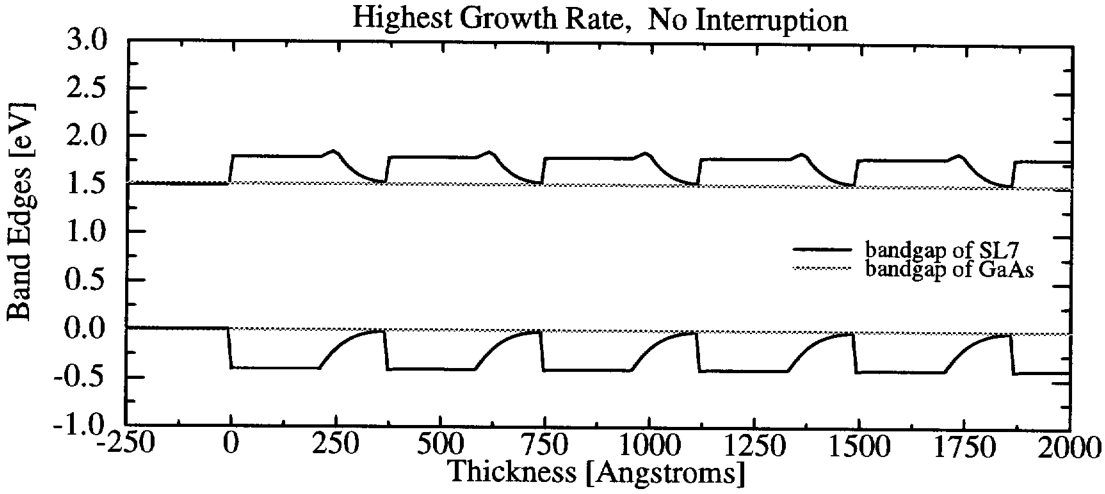

(b) SL7

Figure 5-7 Bandgap of Superlattices SL3 & SL7

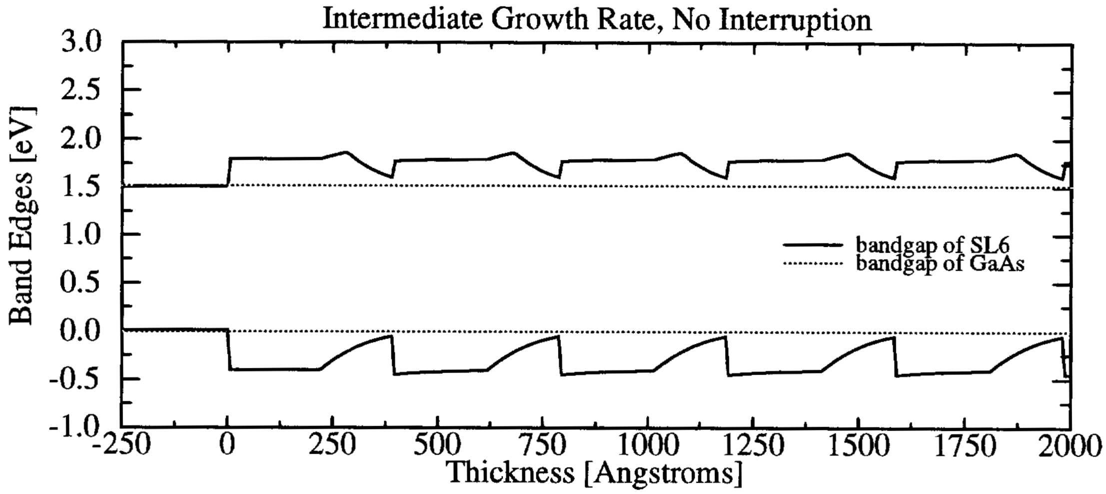

(a) SL6

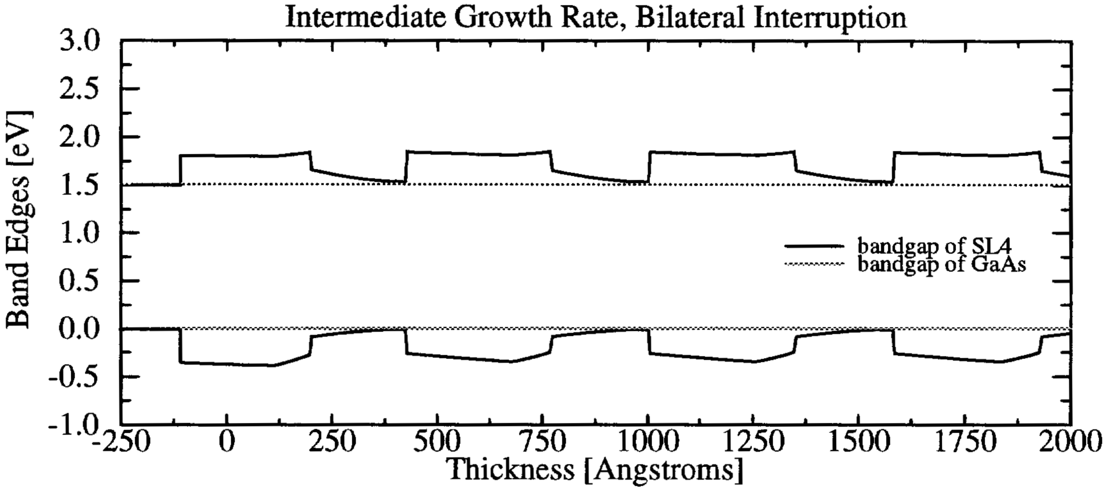

(b) SL4

Figure 5-8 Bandgap of Superlattices SL6 & SL4

and 125Å GaAs square wells. Only the model of the growth interrupted sample, SL4, was composed of approximately square wells of binary GaAs, as shown in Figure 5-8(b). Both the barriers and the wells in the model of this sample were increased in thickness due to the continued growth during the interrupt interval. The barriers were ~300Å thick and the wells ~235Å thick (see Table 4-4 on page 86). The samples grown without interruption at various growth rates all showed approximately triangular wells in the models due to the growth of $Al_xGa_{1-x}As$ during the interval intended for well growth. The model of the sample grown at the lowest rate, SL3 (Figure 5-7(a)), reached a conduction band minimum in the wells at a composition of $Al_{0.25}Ga_{0.75}As$ with an effective well width[1] of 85Å. The model of the sample grown at the highest rate, SL7 (Figure 5-7(b)), reached a conduction band minimum in the wells at $x=0.02$ with an effective well width of 125Å. The model of the sample grown at the intermediate rate, SL6 (Figure 5-8(a)), reached a minimum in the wells at $x=0.10$ with an effective well width of 110Å. These deviations from the SL parameters as designed will change the width and the central energy of the SL energy band and alter the photoluminescence transition energies. These effects will be examined in Section 5.3

5.2.2 Quantum Well Structures

Deviations from the designed structure were also apparent in the models of the growth of the quantum well stacks. The QW bandgap versus thickness models were calculated by the same method as the SL models using the concentration versus time functions derived previously. The bandgap versus thickness diagrams resulting from these calculations are shown in Figure 5-9. All QW samples were grown at the intermediate growth rate due to limitations on source materials.

The model for QW1, grown without interruption, showed wells which were trian-

---

[1] Effective well width was defined as the thickness of the well over which the mole fraction of Al was ≤ 0.43. This is the mole fraction at which the $\Gamma \rightarrow X$ transition occurs in $Al_xGa_{1-x}As$.

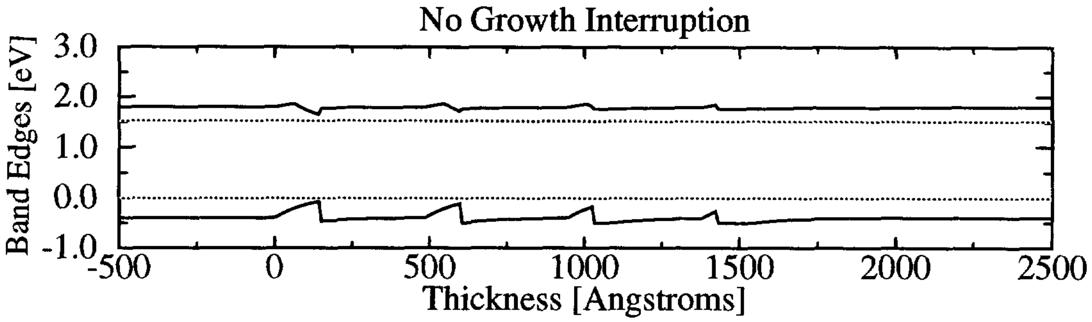

(a) QW1

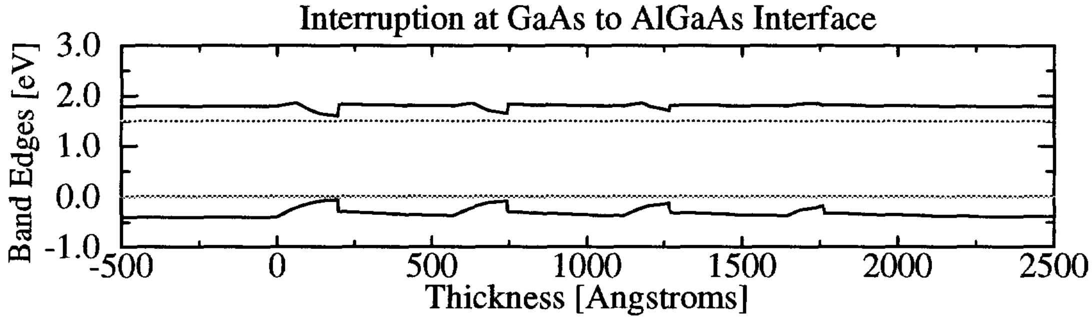

(b) QW3

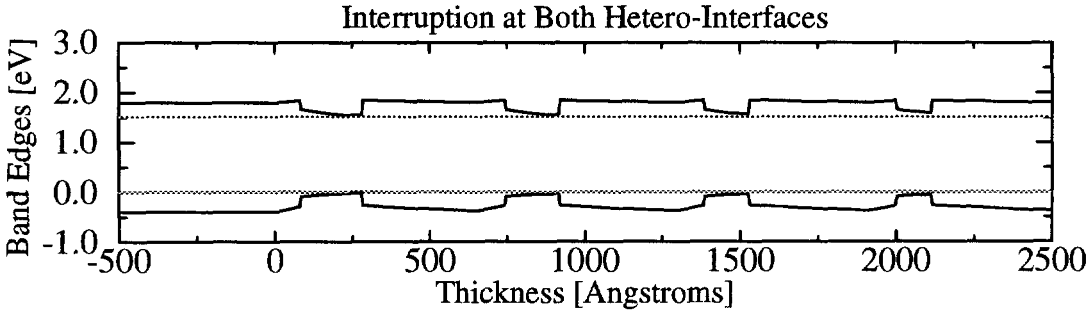

(c) QW2

Figure 5-9 Bandgap of Quantum Well Stacks

gular rather than square, as expected from the growth of $Al_xGa_{1-x}As$ during the well interval. The barrier heights were all reduced from their designed values due to the non-zero Al mole fraction in the well. The effective well widths were also reduced to 80, 50, 20, and 0Å from the designed widths of 100, 75, 50, and 25Å. The narrowest well is considered to be 0Å in width due to the fact that the mole fraction of Al throughout that well was greater than 0.55, which is above the $\Gamma \rightarrow X$ transition for AlGaAs.

The model of QW3, grown with an interrupt at all AlGaAs on GaAs surfaces, also produced approximately triangular wells due to continued growth of $Al_xGa_{1-x}As$ during the interval intended for well growth. The confinement barriers were reduced due to the non-zero Al mole fraction in the wells. The effective widths of the wells in this sample, however, were increased to 135, 120, 90, and 35Å from the designed widths of 100, 75, 50, and 25Å due to the continued growth of GaAs during the GaAs-to-AlGaAs interrupt.

The model of QW2, which was grown with interrupts both at the AlGaAs on GaAs interfaces and at the GaAs on AlGaAs interfaces, produced a bandgap diagram similar to that seen for the bilaterally interrupted superlattice, SL4. The wells in this model were approximately square wells composed of ternary AlGaAs in which $x \leq 0.2$. The effective well widths were increased to 200, 175, 145, and 115Å. This increase is due to the continued growth of low mole fraction AlGaAs during the the GaAs-to-AlGaAs interrupt (as in QW3), and also to the more abrupt drop in Al mole fraction after the AlGaAs-to-GaAs interrupt. During the AlGaAs-to-GaAs interrupt, concentrations of both TMGa and DMAlH fall exponentially, and thus the [Al(t)] to [Al(t)]+[Ga(t)] ratio does not decrease as rapidly as is the case when only the Al concentration is decaying. When the TMGa concentration is increased for well growth, the ratio changes suddenly and the mole fraction of Al is greatly decreased at the beginning of the well interval. This causes more of the well growth at the beginning of the well interval to be within the mole fraction limits $0 \leq x \leq 0.43$.

The deviations in well shape, effective width, and barrier height seen in the quantum well models will result in quantum confined states in the wells which are different from those calculated for the wells as designed. The first confined state was calculated for each well using the well width, barrier height to the Γ valley in the cladding layer, and shape parameters produced by the model. In addition, the SL bands for samples SL4 and SL6 were calculated using the parameters of well width, barrier width, barrier height to the Γ valley in the ternary layer, and well shape produced by the SL models. From these energy level results, photoluminescence wavelengths were tentatively predicted.

5.3 Quantum Well and Superlattice Energy State Calculations

5.3.1 Ideal Square Well Solutions

The first energy state in ideal wells was calculated from the finite square well solution to the electron or heavy hole wave equation [1, 133-135]:

$$E_{1C,V} = V_{C,V} - \left(\frac{m_W^{e,hh}}{m_B^{e,hh}} \cdot E_{1C,V} \cdot \tan^2 \sqrt{\frac{m_W^{e,hh} \cdot E_{1C,V} \cdot L_W^2}{2 \cdot (h/2\pi)^2}} \right) \qquad \text{Eqn. 5-18}$$

$V_{c,v}$ represents the barrier height, ΔE_V in the valence band and $\Delta E_\Gamma = 0.81x$ eV in the conduction band. The conduction band barrier height is calculated from the Γ valley of the well to the Γ valley of the barrier according to the analysis by Kroemer [10]. The effective mass of the electron in bulk GaAs at 10K is $m_{GaAs}^{e} = 0.0667 m_o$ [9]. In a quantum well the effective mass of the electron is a function of the energy level of the particle in the well [135], and is approximated by the cubic relation:

$$m_W^e(E_1) = \left(0.0667 + 0.0436 E_1 + 0.0236 E_1^2 - 0.147 E_1^3 \right) m_o \qquad \text{Eqn. 5-19}$$

The mole fraction dependence of electron effective mass in $Al_xGa_{1-x}As$ was taken to be $m_B^e = (0.0667 + 0.83x)\, m_o$ at 10K [135]. Solutions for the first conduction band energy level were obtained using the ideal parameters (designed well thickness, barrier composition, and conduction band barrier height to the Γ valley in the cladding) in Equations 5-18 and 5-19, which were iterated from E_1=1meV in 1meV steps until the difference in m_W^e was less than 1%. Solutions for valence band energy levels were obtained using the designed well thickness, barrier composition, and valence band barrier height in Equation 5-18 with the heavy hole effective mass parameters $m_W^{hh} = 0.48m_0$ and $m_B^{hh} = (0.48 + 0.31x)\, m_o$ [135]. The photoluminescence transition energy was then calculated as $E_{PL} = E_{1C} + E_{1V} + E_{g,\,GaAs}$. Results for ideal square wells are listed in Table 5-2.

Table 5-2 Transition Energies in Ideal Square Wells

L_W [Å]	E_{1C} [eV]	E_{1V} [eV]	E_{PL} [eV]	λ_{PL} [μm]
25	0.5993	0.1261	2.642	0.4701
50	0.1990	0.0480	2.163	0.5742
75	0.0950	0.0250	2.036	0.6100
100	0.0549	0.0152	1.986	0.6254
125	0.0356	0.0102	1.962	0.6331

5.3.2 Non-Ideal Well Solutions

Two approximations for determining the first energy level in the non-ideal wells described by the model were examined, the triangular well approximation and the asymmetrical square well approximation. The triangular well approximation produced an over-estimate of the first energy level due to the increased confinement in the triangular well compared to that in an exponentially graded well. The asymmetrical square well approximation produced an under-estimate of the first energy level due to the reduced confinement in the square well compared to that in the exponentially graded well. These calculation approximations are compared graphically to the finite square well solution in Figure 5-10.

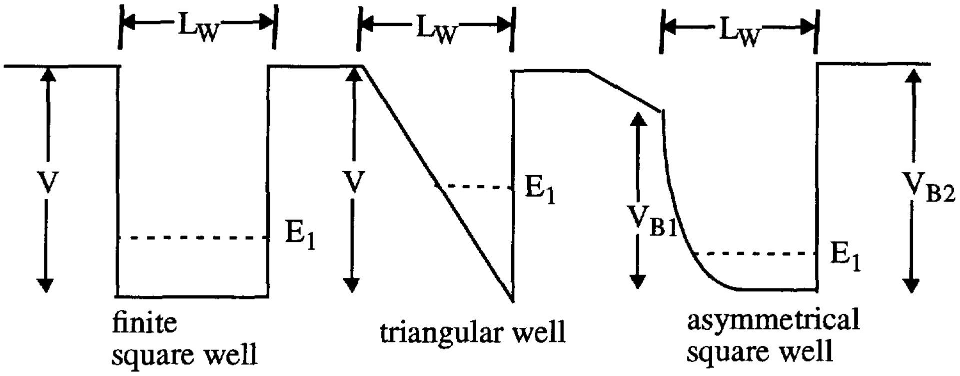

Figure 5-10 Quantum Well Energy Level Approximations

Numeric solutions for an exponentially graded well have been calculated by other workers and compared to the asymmetrical square well solutions [135]. The energy shift was shown to be larger for a narrow well than for a wide well. This shift is negligible for wells wider than 150Å. The magnitude of the shift for wells as narrow as 30Å was shown to be less than 3%, which is within the error in these current calculations. Therefore the asymmetrical square well approximation was considered to be the best approximation for calculating energy levels in the wells described by the model. The asymmetrical square well solution for the first energy level is:

$$E_{1C,V} = \frac{(h/2\pi)^2}{2m_W^{e,hh}(L_W)^2} \cdot \left[\pi - \operatorname{asin}\sqrt{\frac{m_W^{e,hh}E_{1C,V}}{m_{B1}^{e,hh}V_{B1}}} - \operatorname{asin}\sqrt{\frac{m_W^{e,hh}E_{1C,V}}{m_{B2}^{e,hh}V_{B2}}}\right]^2 \qquad \text{Eqn. 5-20}$$

This approximation required six input parameters for calculation of the first energy level in both conduction band and valence band wells: the composition x_{B1} and barrier height V_{B1} of the first confinement layer, the composition x_{B2} and barrier height V_{B2} of the second confinement layer, the composition x_W in the well, and the effective well width L_W. These parameters were determined for both conduction and valence bands from the spreadsheet calculations performed to model bandgap versus thickness using Equations 5-14, 5-16, and 5-17; they are presented in Table 5-3. The effective mass of carriers in the barriers was calculated according to $m_B^e = (0.0667 + 0.83x_B)\,m_o$ and $m_B^{hh} = (0.48 + 0.31x_B)\,m_o$. The effective mass of heavy holes in the well was $m_W^{hh} = (0.48 + 0.31x_W)\,m_o$. The electron effective mass in the well depended on E_1 and required iterative solutions of Equations 5-19 and 5-20 for the conduction band. The results of these calculation are presented in Table 5-4. Predictions which are underlined were observed experimentally.

Brackets in Table 5-4 indicate that the first energy level in the well is above the X valley in the barrier. Under these conditions scattering from the Γ valley in the well to the X valley in the barrier will decrease luminescent efficiency. Energy level solutions for the 20Å well in sample QW1 and for the 35Å well in sample QW3 are above the X valley minimum on the low barrier side of the wells. The transition energies for these wells are bracketed to indicate that the existence of these transitions is unlikely. This is consistent with calculations indicating that the assumption of perfect confinement is not accurate in QWs less than 30Å in thickness [136].

Table 5-3 Calculation Parameters for Asymmetrical Square Wells

Sample	Interrupt	Well #	L_W [Å]	x_W	x_{B1}	$V_{B1,C}$ [eV]	$V_{B1,V}$ [eV]	x_{B2}	$V_{B2,C}$ [eV]	$V_{B2,V}$ [eV]
QW1	none	1	80	0.16	0.43	0.225	0.139	0.95	0.635	0.395
		2	50	0.24	0.43	0.162	0.100	1.00	0.613	0.378
		3	20	0.37	0.43	0.065	0.041	1.00	0.514	0.318
		4	0	>0.43	--	--	--	--	--	--
QW2	bilateral	1	200	0.04	0.43	0.405	0.250	0.52	0.395	0.244
		2	175	0.05	0.43	0.389	0.240	0.52	0.379	0.234
		3	145	0.06	0.43	0.370	0.222	0.52	0.360	0.222
		4	115	0.10	0.43	0.346	0.213	0.52	0.336	0.207
QW3	at AlGaAs on GaAs interface only	1	135	0.12	0.43	0.262	0.162	0.58	0.373	0.230
		2	120	0.17	0.43	0.240	0.148	0.59	0.431	0.210
		3	90	0.25	0.43	0.175	0.108	0.61	0.296	0.183
		4	35	0.37	0.43	0.066	0.040	0.65	0.230	0.141
SL4	bilateral	--	235	0.03	0.43	0.383	0.237	0.52	0.404	0.249
SL6	none	--	110	0.11	0.43	0.273	0.169	0.90	0.640	0.395

Table 5-4 Transition Energies in Asymmetrical Square Wells

Sample	Interrupt	Well #	L_W [Å]	E_{1C} [eV]	E_{1V} [eV]	$E_{g,well}$ [eV]	E_{PL} [Ev]	λ [μm]
QW1	none	1	80	0.024	0.009	1.728	1.761	0.7053
		2	50	0.039	0.018	1.835	1.892	0.6564
		3	20	[0.065]	0.035	1.994	[2.094]	[0.5931]
		4	0	--	--	--	--	--
QW2	bilateral	1	200	0.009	0.002	1.563	1.574	0.7891
		2	175	0.010	0.002	1.582	1.594	0.7892
		3	145	0.014	0.003	1.610	1.627	0.7634
		4	115	0.016	0.005	1.646	1.667	0.7451
QW3	at AlGaAs on GaAs interface only	1	135	0.011	0.003	1.668	1.682	0.7384
		2	120	0.011	0.004	1.736	1.751	0.7093
		3	90	0.013	0.006	1.841	1.860	0.6677
		4	35	[0.036]	0.021	1.997	[2.054]	[0.6047]
SL4	bilateral	--	235	0.007	0.001	1.548	1.556	0.7982
SL6	none	--	110	0.017	0.005	1.660	1.682	0.7384

At 10K, kT/q is about 0.9meV. Energy levels in valence band wells within 2-3 kT/q (~2meV) of the valence band maximum are an indication that the width of the valence band well has reached the maximum limit for quantum confinement. Valence band energy levels in these wide wells can be approximated by the valence band maximum.

5.4 Predictions from the Band Models

The quantum well energy level results are based on the bandgap model which is itself an approximation. Therefore the prediction of photoluminescence behavior must be qualitative only.

Photoluminescence (PL) from the sample QW1 is predicted to occur from a maximum of two wells, the 80Å well and the 50Å well. Poor confinement in the 20Å well is expected to reduce luminescent efficiency from that well. In the well designated as having zero thickness, the material at the bottom of the well is indirect $Al_{0.55}Ga_{0.45}As$ for which no PL is expected. The PL transition energies for this sample are tentatively predicted to be in the range 1.75 to 1.90 eV.

The concentration model indicated that neither QW2 nor QW3 was actually growth-interrupted. However, according to the model calculations the material growth during the nominal interrupt intervals was slowed. Slower growth rates are also associated with increased incorporation of contaminants due to the decreased competition for lattice sites with Group III elements [85].

PL from sample QW2 is expected from all four wells, in the energy range 1.57 to 1.67 eV. However, this sample was growth interrupted (or growth slowed), which has been shown to increase the incorporation of contaminants at the interrupted surface [137]. These contaminants act as recombination centers, thus decreasing luminescent efficiency of the wells. PL intensity from this sample may be affected by the incorporation of contaminants.

PL from sample QW3 is expected from only three wells. Poor confinement in the 35Å well is expected to result in the absence of luminescence from this well. PL transition energies from the other wells are expected to be in the range 1.68 to 1.86 eV. As this sample was interrupted (or slowed) at the GaAs-to-AlGaAs interface, PL intensity may be decreased.

In SL4, the growth-interrupted superlattice, the center of the luminescence band is within 3kT/q of the conduction band, indicating that the wells in this SL specimen are near the maximum width for quantum confinement. Therefore a distinct SL band in the PL spectrum may not be observed. Luminescence from this sample should occur near the band-to-band energy in the wells, ~1.56 eV. Bilateral growth interruptions are expected to reduce luminescent efficiency in this specimen.

PL in a band centered around 1.68 eV is predicted from SL6. As this sample was grown without interrupts, no decrease in PL intensity due to the incorporation of contaminants is expected.

Chapter 6

Photoluminescence Measurements

6.1 Theory of Photoluminescence

Luminescence is the emission of optical radiation as a result of electronic excitation of a material. Photoluminescence is defined as luminescence in which the excitation source is optical radiation [138]. The optical excitation results in a non-equilibrium state in the semiconductor. The excess population of electron-hole pairs generated by the input radiation may recombine in a radiative process in which the energy difference between the two states is emitted as electromagnetic radiation [139]. A wavelength scan of emitted radiation constitutes the photoluminescence spectrum. The transition from an upper to a lower energy state may also proceed via one or more intermediate states which may or may not be radiative.

The intrinsic transitions of the material occur at or near the band edges. These intrinsic transitions include radiative recombination of free excitons, radiative recombination of excitons bound to shallow impurities, and band-to-band recombination of electrons and holes which are not associated in excitonic pairs. Band-to-band transitions may be direct (radiative) or indirect (non-radiative). In addition to the intrinsic transitions of the material, impurities provide intermediate states through which carriers may recombine. Recombination paths via impurities are defined as extrinsic transitions. Extrinsic transition include shallow transitions to neutralize ionized donors or acceptors, deep transitions from the conduction band to an acceptor state or from a donor state to the valence band, transitions to deep levels within the bandgap, and donor-to-acceptor transitions [139].

The radiative transition processes are in competition with the non-radiative processes for the excess population of carriers. The radiative efficiency η_q is the fraction of the excited carriers that recombine radiatively to total radiative and non-radiative recombination, and may be written in terms of the carrier lifetimes as

$$\eta_q = \frac{R_r}{R_r + R_{nr}} = \frac{\tau_{nr}}{\tau_{nr} + \tau_r} \qquad \text{Eqn. 6-1}$$

where $R_{r,nr}$ are the radiative (r) and non-radiative (nr) recombination rates and $\tau_{r,nr}$ are the radiative and non-radiative lifetimes. If the number of carriers participating in radiative transitions is small compared to the number undergoing non-radiative transitions, luminescent efficiency will be low [138]. Radiative efficiency is increased at lower temperatures due to the increase in carrier lifetime for non-radiative transitions at low temperatures. PL measurements taken at lower temperatures thus have the advantage of increased luminescent efficiency.

In bulk materials, PL transition energies provide information on bandgap energy and excitonic binding energy, and the PL linewidth and luminescent efficiency are measures of crystal quality and purity [138, 139]. PL measurements on quantum-size structures provide additional information on the nature of the heterointerfaces [140].

6.2 PL on Quantum-Size Structures

The linewidth and peak splitting of PL transitions from QWs are sensitive to the structure of the interfaces between the layers [140, 141], and the intensity is related to the material quality (Section 6.1). This sensitivity to interfaces can be used to study the growth process and determine appropriate process control adjustments.

6.2.1 Energy Shift of PL in Quantum Wells

Due to the confinement of carriers, the PL transition energy is shifted to higher energies as the well thickness is decreased [137]. The initial energy state for the band-to-band transition is the first quantized energy level in the conduction band well, and the final energy state is the first quantized energy level in the valence band well. However, because of the increase in exciton binding energy due to spatial confinement [136], exciton recombination plays a more signatificant role in QWs than in bulk crystals [137, 141]. It has been shown that exciton localization in QWs dominates PL at low temperatures (T<50K), although the low temperature PL lineshape indicates the presence of some free carrier recombination [141]. Excitonic transitions are expected at energies below the band-to band transition by the amount of the excitonic binding energy. PL emission from quantum wells has consequently been described as an excitonic probe of the QW which is sensitive to structural variations on the order of the exciton diameter [3, 76, 86], approximately 150-200Å.

An additional shift in the emission energy is observed in QWs with graded or interdiffused interfaces [87, 143-144]. When the barrier-to-well interface is not abrupt, the well is effectively thinner than a well grown for the same duration but having abrupt interfaces, as demonstrated by the calculations in Section 5.3.2. This decrease in effective width causes an increase in the first energy level in the well and a shift to higher energies of PL emission from the well.

6.2.2 Evaluating Interface Roughness

Luminescence lines in QWs are broadened due to interface roughness, alloy disorder, the thermal distribution of carriers, and free carrier effects [137]. The principle broadening mechanism at low temperatures is the two-dimensional roughness composed of interface roughness and alloy disorder [60]. The full width half maxima (FWHM) of PL spectra obtained at low temperature are narrower than those obtained at higher temperatures due to the decreased contributions of the thermal distribution and free carrier effects [141]. Broadening due to alloy disorder scattering is not affected by temperature [77]. The other component of the 2D roughness, atomic scale roughness parallel to the interface, is related to the FWHM of the low temperature emission line by

$$\Delta L_W = \Delta(h\nu)\left(\frac{4\mu_0 L_W^3}{h^2}\right) \qquad \text{Eqn. 6-2}$$

where ΔL_W is the uncertainty in the nominal well width L_W, $\Delta(h\nu)$ is the FWHM of the PL emission, and μ_0 is the reduced mass of the exciton [137]. In addition to broadening the emission line, any departure from the ideal well width which has a lateral extent on the order of the exciton will result in a discrete emission line. Figure 6-1 illustrates the effect of fluctuations in well width over a range of lengths.

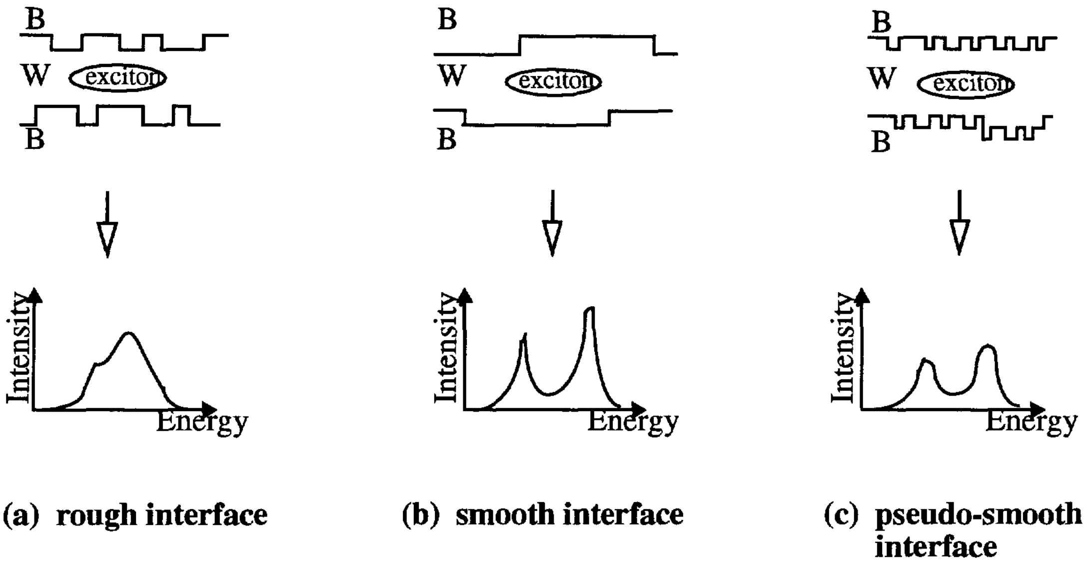

(a) rough interface (b) smooth interface (c) pseudo-smooth interface

Figure 6-1 The Effect of Well Width Fluctuations on PL

Because of its sensitivity to the length scale of roughness parallel to the interface, photoluminescence is suitable for the evaluation of the characteristic length of the in-plane roughness at QW interfaces [6]. A rough interface, as in Figure 6-1(a), has interface roughness with a lateral correlation length on the order of 100Å. The excitonic transition is broadened by the random variation in well width over which the exciton extends. The smooth interface in Figure 6-1(b) has a lateral correlation length greater than or equal to the exciton diameter. In this case, the exciton may occupy one of several areas of uniform width, resulting in distinct PL energies. In the pseudo-smooth interface of Figure 6-1(c) the lateral correlation length is 50Å or less and the exciton no longer sees the variation in well width, but rather an average well width over its spatial extent. The pseudo-smooth interface also produces distinct PL lines corresponding to the average well widths sampled by the exciton, but in this case the peaks are broadened by atomic scale roughness [6].

In the GaAs/AlGaAs system the character of the interface depends critically on the order of material growth, GaAs on AlGaAs or AlGaAs on GaAs [85, 145]. This dependence on growth order will be discussed in detail in Section 6.3.

6.3 Normal and Inverted Surfaces in QW Structures

The model for the growth of GaAs and AlGaAs with V:III ratios greater than one involves the surface migration of the Ga or Al atoms leading to the formation of monolayer high islands at the growing surface [2-3, 22]. The lateral extent of these islands depends on the migration length of the cations [86]. It is generally believed that the migration length of Al is smaller than that of Ga on the epitaxial surface of GaAs/AlGaAs compounds because of the stronger Al-As bond compared to the Ga-As bond [61, 145-146]. This leads to larger island sizes of approximately 100-200Å for GaAs and smaller island sizes of 40Å or less for $Al_xGa_{1-x}As$ when $x>0.5$ [82]. Thus the growth of AlGaAs on GaAs begins on the smoother GaAs surface and the growth of GaAs on AlGaAs begins on the rougher AlGaAs surface. These heterointerfaces are designated normal (AlGaAs on GaAs) and inverted (GaAs on AlGaAs) [85]. Various techniques for smoothing normal (GaAs) and inverted (AlGaAs) surfaces prior to growth of the next layer have been investigated, including growth interruption at interfaces [3, 61, 65, 82, 86, 145-147], temperature switching schemes [146], atomic layer epitaxy [55], migration enhanced epitaxy [56], flow rate modulation [57], and growth rate modulation [62]. The most easily realized technique in conventional MBE and MOCVD is growth interruption at the heterointerfaces, which has been extensively studied.

6.3.1 The Effect of Growth Interruption

The analytical technique of reflection high energy electron diffraction (RHEED) used in the high vacuum environment of molecular beam epitaxy has shown that the GaAs surface becomes smoother during an interruption in growth [80-81]. This smoothing is attributed to the increase in migration time during which the Ga cations may move on the surface to find energetically favorable positions at step edges. Interrupt time for optimum smoothing depends on the Ga migration length at the given substrate temperature. Interrupt intervals longer than the time required for the cations to move a distance equal to the average Ga migration length do not result in additional smoothing. Optimum interrupt intervals vary from 10 to 20 seconds at MOCVD substrate temperatures (650-750°C) to 60-100 seconds at MBE substrate temperatures (500-650°C) [65, 82-84]. This smoothing of the normal interface results in a narrower PL linewidth due to decreased interface scattering [2-3, 76] and excitonic peak splitting due to the lateral extent of steps becoming larger than the exciton diameter [76, 82, 86, 137]. The roughness of the normal surface without growth interruption is illustrated in Figure 6-2(a). Figures 6-2(b) and (c) show the effect of growth interruption on the normal surface and on both surfaces, respectively.

RHEED studies have also indicated that no smoothing of the $Al_xGa_{1-x}As$ surface for $x>0.5$ takes place during interrupt intervals as long as 300 seconds at MBE substrate

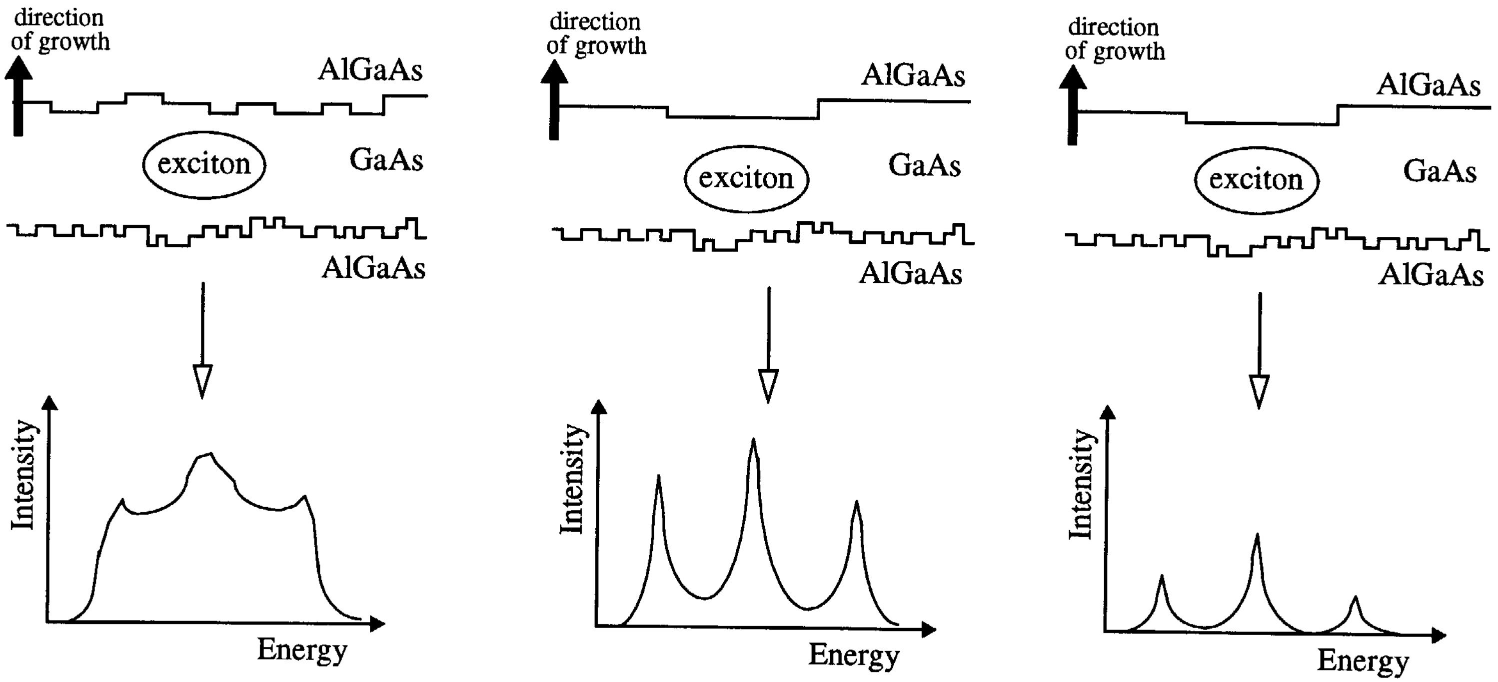

(a) No Growth Interrupt

(b) Interrupt at Normal Interface

(c) Bilateral Interrupts

Figure 6-2 Effect of Growth Interrupt on Normal & Inverted Interfaces temperatures [85-87]. It is inferred from these observations that the Al migration length is so short that additional migration time does not enhance Al migration to step edges. This results in the rougher surface of $Al_xGa_{1-x}As$ for x>0.5. PL investigations of MOCVD-grown GaAs/AlGaAs QWs show no linewidth narrowing and no peak splitting when growth is interrupted only at the inverted surface for intervals as long as 90 seconds [65, 84, 88-90]. It is generally accepted that the inverted surface cannot be smoothed in MBE or MOCVD by growth interruption alone. The invariance of the inverted surface is shown in Figure 6-2(b) and (c).

6.3.2 Trap Incorporation at Normal and Inverted Surfaces

Growth interruption at the heterointerfaces of QWs has been observed to produce a rapid deterioration of the total luminescent efficiency when the interrupt exceeds 30 seconds [2]. This breakdown of luminescent efficiency has been correlated to an enhanced incorporation of deep non-radiative centers during the interrupt interval, and to an increase in the concentration of shallow and moderately deep radiative centers [85]. Systematic investigations of the effect of growth interrupts on normal and inverted interfaces, taken separately, have shown that growth interruption at the normal surface produces smoothing of the interface, an increase in shallow impurities which results in an increase in extrinsic PL intensity, and no appreciable increase in non-radiative traps [58, 85, 149]. Growth interruption at the inverted surface, on the other hand, has been shown to produce no smoothing of the interface, a strong increase in shallow impurities and the associated increase in extrinsic PL intensity, and a marked increase in the concentration of non-radiative recombination centers which quenches the luminescence [85]. This behavior is attributed to the relatively greater reactivity of Al as compared to Ga [85, 149].

Thus growth interruption at either interface increases the incorporation of neutral acceptors (mainly carbon) at the interrupted interface, resulting in a low-energy tail or a discrete low-energy peak in the PL spectrum due to the transition from the first level in the conduction band well to the shallow acceptor [58]. Growth interruption at inverted interfaces increases the incorporation of deep traps and reduces the integrated PL intensity. Consequently, an optimum interrupt interval at the normal interface only will produce the desirable combination of smooth interfaces without degradation of PL efficiency. Growth interruption at the inverted interface will produce an increase in non-radiative recombination centers and the degradation of PL efficiency.

For the purpose of observing these effects in the current investigation, one quantum well stack sample was grown with no interrupt (QW1), another was grown with interrupts at both the normal and inverted interfaces (QW2), and the final sample was grown with an interrupt at the normal interface only (QW3). Although the model of switching transients developed from the DCRC data indicated that no complete interruption in epitaxial growth occured in these samples, the growth rate did decrease during the interrupt interval. It is expected that this decrease in growth rate allowed an increase in impurity incorporation during the intended interrupt interval [85].

6.4 Obtaining Photoluminescence Measurements

6.4.1 The PL System

Steady state photoluminescence spectra were taken with the samples mounted on the cold finger in a variable-temperature cryostat cooled to 9.5K. For optical pumping, the 5145Å line of an Ar-ion laser was used operating CW with an output power of 0.5W. The focused excitation spot size on the sample was estimated to be 150-200μm in diameter. Excitation power at the sample surface was measured with and without an attenuator in the beam, resulting in excitation densities on the sample of 250mW/cm^2 without attenuation and 20mW/cm^2 with attenuation. The resulting PL emission from the sample was focused on the 5mm entry slit of a 0.5m spectrometer with a spectral resolution of 5Å. Radiation passing through the spectrometer was detected by a LN_2-cooled Ge PIN diode detector. The spectrometer scan and data collection were computer controlled. Each QW sample was scanned in two sections. The short wavelength range from 0.6000 to 0.8000 µm was scanned without beam attentuation in order to obtain maximum PL intensity in the range of expected QW emission. The longer wavelength range from 0.8000 to 0.8600 was scanned with the attenuator in the excitation beam in order to prevent saturation of the detector from the strong intensity of the GaAs substrate emission. PL spectra were also obtained on the intermediate growth rate SLs with (SL4) and without (SL6) growth interruption using the same two-section scan method.

6.4.2 PL Data

PL spectra on samples QW1, QW2, and QW3 are presented in Figure 6-3. The strong luminescence peak at 1.513 eV in all samples is consistent with the 10K excitonic transition in the GaAs substrate and buffer layer. This peak is invariant in energy and FWHM (~5 meV) in all three QW stacks. The broader peak at approximately 1.490 eV in all samples is consistent with exciton to neutral acceptor transitions for carbon impurities, which lie 0.026 eV above the valence band edge in GaAs [88, 138, 149]. The relative intensity of this peak indicates a high concentration of unintentional carbon dopants from the metalorganic Group III sources [65, 89]. In the spectrum of QW3, with a growth interrupt at the normal interface only, this exciton to carbon peak shows the distinctive low energy tail which is characteristic of increased incorporation of shallow impurities during the growth interrupt interval [58]. In the spectrum of QW2, with growth interrupts at both normal and inverted interfaces, the exciton to carbon peak shows an unexpected high energy shoulder which may be due to an increase in carbon doping sufficient to produce a band of impurity states [89].

In the sample with bilateral interrupts there is no emission from any transition

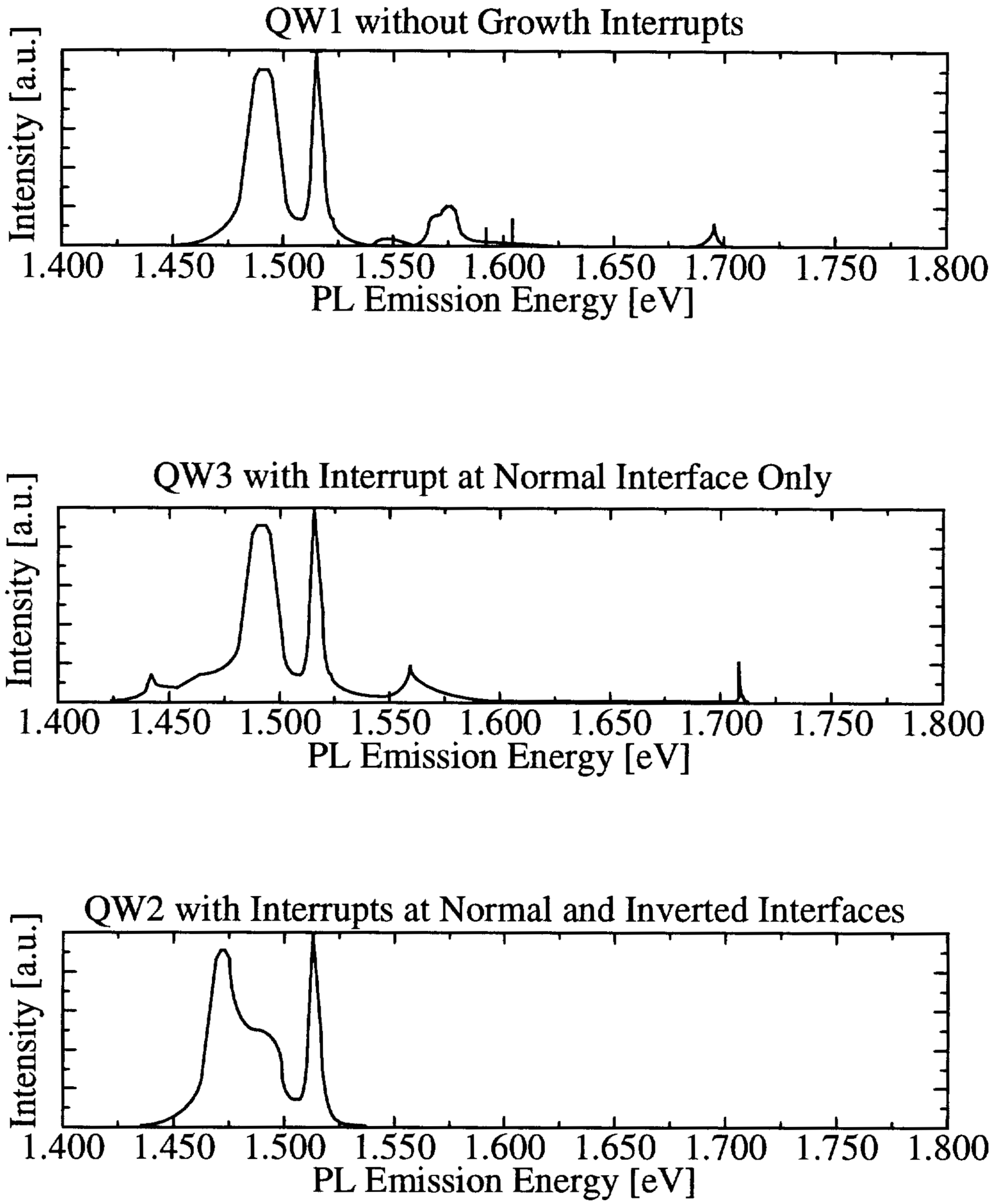

Figure 6-3 PL Spectra on QWs With and Without Interrupts

higher than the GaAs substrate and buffer. This is presumably due to the large increase in deep level traps associated with the interrupt on the AlGaAs surface, which is known to degrade luminescent efficiency. In both the uninterrupted sample and the sample interrupted at the normal interface only, there is a weak emission line near 1.695 eV and 1.710 Ev, respectively. QW transitions in the range 1.67 to 1.73 eV were predicted from the model for wells on the order of 100Å thick. The stronger peak at 1.575 and 1.560 eV, respectively, in these samples was not predicted by the model. It is lower in transition energy than predicted for the widest wells. It is possible that this represents a transition from a bound exciton (BE) associated with an inhomogeneity in a QW (rather than with an impurity) to a neutral carbon acceptor state [150]. This speculation is supported by the observation that the FWHM of the transition is decreased by growth interruption, implying that the transition is associated with the GaAs surface of a QW. However, in the absence of a series of PL lines which can be reliably associated with individual QWs, it is not possible to evaluate the accuracy of the bandedge model developed in Chapter 5.

The luminescence spectra of SL4 with bilateral interrupts and SL6 without interrupts are presented in Figure 6-4. The emission line from the excitonic transition in the GaAs substrate and buffer is present at 1.513 eV in both samples. FWHM of this peak is 3 meV in the uninterrupted sample and 5 meV in the interrupted sample. The lower energy peak near 1.490 eV from the exciton to neutral carbon transition is also present in both spectra. In SL4, with bilateral growth interrupts, the exciton to carbon peak merges into the GaAs substrate/buffer peak as a low energy shoulder, indicating that carbon doping in this sample is approaching degenerate levels and forming a continuous band of states [150]. Weak emission from the SL band is present in both samples. The interrupted sample shows weak SL emission at 1.544 eV, in good agreement with E_{PL} predicted by the model. The uninterrupted sample shows weak SL emission at 1.605 eV, substantially below E_{PL} of 1.682 predicted by the model. The characteristic broadening of the SL emission band is not visible in either specimen.

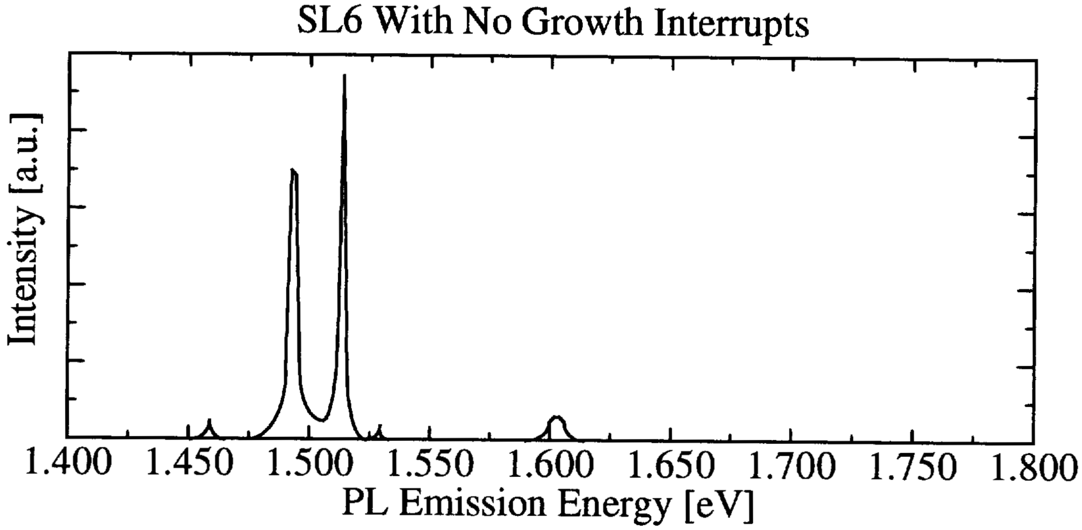

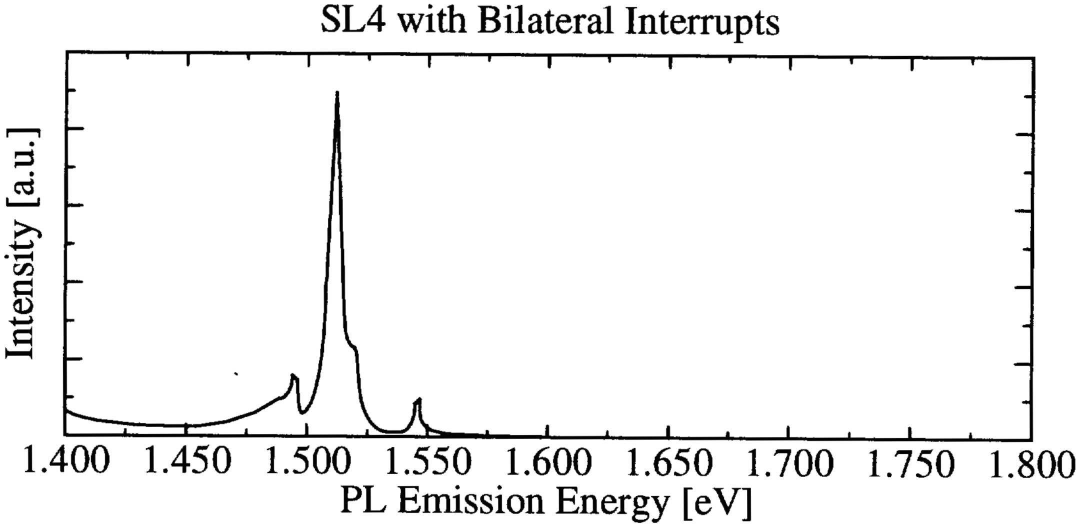

Figure 6-4 PL Spectra on SLs With and Without Interrupts

6.5 Conclusions from PL Data

The two major residual impurities in GaAs and AlGaAs are carbon and oxygen [151]. Carbon contamination of epitaxial GaAs is known to be a problem when TMGa is used as the Ga precursor, and can be reduced by the use of tri-ethyl gallium (TEGa) [18]. Carbon contamination is more severe in AlAs and AlGaAs layers due to the strong Al-C bond [151]. The use of DMAlH as an aluminum source, while reducing oxygen contamination in the highly sensitive AlGaAs layers, is also known to increase carrier compensation due to high levels of carbon incorporation [74-75]. In addition, the incorporation of residual carbon impurities is enhanced at the higher substrate temperatures required for the growth of AlAs and AlGaAs [151].

The 10K luminescence peak seen at 1.495 eV has been identified as the exciton to neutral carbon acceptor (e-C_{As}) transition of the GaAs buffer layer [135]. It is seen in virtually all MOCVD-grown GaAs/AlGaAs material due to the large quantity of CH_3 radicals produced at the growing surface by the pyrolysis of the metalorganic sources. The relative intensity of this PL peak is a qualitative measure of carbon contamination in the material. The PL data presented here indicate a high level of carbon contamination in the material grown for this investigation. Carbon contamination in the samples which were interrupted at the AlGaAs surface was observed to increase and form a low energy shoulder on the GaAs substrate peak. This indicates that unintentional carbon doping approaches degenerate levels when growth is interrupted at the AlGaAs surface.

The other major impurity, oxygen, forms a deep level trap in GaAs and AlGaAs. Oxygen doping studies in GaAs have indicated that when a few ppm of O_2 are added to the gas stream, less than $10^{16}cm^{-3}$ of O is incorporated into the solid [152]. Photoluminescence efficiency and electron mobility are not greatly affected by this level of oxygen contamination in GaAs. For AlGaAs, however, studies have shown that 1 ppm of O_2 in the vapor results in $10^{20}cm^{-3}$ of O in the solid [152]. This amount is enough to adversely affect the PL efficiency, as the deep level oxygen traps are non-radiative recombination centers. It is also sufficient to produce semi-insulating material due to free carrier trapping and decreased carrier lifetimes. The sources of oxygen contamination in MOCVD are leaks into the system, desorption from walls, outgassing from the susceptor, and as an impurity in the source materials (particularly AsH_3).

Strong peaks from the excitonic transition in the GaAs substrate and buffer are present in all samples, as are peaks due to GaAs buffer layer exciton to acceptor transitions. Deep trap quenching of luminescence therefore does not occur in epitaxial GaAs grown in the IV-MOCVD system. For epitaxial AlGaAs, on the other hand, the data indicate severe degradation of PL efficiency. The absence of photoluminescence peaks which can be unambiguously associated with transitions in quantum wells implies that PL efficiency in the well stack is low in all samples regardless of growth interruption. These observations lead to the conclusion that PL efficiency has been seriously degraded by oxygen contamination of Al-containing layers in the QW stacks. The PL spectrum of QW2, showing no luminescence signal at all above the GaAs exciton transition, implies that the incorporation of oxygen is enhanced during the growth interrupt (or slowdown) interval on the AlGaAs surface. Clearly the oxygen contamination problem must be addressed before optical or electrical quality AlGaAs can be grown in the IV-MOCVD system.

Chapter 7

Conclusions

7.1 Effectiveness of Fast-Switch Manifold

Rocking curve data indicated that superlattice layers grown in this investigation were substantially thicker than those designed using the steady state growth rates of GaAs and AlGaAs. Since the superlattice growth procedure involved multiple switching events, this implied that switching transients made a significant contribution to the growth of material. The transients for TMGa and DMAlH were individually characterized by switching constants to account for the difference in layer thickness in the superlattices as grown compared to that in the SLs as designed. There was an apparent inverse relationship between growth rate and switching coefficient which will require confirmation and further investigation. Due to the mass flow controller constraints and the limitations of manual switching accuracy, the growth rates of SL layers in this system are limited to a range in which the switching transients for the Group III sources are 4 to 30 seconds.

Two suggested approaches to decreasing interdiffusion of reactants in the gas stream and improving the effectiveness of the fast-switch manifold are (1) moving the switching point in the manifold closer to the reactor chamber inlet in order to decrease transport time in the manifold, and (2) converting to a computer controlled manifold in order to achieve accurate switching at higher growth rates. The first approach has been attempted by other workers in horizontal MOCVD systems without substantial improvement in junction abruptness [153]. However, gas flow dynamics are significantly different in the IV-MOCVD system and minimizing the distance over which interdiffusion takes place may result in some improvement in abruptness in this system. Conversion to a computer controlled manifold would allow accurate growth of SL layers at increased rates. This would result in an improvement of layer abruptness if interdiffusion does indeed decrease as the growth rate increases, as indicated by this preliminary work.

7.2 Effectiveness of Growth Interruption

Growth interruption had three main effects in this system. First, additional layer thicknesses were grown during the interrupt intervals due to the switching transient, resulting in further deviation from the geometry of the structure as designed. Second, an interrupt at the GaAs surface produced a smoother interface, as shown by the decrease in FWHM of PL emission from quantum wells. Third, an interrupt at the AlGaAs surface resulted in a drastic reduction of PL efficiency due to the incorporation of deep level traps during the interrupt (or slowdown) interval. In order to make use of the growth interrupt technique in this system, it will be necessary to avoid interrupts at AlGaAs surfaces entirely and to design structures accommodating the additional layer growth during the interrupt at the GaAs surface.

7.3 Source and System Cleanliness

High concentrations of residual carbon acceptors in all material grown for this investigation are attributed to the metalorganic source materials TMGa and DMAlH. For GaAs growth at temperatures appropriate for the growth of high quality AlGaAs, carbon contamination from the TMGa source is always high [70]. The use of tri-ethyl gallium (TEGa) has been shown to greatly decrease carbon incorporation in GaAs layers [72].

Changing the Ga source to TEGa would result in a reduction of residual carbon and a decrease in the compensation of the material. The DMAlH aluminum source used here also results in high levels of carbon incorporation. However, DMAlH has the important advantage of substantially reducing the incorporation of oxygen in AlGaAs layers compared to other metalorganic Al sources [72]. Since no alternate source of aluminum which simultaneously eliminates carbon and oxygen contamination is currently available, the use of DMAlH remains optimum.

Photoluminescence data demonstrated that oxygen contamination was a severe problem in the IV-MOCVD system. The sources of this contaminant in the system must be eliminated or reduced in order to grow high quality Al-containing compounds. This process includes use of highest purity AsH_3, as this gas is known to be a source of oxygen contamination [151]. It will also be necessary to improve the leak-tight integrity of the reactor assembly and the handling of the susceptor and quartz reactor chamber. A hydrogen anneal for the reactor chamber would eliminate much of the oxygen desorption from the chamber walls.

7.4 Suggestions for Further Work

Several system improvements are suggested before further crystal growth is performed in this system. First, a thorough cleanup of system and sources should be done, including changing the Ga source to TEGa, using the highest purity AsH_3, and arranging for a hydrogen anneal of the quartzware between growth runs. Additional system improvements should include moving the manifold switching point closer to the reactor inlet and converting manifold switching to computer control.

Once these source and instrumentation improvements have been made, the effectiveness of the cleanup process can be evaluated by growing $Al_xGa_{1-x}As$ in the direct bandgap range ($0<x\leq0.43$) for photoluminescence measurements. Reasonable lumines-

cence intensities from direct bandgap AlGaAs would indicate that the oxygen contamination problem had been adequately addressed. Until this can be accomplished, further work on this system is not recommended.

After the sources of oxygen contamination have been reduced, additional system dynamics investigations are suggested. Experiments in which substrate temperature, V:III ratio, and total system flow are individually varied will provide additional information on the rate limiting mechanism and on the relative magnitude of pyrolysis effects in the IV-MOCVD system.

Finally, additional superlattice investigations are suggested. Growth of SLs with shorter periods and increased growth rates will be possible with computer controlled switching. This set of experiments will be useful in confirming the inverse relationship of switching coefficient to growth rate. If the results of the system cleanup are favorable, SLs grown with variable interrupt intervals on the GaAs surface would provide more accurate information on switching coefficients in the manifold. These investigations are necessary before optimum growth parameters and system conditions can be determined.

References

[1] C. Weisbuch and B. Vinter, *Quantum Semiconductor Structures*, Academic Press Inc. (1991).

[2] D. Bimberg, F. Heinrichsdorff, R.K. Bauer, D. Gerthsen, D. Stenkamp, D.E. Mars and J.N. Miller, Binary AlAs/GaAs versus ternary GaAlAs/GaAs interfaces: A dramatic difference of perfection, *J. Vac. Sci. Technol.B* **10** (4), 1793 (1992).

[3] M. Tanaka, T. Noda and H. Sakaki, Atomic-scale characterization and control of semiconductor interfaces grown by molecular beam epitaxy: interface roughness and optical and electronic properties, *Materials Science and Engineering* **B14**, 304 (1992).

[4] M.A.G. Halliwell, M.H. Lyons and M.J. Hill, The interpretation of x-ray rocking curves from III-V semiconductor device structures, *J. Cryst. Growth* **68**, 523 (1984).

[5] W.J. Bartels, J. Hornstra and D.J.W. Lobeek, X-ray diffraction of multilayers and superlattices, *Acta Cryst.* **A42**, 539 (1986).

[6] E. Chason, C.M. Falco, A. Ourmazd, E.F. Schubert, J.M. Slaughter and R.S. Williams, Interface roughness: What is it and how is it measured?, *Mat. Res. Soc. Symp. Proc.: Evolution of Surface and Thin Film Microstructure,* **280**, 203 (1993).

[7] B.K. Tanner, A.G. Turnbull, C.R. Stanley, A.H. Kean and M. McElhinney, Measurement of aluminum concentration in epitaxial layers of $Al_xGa_{1-x}As$ on GaAs by double axis x-ray diffractometry, *Appl. Phys. Lett.* **59** (18), 2272 (1991).

[8] S.N.G. Chu, A.T. Macrander, K.E. Strege and W.D. Johnston, Jr., Misfit stress in InGaAs/InP heteroepitaxial structures grown by vapor-phase epitaxy, *J. Appl. Phys.* **57** (2), 249 (1985).

[9] O. Madelung, (ed.), *Semiconductors: Group IV Elements and III-V Compounds,* Data in Science and Technology Series, Springer-Verlag (1991).

[10] H. Kroemer, Band offsets at heterointerfaces: Theoretical basis and review of recent experimental work, *Surf. Sci.* **174**, 299 (1986).

[11] Y.C.A. Shih and B.G. Streetman, Photoluminescence of AlAs/GaAs superlattice quantum wells, *Appl. Phys. Lett.* **62** (21), 2655 (1993).

[12] N.J. Pulsford, Electronic structure and electrical characterisation of semiconductor heterostructures, *Physics and Technology of Semiconductor Quantum Devices*, K.H. Ploog and L. Tapfer (eds.), Lecture Notes in Physics Series, Springer-Verlag (1993).

[13] B.J. Streetman, *Solid State Electronic Devices*, Prentice-Hall Inc. (1980).

[14] N. Zhu, R. Li, J. Chen and S. Xu, Determination of interface coherency by x-ray double-crystal diffraction, *J. Appl. Phys.* **75** (6), 2805 (1994).

[15] J. Hornstra and W.J. Bartels, Determination of the lattice constant of epitaxial layers of III-V compounds, *J. Cryst. Growth* **44**, 513 (1978).

[16] M. Fatemi and R.E. Stahlbuch, X-ray rocking curve measurement of composition and strain in Si-Ge buffer layers grown on Si substrates, *Appl. Phys. Lett.* **58** (8), 825 (1991).

[17] I.C. Bassignana, D.A. Macquistan and A.J. Spring-Thorpe, Problems in the use of epitaxial AlAs layers as calibration standards for the Al content of AlGaAs/GaAs layers, *Inst. Phys. Conf. Ser.: GaAs and Related Compounds,* **120** (5), 247 (1991).

[18] G.B. Stringfellow, *Organometallic Vapor-Phase Epitaxy: Theory and Practice*, Academic Press, Inc. (1989).

[19] A.Y. Cho and J.R. Arthur, Molecular beam epitaxy, *Prog. Solid State Chem.* **10**, 157 (1975).

[20] W.T. Tsang, *Semiconductors and Semimetals* **22**, Academic Press (1985).

[21] C.R. Abernathy, A.S. Jordan, S.J. Pearton and W.S. Hobson, Growth of high quality AlGaAs by metalorganic molecular beam epitaxy using trimethylamine alane, *Appl. Phys. Lett.* **56** (26), 2654 (1990).

[22] K.H. Ploog, Epitaxial growth of nanostructured III-V semiconductors, *Physics and Technology of Semiconductor Quantum Devices,* K.H. Ploog and L. Tapfer (eds.), Lecture Notes in Physics Series, Springer-Verlag (1993).

[23] H.M. Manasevit, Reflecting on metalorganic chemical vapor deposition (MOCVD), *J. Cryst. Growth* **55**, 1 (1981).

[24] G.B. Stringfellow, Fundamentals of thin film growth, *J. Cryst. Growth* **137**, 212 (1994).

[25] A. Sherman, Modeling of chemical vapor deposition reactors, *J. Elec. Mater.* **17** (5), 413 (1988).

[26] L.J. Giling, Principles of flow behavior: Applications to CVD-reactors, *Crystal Growth of Electronic Materials*, E. Kaldis (ed.), Elsevier Science Publisher (1985).

[27] M.J. Ludowise, Metalorganic chemical vapor deposition of III-V semiconductors, *J. Appl. Phys.* **58** (8), R31 (1985).

[28] J. Korec and M. Heyen, Modeling of chemical vapor deposition, *J. Cryst. Growth* **60**, 286 (1982).

[29] J. Van de Ven, G.M.J. Rutten, M.J. Raaijmakers and L.J. Giling, Gas phase depletion and flow dynamics in horizontal MOCVD reactors, *J. Cryst. Growth* **76**, 352 (1986).

[30] H. Moffat and K.F. Jensen, Complex flow phenomena in MOCVD Reactors, *J. Cryst. Growth* **77**, 108 (1986).

[31] L.J. Giling, Gas flow patterns in horizontal epitaxial reactor cells observed by interference holography, *J. Electrochem. Soc.* **192**, 634 (1982).

[32] I.O. Clark, A.L. Fripp and W.A. Jesse, MOCVD manifold switching effects on growth and characterization, *J. Cryst. Growth* **109**, 246 (1991).

[33] J.S. Roberts, N.J. Mason and M. Robinson, Factors influencing doping control and abrupt metalllurgical transitions during atmospheric pressure MOVPE growth of AlGaAs and GaAs, *J. Cryst. Growth* **68**, 422 (1984).

[34] A. Ishibashi, Y. Mori, M. Itabashi and N. Watanabe, Optical properties of $(AlAs)_n(GaAs)_n$ superlattices grown by metalorganic chemical vapor deposition, *J. Appl. Phys.* **58**, 2691 (1985).

[35] B.I. Miller, E.F. Schubert, U. Koren, A. Ourmazd, A.H. Dayem and R.J. Capik, High quality narrow GaInAs/InP quantum wells grown by atmospheric organometallic vapor phase epitaxy, *Appl. Phys. Lett.* **49**, 1384 (1986).

[36] D.I. Fotiadis, A.M. Kremer, D.R. McKenna and K.F. Jensen, Complex flow phenomena in vertical MOCVD reactors: Effects on deposition uniformity and interface abruptness, *J. Cryst. Growth* **85**, 154, (1987).

[37] N.S. Raghavan, W. Montasser, R.S. Timsit, R.L. Adams and E.J. Fjarlie, Gas flow in a vertical MOCVD reactor, *Inst. Phys. Conf. Ser.: GaAs and Related Compounds,* **106**, 75 (1989).

[38] M. Kondo, A. Kuramata, T. Fujii, C. Anayama, J. Okazaki, H. Sekiguchi, T. Tanahashi, S. Yamazaki and K. Nakajima, An approach to versatile highly-uniform MOVPE growth: The flow controlled stagnation point flow reactor, *J. Cryst. Growth* **124**, 265 (1992).

[39] P.N. Gadgil, Single wafer processing in stagnation point flow CVD reactor: Prospects, constraints and reactor design, *J. Elec. Mater.* **22** (2), 171 (1993).

[40] C.A. Wang, S. Patnaik, J.W. Caunt and R.A. Brown, Growth characteristics of a vertical rotating-disk OMVPE reactor, *J. Cryst. Growth* **93**, 228 (1988).

[41] N. Kobayashi, T. Fukui and K. Tsubaki, Selectively-doped GaAs/n-AlGaAs heterostructures grown by MOCVD, *Jap. J. Appl. Phys.***23** (9), 1176 (1984).

[42] M.R. Leys, C. Van Opdorp, M.P.A. Viegers and H.J. Talen-van der Mheen, Growth of multiple thin layer structures in the GaAs-AlAs system using a novel VPE reactor, *J. Cryst. Growth* **68**, 431 (1984).

[43] W.L. Holstein, Modeling of chimney CVD reactors, *J. Cryst. Growth* **125**, 311 (1992).

[44] C. Houtman, D.B. Graves and K.F. Jensen, CVD in stagnation point flow, *J. Electrochem. Soc.* **133** (5), 961 (1986).

[45] P. Lee, D. McKenna, D. Kapur and K.F. Jensen, MOCVD in inverted stagnation point flow, *J. Cryst. Growth* **77**, 120 (1986).

[46] A.H. Dilawari and J. Szekely, A mathematical representation of a modified stagnation flow reactor for MOCVD applications, *J. Cryst. Growth* **108**, 491 (1991).

[47] J.D. Parsons, Inverted-vertical OMVPE reactor: Design and characterization, *J. Cryst. Growth* **116**, 387 (1992).

[48] J.D. Parsons, U.S. Patent No. 4,732,110 (1988).

[49] J.D. Parsons, K. Oatis, J. Wu, A.K. Chaddha, S.R. Hahn, H-S. Chen, S. Wild and C. Deng, Growth of undoped indium phosphide by OMVPE in an inverted-vertical reactor using trimethylindium and tertiarybutylphosphine and phosphine, *J. Electrochem. Soc.* **140** (11), 3280 (1993).

[50] C.H. Chen, D.S. Cao and G.B. Stringfellow, Use of tertiarybutylphosphine for the growth of InP and $GaAs_{1-x}P_x$, *J. Elec. Mater.* **17** (1), 67 (1988).

[51] Y. Monteil, R. Favre, P. Raffin, J. Bouix, M. Vaille and P. Gibart, Raman investigations on AsH_3 decomposition in MOVPE, *J. Cryst. Growth* **93**, 159 (1988).

[52] R. Lückerath, P. Tommack, A. Hertling, H.J. Koss, P. Balk, K.F. Jensen and W. Richter, CARS *in situ* diagnostics in MOVPE: The thermal decomposition of AsH_3 and PH_3, *J. Cryst. Growth* **93**, 151 (1988).

[53] P. Abraham, A. Bekkaoui, V. Soulière, J. Bouix and Y. Monteil, Thermal decomposition studies of group V hydrides, *J. Cryst. Growth* **107**, 26 (1991).

[54] J.D. Parsons, A.T. Hunter and D.C. Reynolds, Characterization of high purity, p-type GaAs grown at atmospheric pressure by MOVPE, *Inst. Phys. Conf. Ser.: GaAs and Related Compounds,* **79**, 211 (1985).

[55] D. Bertone, Atomic layer epitaxy of InP, *J. Elec. Mater.* **21** (3), 265 (1992).

[56] Y. Horikoshi and M. Kawashima, Migration-enhanced epitaxy of GaAs and AlGaAs, *J. Cryst. Growth* **95**, 17 (1989).

[57] N. Kobayashi, T. Makimoto, Y. Yamauchi and Y. Horikoshi, Flow-rate modulation epitaxy of GaAs and AlGaAs, *J. Appl. Phys.* **66** (2), 640 (1989).

[58] C.W. Tu, R.C. Miller, B.A. Wilson, P.M. Petroff, T.D. Harris, R.F. Kopf, S.K. Sputz and M.G. Lamont, Properties of (Al,Ga)As/GaAs heterostructures grown by molecular beam epitaxy with growth interruption, *J. Cryst. Growth* **81**, 159 (1987).

[59] T.Y. Wang, A.W. Kimball, G.S. Chen, D. Birkedal and G.B. Stringfellow, GaInP/AlGaInP strained quantum wells grown using atmospheric pressure organometallic vapor phase epitaxy, *J. Cryst. Growth* **109**, 285 (1991).

[60] J. Singh, K.K. Bajaj and S. Chaudhuri, Theory of photoluminescence line shape due to interfacial quality in quantum well structures, *Appl. Phys. Lett.* **44** (8), 805 (1984).

[61] M. Tanaka, H. Sakaki, J. Yoshino and T. Furuta, Photoluminescence and absorption linewidth of extremely flat GaAs-AlAs quantum wells prepared by molecular beam epitaxy including interrupted deposition for atomic layer smoothing, *Surf. Sci.* **174**, 65 (1986).

[62] C. Maierhofer, S. Munnix, D. Bimberg, R.K. Bauer, D.E. Mars and J.N. Miller, Reduction of trap concentration and interface roughness of GaAs/AlGaAs quantum wells by low growth rates in molecular beam epitaxy, *Appl. Phys. Lett.* **55** (1), 50 (1989).

[63] D.J. Wolford, G.D. Gilliland, T.F. Kuech, J.F. Klem, H.P. Hjalmarson, J.A. Bradley, C.F. Tsang and J. Martinsen, Comparison of transport, recombination, and interfacial quality in molecular beam epitaxy and organometallic vapor-phase epitaxy GaAs/$Al_xGa_{1-x}As$ structures, *Appl. Phys. Lett.* **64** (11), 1416 (1994).

[64] M. Razeghi, F. Omnes, J. Nagle, M. Defour, O. Acher and P. Bove, High-purity GaAs layers grown by low-pressure metalorganic chemical vapor deposition, *Appl. Phys. Lett.* **55** (16), 1677 (1989).

[65] R.D. Dupuis, J.G. Neff and C.J. Pinzone, Very smooth AlGaAs-GaAs quantum wells grown by metalorganic chemical vapor deposition, *J. Cryst. Growth* **124**, 558 (1992).

[66] G.H. Olsen and M. Ettenberg, Universal stain/etchant for interfaces in III-V compounds, *J. Appl. Phys.* **45** (11), 5112 (1974).

[67] S.B. Phatak and G. Kelner, Material-selective chemical etching in the system InGaAsP/InP, *J. Electochem. Soc.* **126** (2), 287 (1979).

[68] H. Kräutle, H. Roehle, A. Escobosa and H. Beneking, Investigation on low temperature MO-CVD growth of GaAs, *J. Elec. Mater.* **12** (1), 215 (1983).

[69] D.H. Reep and S.K. Ghandhi, Electronic properties of organometallic chemical vapor deposited GaAs epitaxial layers, *J. Electrochem. Soc.* **131** (11), 2697 (1984).

[70] P.D. Dapkus, H.M. Manasevit, K.L. Hess, T.S. Low and G.E. Stillman, Electronic transport in ultrathin heterostructures, *J. Cryst. Growth* **55**, 10 (1981).

[71] M.J. Tsai, M.M. Tashima and R.L. Moon, The effects of the growth temperature on $Al_xGa_{1-x}As$ ($0 \leq x \leq 0.37$) LED materials grown by OM-VPE, *J. Elec. Mater.* **13**, 437 (1984).

[72] A.C. Jones, Metalorganic precursors for vapour phase epitaxy, *J. Cryst. Growth* **129**, 728 (1993).

[73] G.E. Coates, M.L.H. Green and K. Wade, *Organometallic Compounds*, Methuen & Co. Ltd. (1987).

[74] R. Bhat, M.A. Koza, C.C. Chang and S.A. Schwarz, The growth and characterization of AlGaAs using dimethyl aluminum hydride, *J. Cryst. Growth* **77**, 7 (1986).

[75] A.C. Jones, P.J. Wright, P.E. Oliver, B. Cockayne and J.S. Roberts, Growth of $Al_xGa_{1-x}As$ by MOVPE using alternative alkylaluminium *[sic]* precursors, *J. Cryst. Growth* **100**, 395 (1990).

[76] T. Hayakawa, T. Suyama, K. Takahashi, M. Kondo, S. Yamamoto, S. Yano and T. Hijikata, Interface disorder in GaAs/AlGaAs quantum wells grown by molecular beam epitaxy at high substrate temperature, *Appl. Phys. Lett.* **47** (9), 952 (1985).

[77] S.B. Ogale, A. Madhukar, F. Voillot, M. Thomsen, W.C. Tang, T.C. Lee, J.Y. Kim and P. Chen, Atomistic nature of heterointerfaces in III-V semiconductor-based quantum-well structures and its consequences for photoluminescence behavior, *Phys. Rev. B* **36** (3), 1662 (1987).

[78] M.A. Herman, D. and J. Christen, Heterointerfaces in quantum wells and epitaxial growth processes: Evaluation by luminescence techniques, *J. Appl. Phys.* **70** (2), R1 (1991).

[79] X. Wang, H. Zheng, T. Yu and R. Laiho, Study on interface roughness in GaAs/AlGaAs single quantum wells, *Superlattices and Microstructures* **12** (3), 359 (1992).

[80] A. Madhukar, T.C. Lee, M.Y. Yen, P. Chen, J.Y. Kim, S.V. Ghaisas and P.G. Newman, Role of surface kinetics and interrupted growth during molecular beam epitaxial growth of normal and inverted GaAs/AlGaAs(100) interfaces: A reflection high-energy electron diffraction intensity dynamics study, *Appl. Phys. Lett.* **46** (12), 1148 (1985).

[81] S. Clarke, D.D. Vedensky and M.W. Ricketts, Influence of surface morphology upon recovery kinetics during interrupted epitaxial growth, *J. Cryst. Growth* **95**, 28 (1989).

[82] M. Tanaka and H. Sakaki, Atomistic models of interface structures of GaAs-$Al_xGa_{1-x}As$(x=0.2-1) quantum wells grown by interrupted and uninterrupted MBE, *J. Cryst. Growth* **81**, 153 (1987).

[83] S. Koshiba, S. Nanao, O. Tsuda, Y. Watanabe, Y. Sakurai, H. Sakaki, H. Kawata and M. Ando, Effects of growth interruption on structure of MBE grown GaAs/AlAs hetero-interfaces studied by x-ray diffraction, *J. Cryst. Growth* **95**, 51 (1989).

[84] G. Landgren, J. Wallin and S. Pellegrino, Optimal growth interrupts for very high quality InGaAs(P)/InP superlattices grown by MOVPE, *J. Elec. Mater.* **21** (1), 105 (1992).

[85] R. Köhrbrück, S. Munnix, D. Bimberg, D.E. Mars and J.N. Miller, Inequivalence of normal and inverted interfaces of molecular-beam epitaxy grown AlGaAs/GaAs quantum wells, *J. Vac. Sci. Technol. B* **8** (4), 798 (1990).

[86] D. Gammon, B.V. Shanabrook and D.W. Katzer, Interfaces in GaAs/AlAs quantum well structures, *Appl. Phys. Lett.* **57** (25), 2710 (1990).

[87] R.F. Kopf, E.F. Schubert, T.D. Harris and R.S. Becker, Photoluminescence of GaAs quantum wells grown by molecular beam epitaxy with growth interruptions, *Appl. Phys. Lett.* **58** (6), 631 (1991).

[88] J.R. Shealy, C.F. Schaus and L.F. Eastman, Photoluminescence of OMVPE grown AlGaAs: The effect of composition, doping and the substrate, *J. Cryst. Growth* **68**, 305 (1984).

[89] Z.H. Lu, M.C. Hanna, D.M. Szmyd, E.G. Oh and A. Majerfeld, Determination of donor and acceptor densities in high-purity GaAs from photoluminescence analysis, *Appl. Phys. Lett.* **56** (2), 177 (1990).

[90] W.J. Bartels, Characterization of thin layers on perfect crystals with a multipurpose high resolution x-ray diffractometer, *J. Vac. Sci. Technol. B* **1** (2), 338 (1983).

[91] P.F. Fewster and C.J. Curling, Composition and lattice-mismatch measurement of thin semiconductor layers by x-ray diffraction, *J. Appl. Phys.* **62** (10), 4154 (1987).

[92] L. Tapfer and K. Ploog, Improved assessment of structural properties of $Al_xGa_{1-x}As$/GaAs heterostructures and superlattices by double-crystal x-ray diffraction, *Phys. Rev. B* **33** (8), 5565 (1986).

[93] M.J. Hill, B.K. Tanner, M.A.G. Halliwell and M.H. Lyons, Simulation of x-ray double-crystal rocking curves of multiple and inhomogeneous heteroepitaxial layers, *J. Appl. Cryst.* **18**, 446 (1985).

[94] E.E. Fullerton, I.K. Schuller, H. Vanderstraeten and Y. Bruynseraede, Structural refinement of superlattices from x-ray diffraction, *Phys. Rev. B* **45** (16), 9292 (1992).

[95] V. Holy, J. Kubena, I. Ohlidal and K. Ploog, The diffuse x-ray scattering in real periodical superlattices, *Superlattices and Microstructures* **12** (1), 25 (1992).

[96] J.G. Pellegrino, S.B. Qadri, C.M. Cotell, P.M. Amirtharaj, N.V. Nguyen and J. Comas, Interface sharpness during the initial stages of growth of thin, short-period III-V superlattices, *J. Vac. Sci. Technol. A* **11** (4), 917 (1993).

[97] B.D. Cullity, *Elements of X-Ray Diffraction*, Addison-Wesley Publishing Company (1978).

[98] B.E. Warren, *X-Ray Diffraction*, Addison-Wesley Publishing Company (1969).

[99] W.H. Zachariasen, *Theory of X-Ray Diffraction in Crystals*, Dover Inc. (1967).

[100] W.J. Bartels and W. Nijman, X-ray double-crystal diffractometry of $Ga_{1-x}Al_xAs$ epitaxial layers, *J. Cryst. Growth* **44**, 518 (1978).

[101] X.R. Wang, X.Y. Chi, H. Zheng, Z.L. Miao, J. Wang, Z.S. Zhang and Y.S. Jin, X-ray double-crystal diffraction studies of GaInAsP/InP heterostructures, *J. Vac. Sci. Technol. B* **6** (1), 34 (1987).

[102] S.J. Barnett, High resolution x-ray diffraction studies of semiconductor superlattices, *J. Cryst. Growth* **103**, 335 (1990).

[103] E.A. Wood, *Crystal Orientation Manual*, Columbia University Press (1963).

[104] M.S. Goorsky, T.F. Kuech, M.A. Tischler and R.M. Potemski, Determination of epitaxial $Al_xGa_{1-x}As$ composition from x-ray diffraction measurements, *Appl. Phys. Lett.* **59** (18), 2269 (1991).

[105] M. Gailhanou, J.F. Carlin and U. Oesterle, X-ray diffraction analysis of low mismatch epitaxial layers grown on misoriented substrates, *J. Cryst. Growth* **140**, 205 (1994).

[106] P. Auvray, M. Baudet and A. Regreny, X-ray diffraction effects in Ga and Al arsenide structures MBE-grown on slightly misoriented GaAs(001) substrates, *J. Cryst. Growth* **95**, 288 (1989).

[107] B.K. Tanner, S.J. Miles, G.G. Peterson and R.N. Sacks, Measurement of Aluminium concentration in GaAlAs epitaxial layers by double-axis x-ray diffraction, *Materials Letters* **7** (5,6), 239 (1988).

[108] C.R. Wie, Rocking curve peak shift in thin semiconductor layers, *J. Appl. Phys.* **66** (2), 985 (1989).

[109] A.T. Macrander and K.E. Strege, X-ray double-crystal characterization of highly perfect InGaAs/InP grown by vapor-phase epitaxy, *J. Appl. Phys.* **59** (2), 442 (1986).

[110] A.T. Macrander, S. Lau, K. Strege and S.N.G. Chu, Nondestructive measurement of layer thicknesses in double heterostructures by x-ray diffraction, *Appl. Phys. Lett.* **52** (23), 1985 (1988).

[111] X. Chu and B.K. Tanner, Interference peaks in double-crystal x-ray rocking curves of laser structures, *Appl. Phys. Lett.* **49** (26), 1773 (1986).

[112] V.S. Speriosu and T. Vreeland, Jr., X-ray rocking curve analysis of superlattices, *J. Appl. Phys.* **56** (6), 1591 (1984).

[113] C. Ferrari and P. Franzosi, Investigation of the interface grading in III-V heterostructures by double-crystal diffractometry, *J. Appl. Phys.* **65** (4), 1544 (1989).

[114] H.K. Lipsanen and V.M. Airaksinen, Growth and characterization of a GaAs/AlAs superlattice with variable layer thicknesses, *J. Elec. Mater.* **23** (5), 465 (1994).

[115] D.W. Berreman, Dynamical theory of x-ray diffraction in flat, focusing, and distorted crystals by Abelés's matrix method, *Phys. Rev. B* **14** (10), 4313 (1976).

[116] S. Nakatani and T. Takahashi, Dynamical treatment of x-ray reflection from crystal surfaces, *Surf. Sci.* **311**, 433 (1994).

[117] M. Zhen-hong, C. Shu-fan and H. Chu-guang, X-ray analysis of the device structures of III-V compound semiconductors, *Phys. Rev. B* **41** (14), 9930 (1990).

[118] I.K. Schuller, E.E. Fullerton, H. Vanderstraeten and Y. Bruynseraede, Quantitative x-ray structure determination of superlattices and interfaces, *Mat. Res. Soc. Symp. Proc.: Structure/Property Relationships for Metal/Metal Interfaces,* **229**, 41 (1991).

[119] J.M. Vandenberg, R.A. Hamm, M.B. Panish and H. Temkin, High-resolution x-ray diffraction studies of InGaAs(P)/InP superlattices grown by gas-source molecular-beam epitaxy, *J. Appl. Phys.* **62** (4), 1278 (1987).

[120] S.E.G. Slusky and A.T. Macrander, Measurement of the miscut angle of crystal surfaces vicinal to major crystal planes by x-ray diffractometry at glancing incidence, *Appl. Phys. Lett.* **53** (21), 2042 (1988).

[121] M. Gailhanou, Accurate monocrystal miscut angle determination by x-ray diffraction on a wedge, *Appl. Phys. Lett.* **63** (4), 458 (1993).

[122] C. Kittel, *Introduction to Solid State Physics*, John Wiley & Sons, Inc. (1959).

[123] *International Tables for X-Ray Crystallography* **3**, Physical and Chemical Tables, published for the International Union of Crystallogrphy, Kynoch Press (1968).

[124] H. Rhan, U. Pietsch, S. Rugel, H. Metzger and J. Peisl, Investigations of semiconductor superlattices by depth-sensitive x-ray methods, *J. Appl. Phys.* **74** (1), 146 (1993).

[125] M.A.G. Halliwell, Measurement of relaxation in strained layer semiconductor structures, *Advances in X-Ray Analysis* **33**, 61 (1990).

[126] J. Bak-Misiuk, W. Paszkowicz, J. Domagala, S. Miotkowska and Z.R. Zytkiewicz, Determination of $Ga_{1-x}Al_xAs$ epitaxial layer composition by x-ray intensity measurements of quasi-forbidden reflections, *J. Cryst. Growth* **126**, 168 (1993).

[127] P. Ravila, V.M. Airaksinen, H. Lipsanen, T. Tuomi and P.A. Claxton, X-ray diffraction analysis of superlattices grown on misoriented substrates, *J. Cryst. Growth* **114**, 569 (1991).

[128] B. Rosner and H. Berger, Influence of misoriented substrates and dislocations on the diffraction patterns of superlattices, *J. Appl. Cryst.* **26**, 532 (1993).

[129] E.E. Fullerton, W. Cao, G. Thomas, I.K. Schuller, M.J. Carey, and A.E. Berkowitz, Quantitative characterization of epitaxial superlattices by x-ray diffraction and high resolution electron microscopy, *Appl. Phys. Lett.* **63** (4), 482 (1993).

[130] I.K. Schuller and Y. Bruynseraede, Quantitative x-ray diffraction from thin films, *NanoStructured Materials* **1**, 387 (1992).

[131] J.H. Li, Z.H. Mai, S.F. Cui, Z.H. Chen, and M.H. Li, Characterization of $Al_xGa_{1-x}As/Al_yGa_{1-y}As/GaAs$ step multi-quantum wells on (001) GaAs by x-ray double-crystal diffraction, *J. Cryst. Growth* **129**, 532 (1993).

[132] I.O. Clark, *MOCVD requirements for abrupt junction growth*, PhD Dissertation, University of Virginia (1990).

[133] G. Bastard, *Wave Mechanics Applied to Semiconductor Heterostructures,* Halsted Press (1988).

[134] D. ter Haar, *Selected Problems in Quantum Mechanics*, Academic Press Inc. (1964).

[135] H. Kawai, K. Kaneko, and N. Watanabe, Photoluminescence of AlGaAs/GaAs quantum wells grown by metalorganic chemical vapor deposition, *J. Appl. Phys.* **56** (2), 463 (1984).

[136] G. Bastard, E.E. Mendez, L.L. Chang, and L. Esaki, Exciton binding energy in quantum wells, *Phys. Rev. B* **26** (4), 1974 (1982).

[137] M.A. Herman, D. Bimberg and J. Christen, Heterointerfaces in quantum wells and epitaxial growth processes: Evaluation by luminescence techniques, *J. Appl. Phys.* **70** (2), R1 (1991).

[138] S.M. Sze, *Physics of Semiconductor Devices*, John Wiley & Sons (1981).

[139] J.I. Pankove, *Optical Processes in Semiconductors*, Dover Publications (1971).

[140] T.R. Block, D.P. Neikirk, and B.G. Streetman, Photoluminescence study of the effects of growth interruption on integer and fractional monolayer AlGaAs/GaAs quantum wells, *J. Vac. Sci. Technol. B* **10** (2), 832 (1992).

[141] M. Colocci, M. Gurioli, and A. Vinattieri, Thermal ionization of excitons in GaAs/AlGaAs quantum well structures, *J. Appl. Phys.* **68** (6), 2809 (1990).

[142] M.H. Bode and A. Ourmazd, Interfaces in GaAs/AlAs: Perfection and applications, *J. Vac. Sci. Technol. B* **10** (4), 1787 (1992).

[143] T.E. Schlesinger, J.C. Lee, and T.F. Kuech, Interdiffusion of Al and Ga in (Al,Ga)As/GaAs quantum wells, *Mat. Res. Soc. Symp. Proc.: Interfaces, Superlattices, and Thin Films,* **77**, 241 (1987).

[144] M.T. Furtado and M.S.S. Loural, Direct evaluation of interdiffusion coefficients in quantum well heterostructures using photoluminescence, *Superlattices and Microstructures* **14** (1), 21 (1993).

[145] M. Tanaka, H. Sakaki, and J. Yoshino, Atomic-scale structures of top and bottom heterointerfaces in GaAs-$Al_xGa_{1-x}As$ (x=0.2-1) quantum wells prepared by molecular beam epitaxy with growth interruption, *Jap. J. Appl. Phys.* **25** (2), L155 (1986).

[146] M. Tanaka and H. Sakaki, Surface migration study of atoms and formation of truly-smooth top and bottom heterointerfaces in GaAs-AlAs quantum wells by temperature-switched technique in molecular beam epitaxy, *Superlattices and Microstructures* **4** (2), 237 (1988).

[147] H. Sakaki, M. Tanaka and J. Yoshino, One atomic layer heterointerface fluctuations in GaAs-AlAs quantum well structures and their suppression by insertion of smoothing period in molecular beam epitaxy, *Jap. J. Appl. Phys.* **24** (6), L417 (1985).

[148] T. Noda, M. Tanaka and H. Sakaki, Correlation length of interface roughness and its enhancement in molecular beam epitaxy grown GaAs/AlAs quantum wells studied by mobility measurement, *Appl. Phys. Lett.* **57** (16), 1651 (1990).

[149] R.C. Miller, A.C. Gossard, W.T. Tsang, and O. Munteanu, Extrinsic photoluminescence from GaAs quantum wells, *Phys. Rev. B* **25** (6), 3871 (1982).

[150] K. Brunner, G. Abstreiter, G. Böhm, G. Tränkle, and G. Weimann, Sharp-line photoluminescence of excitons localized at GaAs/AlGaAs quantum well inhomogeneities, *Appl. Phys. Lett.* **64** (24), 3320 (1994).

[151] G.B. Stringfellow, The role of impurities in III/V semiconductors grown by organometallic vapor phase epitaxy, *J. Cryst. Growth* **75**, 91 (1986).

[152] D. Kisker, J.N. Miller, and G.B. Stringfellow, Oxygen gettering by graphite baffles during organometallic vapor phase epitaxial AlGaAs growth, *Appl. Phys. Lett.* **40** (7), 614 (1982).

[153] W.D. Johnston, Laser R&D, AT&T Bell Laboratories. Personal communication.

Vita

The author, Karen Oatis, was born in New London, Connecticut, on February 9, 1947. She received a Bachelor of Arts degree in modern languages from Arizona State University in 1969, and a Master of Arts degree in German from San Diego State College in 1971. After a number of years as a hippy and fulltime parent she entered Oregon State University, where she received the Bachelor of Science and Master of Science degrees in Electrical Engineering in 1988 and 1991, respectively. She received an AT&T Bell Laboratories Fellowship for graduate work in 1988. In 1991 she entered Oregon Graduate Institute of Science & Technology to pursue a PhD. She has worked in the area of semiconductor crystal growth, processing, and characterization since she was an undergraduate at Oregon State.